Hydrodynamic and out-of-equilibrium properties of atomic superfluids and quantum fluids of light

Tom Bienaimé

Research Summary

Habilitation à Diriger des Recherches (HDR)

Hydrodynamic and out-of-equilibrium properties of atomic superfluids and quantum fluids of light

Tom Bienaimé

Centre Européen de Sciences Quantiques
et
Institut de Science et d'Ingénierie Supramoléculaires

UMR 7006

Composition du Jury

Donatella Ciampini	*Professeur à l'Université de Pise*	*Rapporteur*
Anna Minguzzi	*Directrice de recherche à Grenoble*	*Rapporteur*
Martin Weitz	*Professeur à l'Université de Bonn*	*Rapporteur*
Jérôme Dubail	*Chargé de recherche HDR à Nancy*	*Examinateur*
Guido Pupillo	*Professeur à l'Université de Strasbourg*	*Examinateur*
Shannon Whitlock	*Professeur à l'Université de Strasbourg*	*Garant et Président du Jury*

Soutenue le 6 décembre 2023

cnrs

Université de Strasbourg

Contents

1. Introduction

The exploration of light-matter interactions has been the focus of many theoretical and experimental efforts over the past centuries to culminate with the development of the field of quantum optics which describes how photons and quantum matter interact. Today, the degree of control of light-matter interactions is so advanced that physical systems of light and atoms can be created, manipulated and observed at the quantum level in research laboratories around the world. Generally, most of the experiments exploit light-matter interactions either to use light (lasers) to control an assembly of atoms or reversely to manipulate and shape light by making it interact with atoms, molecules or nanostructured materials.

On the one side, our understanding of light-matter interactions together with the progressive refinement of experimental techniques over the past 70 years **enable to control atoms (their internal or external degrees of freedom) with unprecedented precision using light fields**. Among many breakthroughs, and only focusing on the field of ultracold atoms, one can underline the crucial role played by the discovery of optical pumping (Nobel prize 1996 of A. Kastler), of laser cooling and trapping (Nobel prize 1997 of S. Chu, C. Cohen-Tannoudji and W. D. Phillips) which subsequently lead to the observation of Bose-Einstein Condensation (Nobel prize 2001 of E. A. Cornell, W. Ketterle and C. E. Wieman) which in turn enabled to use ultracold atoms to build artificial quantum systems that are highly controllable (e.g. tunneling rate of atoms in optical lattices, atomic interactions) and give access to observables that are not available in solid state systems. This is the essence of quantum simulation where it is now possible to create and observe strongly correlated states of matter with single atom resolution using a so-called quantum gas microscope. Today, in the "era of quantum computing discovery", scientists are even building the first generation of universal digital quantum computers using defect-free arrays of single atoms trapped in optical tweezers which play the role of a quantum memory (qubit register). Using all optical techniques, they can manipulate individual qubits, realize quantum logic operations between two qubits and finally measure the final state of the quantum register. This positions the neutral atom platform as a very serious competitor for the race (that is just beginning) to develop large scale quantum computing hardware.

On the other side, **the properties of light can be controlled and tailored using matter which lead to many important applications in quantum optics**. For example, interactions between photons can be engineered when light propagates inside a nonlinear crystal, photons can be stored and retrieved from an atomic ensemble which serves as a quantum memory, spontaneous parametric down-conversion allows for the generation of entangled photon pairs and of single photons, and quantum logic gates have been realized opening interesting perspectives for quantum information applications. Moreover, quantum simulation with photons has been a rapidly growing field over the past decade with the possibility to confine light in multi-mode optical cavities or in arrays of optical resonators together with the ability to control photon-photon interactions by mediating them through the coupling of light to matter. In these systems, the

powerful tools of quantum optics provide new ways to probe, detect and characterize the many-body states of light that are not available for their atomic counterparts.

After writing the above perspective about the research of light-matter interactions, I realize how modest one should be about his own contribution to this very broad and exciting research field. At the same time, I feel proud to have contributed to the two above-described aspects. Indeed, the first part of this habilitation dissertation is devoted to the **atomic aspects**: an ultracold gas of bosonic atoms is controlled by lasers and magnetic fields to explore the generation of quantized vortices when the system is quench through the normal-to-superfluid thermodynamic phase transition or to create and investigate mixtures of two spin states of atomic Bose-Einstein condensates which lead to the observation of spin superfluidity. Conversely, the second part concerns the **photonic aspects**: we investigate how new properties of light emerge when it propagates in a hot atomic vapor cell. In these conditions, photons acquire an effective mass upon propagation in the paraxial approximation while photon-photon interactions can be tuned by adjusting the laser frequency with respect to the atomic transition or by varying the pressure of the atomic vapor. This establishes an interesting new platform for the exploration of quantum fluids of light where we investigated the hydrodymamic behaviors of light or the effect of a quench of the photon-photon interactions as light enters or exits the cell enabling the exploration of the out-of-equilibrium properties of the system. Finally, in the third part, I conclude and briefly present my future research plans where I would like to use ultracold atoms excited to Rydberg states to push the frontier of quantum fluids of light in a regime where the optical nonlinearities are so large that they manifest themselves at the single photon level. Using this system, I aim at developing new methods to create, manipulate and detect the resulting strongly correlated photonic states.

The results presented in this manuscript would not have been possible without collaborating with my colleagues. I am grateful to all the researchers, permanent members, postdocs, PhD and master students with whom I had the chance to work with in stimulating research environments. These very enriching experiences contributed greatly to my success and to the experimental quantum physicist I am today.

Organization of the report: In each section, after putting my contributions in the context of the state of the art of the field and describing the research environment in which these investigations were carried out, I reproduce a selection of my own articles (see section A.2) that highlights and summarizes my scientific contributions. I reformatted the selected articles to match the style of this report and I sometimes removed some technical parts that would distract the reader from getting on overview of my work[1].

[1]The technical parts of the articles that have been discarded are clearly identified. I refer the reader interested in those parts to the original published versions of the articles which are also available on arXiv.

2. Vortices and spin superfluidity in atomic superfluids

2.1. Context

I grew fascinated by the booming field of ultracold gases and quantum simulation after learning about this exciting research line at conferences and schools during my PhD (2008–2011). Subsequently to the first observation of atomic Bose-Einstein condensation (BEC) in 1995 [12, 55, 100], the field has transitioned to explore the properties of bosonic, fermionic and molecular quantum gases and to use these systems to simulate problems of condensed-matter [49]. Among the large quantity of milestone achievements of this research field, I will only mention a few of them to highlight their diversity: the generation of vortices in BECs [259, 263], the observation of the superfluid-to-Mott quantum phase transition [153], the realization of a molecular BEC from a Fermi gas [154, 330, 429], reaching the Tonks–Girardeau regime with a one dimensional ultracold Bose gas in an optical lattice [306], the exploration of the phase diagram and the thermodynamics of a universal Fermi gas [285, 362], the observation of Anderson localization with BECs [43, 333], the in-situ probing of quantum gases with single atom resolution [21, 361], the realization of the topological Haldane model [201] and more recently the observation of supersolids in dipolar quantum gases [53, 81, 381].

Driven by my interest in the superfluid properties of quantum gases and more specifically about quantum vortices, I joined the group of Jean Dalibard in 2013. He and his group have achieved important results that have been very influential to the ultracold atom community and beyond. They pioneered the generation of quantum vortices when a Bose gas is put into rotation [259], studied their dynamics [336], investigated the regime in which the gas is put in fast rotation [60] and characterized several hydrodynamic collective modes [59, 76, 95]. Later, by adding a strong transverse confinement to the quantum gas which enables to freeze one spatial degree of freedom, the interests of the group evolved towards the exploration of 2D Bose gases: they evidenced the Berezinskii-Kosterlitz-Thouless phase transition in ultracold atomic gases [166], explored the thermodynamics of a 2D Bose gas [417] and studied its superfluid behavior [106]. I started to work in the group around that time. About a year before, Jérôme Beugnon and Sylvain Nascimbène had joined Jean Dalibard to work on this research activity. While all the above mentioned studies of the group were carried out in 3D or 2D harmonic traps, we devoted our efforts to trap 2D Bose gases in all-optical uniform potentials which consists of a strong transverse harmonic confinement to freeze the gas in the vertical direction combined with a "box-like" in-plane confinement. Our goal was to overcome a limitation of harmonic traps, where the nonuniform density leads to spatially varying energy and length scales which hinders the exploration of critical phenomena for which the correlation length diverges. We upgraded the existing setup by replacing the in-plane harmonic confinement by a blue detuned box potential that was realized by imaging a dark intensity mask obtained by a metallic deposit on a glass plate while keeping the original transverse confinement consisting of a blue-detuned optical potential that was shaped into a Hermite-Gauss mode. Finalizing this upgrade, we were loading the 2D box potential by applying evaporative ramps when we noticed that sometimes

the absorption images after a short free space expansion featured small density holes that varied in number and position for each experimental cycle that ran with the exact same experimental parameters. We soon realized that they were stochastically generated quantum vortices which were created when the Bose gas was quenched across the normal-to-superfluid transition and we related the rate of nucleation of these topological defects to the Kibble-Zurek mechanism [15, 210, 427]. This work was published in [P8] together with an extensive study of the transverse condensation transition that occur when the normal-to-superfluid transition is crossed. The ability to design dark intensity masks with arbitrary shape in the clean room enabled to explore the same physics in an annular geometry which corresponds to the configuration originally proposed by Zurek [427]. This was realized by measuring the supercurrent that was stochastically created in the ring-shape trap during the quench with an original interferometric technique [P9]. In addition to these experiments, I supervised the construction of the next generation of experimental setup to explore 2D Bose gase in uniform potentials [P19]. The main innovations of the new design were i) a new 2D confinement method which was realized by a blue-detuned optical accordion lattice for which the spacing of the interference fringes can be dynamically tuned to load the quantum gas with a large lattice spacing in a single dark plane and then compress it to strong 2D confinement by dynamically reducing the lattice spacing ii) a new high-resolution imaging and in-plane trapping potential using two microscope objectives located below and above the plane of the 2D gas. The in-plane potential profile was obtained by direct imaging of the chip of a spatial light modulator which enables the creation of uniform potentials with arbitray geometry. After completing the construction of the new setup, we performed a first experiment in which we studied the cooperative effects when light scatters a dense atomic layer [P17] in strong connection with the problems I investigated during my PhD[2]. Moreover, over the years, the new setup has proven to be very reliable as it later led to many important results and is still currently being used at Collège de France ten years after its construction.

I first encountered Gabriele Ferrari in 2015 when he came to the PhD defense of Lauriane Chomaz, a PhD student in the group of Jean Dalibard. After moving to Trento to start his own group together with Giacomo Lamporesi, they builded a new setup of sodium BECs. Similarly to what happened at LKB, they fortuitously observed the first solitonic vortices in their setup while optimising the evaporation ramps to get a large BEC and connected the rate of their spontaneous creation to the Kibble-Zurek mechanism [240]. Note that contrary to what happens in uniform traps, the non-uniform atomic density in a 3D harmonic potential complicated the analysis because the critical point of the phase transition is crossed locally at different time of the evaporation ramp. They investigated in great details the properties [109] and the dynamics [359] of the topological defects that were created during the quench. The properties of these topological defects interpolate between the characteristics of solitons and vortices due to the large anisotropy of the trapping potential. I joined the group of Trento in October 2015 driven by my interest to continue working on topological defects in atomic BECs while I was also given the opportunity to broaden the range of my research expertise

[2]During my PhD I studied cooperative effects in large and dilute clouds of cold atoms

by leading a new research direction on spinor BECs. In [P20], we extended the results of [240], by making more systematic and extansive measurements of the number of defects that were spontaneously created in the BEC after quench cooling the gas at different rate and for several transverse confinement. We then moved to the exploration of the dynamics and the interactions of topological defects using an innovative minimaly intrusive imaging method that enables to follow the real-time position and orientation of vortex lines by repeatedly extracting a small fraction of the atoms from the gas. We applied this technique to visualize the spinning dynamics of a single solitonic vortex line in an elongated cigar-shaped trap [P18] and to investigate quantum vortex interactions in an atomic Bose-Einstein condensate [P6]. In these experiments, the initial conditions of the system, *i.e.* the number of vortices, their positions and orientations was stochastically generated which forced us to record a large number of experimental runs to acquire a lot of data about the dynamics and interactions of vortices for different initial conditions. Aside from the experimental investigations on topological defects, I was in charge of developping a new research activity on mixtures of BECs[3]. Starting from a spin-polarized sodium BEC in a dipole trap, we created an ultracold mixture of the $|F = 1, m_F = -1\rangle$ and $|F = 1, m_F = +1\rangle$ spin states of sodium atoms using sequencially a Landau–Zener transition and a controlled Rabi oscillation. We showed that the specific properties of this spin mixture – that is not subjected to buoyancy and is missible while still being very close to the missible-immiscible phase transition – leads to a huge enhancement of the spin-dipole polarizability and to the consequent softening of the frequency of the spin-dipole oscillation [P7]. In addition to this study which was done for a mixture of fully condensed spin states (zero temperature), we explored the effects of finite temperature which lead to the observation of spin superfluididy [P5]. Note that these first results on spin mixtures from the group of Trento were seminal to many of their later studies [89, 124, 125, 421].

In order to give a good perspective about my contributions to the field of atomic quantum gases I picked i) three articles on the topic of *the creation and the dynamics of topological defects on atomic BECs*: two from my work in Paris on quenched induced topological defects in 2D uniform [P8] and annular geometries [P9] and one from my work in Trento about the dynamics and interaction of vortices [P6] ii) two articles about *binary mixtures of atomic BECs* from my work in Trento [P7] [P5].

2.2. Creation and dynamics of topological defects in atomic Bose gases

2.2.1. Quench-induced supercurrents in an annular Bose gas [P9]

Abstract: We create supercurrents in annular two-dimensional Bose gases through a temperature quench of the normal-to-superfluid phase transition. We detect the magnitude and the direction of these supercurrents by measuring spiral patterns resulting from the interference of the cloud with a central reference disk. These measurements demonstrate the stochastic nature of the supercurrents. We further measure their

[3]This research line was new for the group of Trento.

distribution for different quench times and compare it with predictions based on the Kibble-Zurek mechanism.

Fluids in annular geometry are ideally suited to investigate the role of topological numbers in quantum mechanics. The phase winding of the macroscopic wavefunction around the annulus must be a multiple of 2π, ensuring the quantization of the circulation of the fluid velocity. The resulting supercurrents have been observed in superfluid systems such as superconductors [364], liquid helium [35] and atomic gases [280, 343]. Studying these currents is crucial for the understanding of quantum fluids, as well as for realizing sensitive detectors like magnetometers [356] and rotation sensors [304].

Supercurrents in annular atomic Bose-Einstein condensates (BECs) are usually created in a deterministic way by using laser beams to impart angular momentum on the atoms [33, 280, 343] or by rotating a weak link along the annulus [414]. Supercurrents can also have a stochastic origin. They may result from thermal fluctuations or appear as topological defects following a rapid quench of the system. The latter mechanism was put forward by Kibble and Zurek (KZ), who studied the phase patterns that emerge in a fluid, when it undergoes a fast crossing of a phase transition point [210, 427].

The KZ mechanism has been studied in several types of systems such as liquid crystals [82], helium [32, 342], ion chains [325, 390], superconducting loops [276] and BECs [58, 240, 406]. For a superfluid confined in a ring geometry, which is the configuration originally considered by Zurek [427], the frozen phase of the wavefunction may lead to a supercurrent of charge q, i.e. a $2\pi q$ phase winding along the ring. In this section, we study a setup realizing this *gedanken* experiment using a quasi two-dimensional (2D) Bose gas trapped in an annular geometry. For each realization of the experiment, we use matter-wave interference between this annulus and a central disk acting as a phase reference, to measure the charge as well as the direction of the random supercurrent [4].

Our experiments are performed with a Bose gas of ^{87}Rb atoms. Along the vertical (z) direction the gas is confined using a harmonic potential with frequency $\omega_z/2\pi = 370\,\mathrm{Hz}$ (figure 1a) [5]. In the horizontal (xy) plane, the atoms are trapped in the dark regions of a "box-potential" beam, engineered using an intensity mask located in a plane optically conjugated to the atom cloud [6]. We use a target-like mask, consisting of a disk of radius $R_0 = 4.5\,\mu\mathrm{m}$ surrounded by a ring of inner (resp. outer) radius of $R_{\mathrm{in}} = 9\,\mu\mathrm{m}$ (resp. $R_{\mathrm{out}} = 15\,\mu\mathrm{m}$) (figure 1b).

The typical time sequence for preparing the gas starts by loading a gas with a 3D phase-space density ≈ 2.4 slightly below the condensation threshold [7] with the box-potential beam at its maximal power. Then we lower linearly this power by a factor ~ 50 in a time t_{evap} to evaporatively cool the atomic cloud and cross the superfluid transition [106]. Last we keep the atoms at a constant box potential depth during a time t_{hold}.

[4] A similar method has recently been developed to investigate the supercurrent generated by a rotating weak link [112]

[5] For details, see Supplemental Material.

[6] see [142] for a 3D version of a similar setup

[7] The estimated total atom number 76000 and the temperature is 210 nK. With these parameters, we never observe any interference fringes such as those of fig 2.

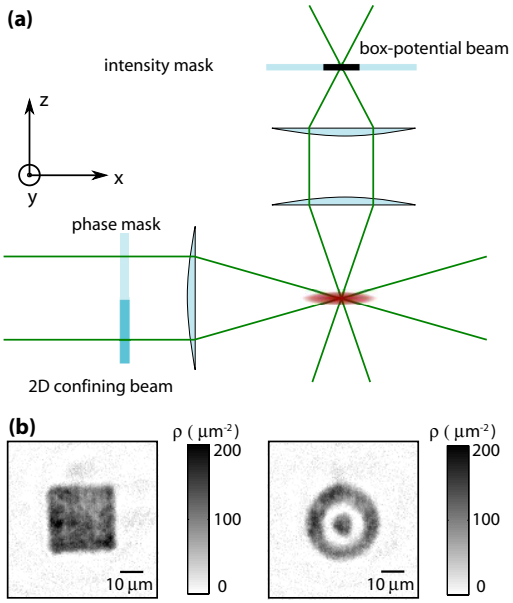

Figure 1. ***Production of box-like potentials using an intensity mask.*** *(a) Along the vertical direction, atoms are confined by a laser beam with an intensity node in the plane $z = 0$ which is shaped using a phase plate (π phase shift between the upper and lower halves of the phase plate). In plane, atoms are trapped in box-like potentials created by imaging an intensity mask onto the atomic plane. The box-like potentials are created by imaging an intensity mask onto the atomic plane. (b) In-situ images of uniform gases in the square and target potentials. Figure from [P9].*

The final temperature is $\sim 10\,\mathrm{nK}$ with similar surface densities in the ring and the disk: $\rho \sim 80\,\mu\mathrm{m}^{-2}$. The typical interaction energy per atom is $E_{\mathrm{int}}/k_{\mathrm{B}} \approx 8\,\mathrm{nK}$, and the gas is marginally quasi-2D with $k_{\mathrm{B}}T$, $E_{\mathrm{int}} \sim \hbar\omega_z$. These parameters correspond to a large 2D phase-space density, $\mathcal{D} = \rho\lambda^2 \geq 100$, so that the gas is deeply in the superfluid regime at the end of the evaporation ramp ($\lambda = \left[2\pi\hbar^2/(mk_{\mathrm{B}}T)\right]^{1/2}$ is the thermal wavelength and m the mass of the ^{87}Rb atom).

We use matter-wave interference to probe the relative phase distribution between the cloud in the central disk and the one in the ring. We abruptly switch off the box-potential while keeping the confinement along the z direction. The clouds experience a hydrodynamical expansion during which the initial interaction energy is converted into kinetic energy. After 7 ms of expansion, we record the interference pattern by imaging the atomic gas along the vertical direction. Typical interference patterns are shown in figure 2. Most of them consist in concentric rings, as expected for a quasi-uniform phase distribution in the disk and the annulus. However we also observe a significant fraction of spiral patterns, revealing the presence of a phase winding in the wavefunction of one of the two clouds.

We developed an automatized procedure to analyze these patterns, which reconstructs

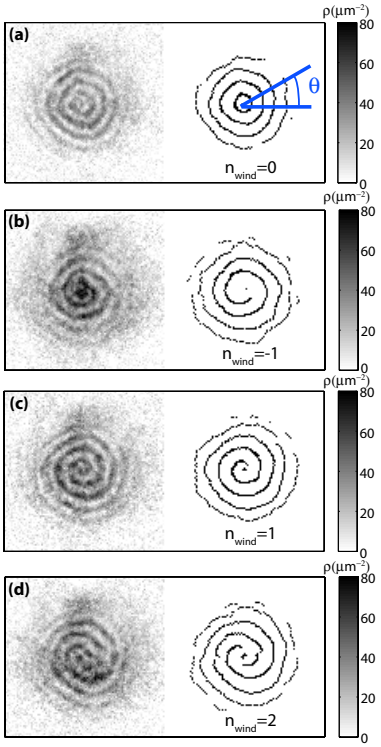

Figure 2. ***Experimental interference patterns.*** *Examples of interference patterns after expansion in the 2D plane, along with constrast-amplified pictures. (a) without phase winding, (b) with phase winding -2π, (c) with phase winding $+2\pi$, (d) with phase winding $+4\pi$. Figure from [P9].*

the phase $\phi(\theta)$ of the fringes along a line of azimuthal angle θ. From the accumulated phase $\Delta\phi$ as the angle θ varies from 0 to 2π, we associate to each pattern a winding number $n_{\rm wind} = \Delta\phi/2\pi$, which is a positive, null or negative integer. This number is recorded for many realizations of the same experimental sequence. Examples of the probability distribution of $n_{\rm wind}$ are shown on figure 3a and b. The measured histograms are compatible with a zero mean value [8]. For example, if we use all the data presented on figure 3c and 3d we find $\langle n_{\rm wind}\rangle = 0.002\,(20)$. This confirms the stochastic nature of the mechanism at the origin of this phase winding.

The first question that arises is the origin of the observed phase winding, which can be due either to a vortex in the central disk or to a quantized persistent current in the outer ring. We can experimentally eliminate the first possibility by noticing that when doing a 3D ballistic expansion (by switching-off both the box-potential beam and the confining beam in the z direction) we never observe any vortex signature in the small disk

[8] The observed asymetry on figure 3b (mean value is 1.4 times the standard deviation) is compatible with the number of realizations: the probability to have a standard deviation equal or larger than this one is 17%.

of radius $R_0 = 4.5\,\mu$m. By contrast, in larger structures such as the square represented in Fig. 1b , we can detect deep density holes revealing the presence of vortices [P8]. Hence we conclude that the spiral interference patterns of figure 2 reveal the presence of a supercurrent in the annulus, whose charge and orientation correspond to the modulus and sign of the winding number n_{wind}. The lifetime of this supercurrent is similar to the cloud lifetime (see Fig. 3c).

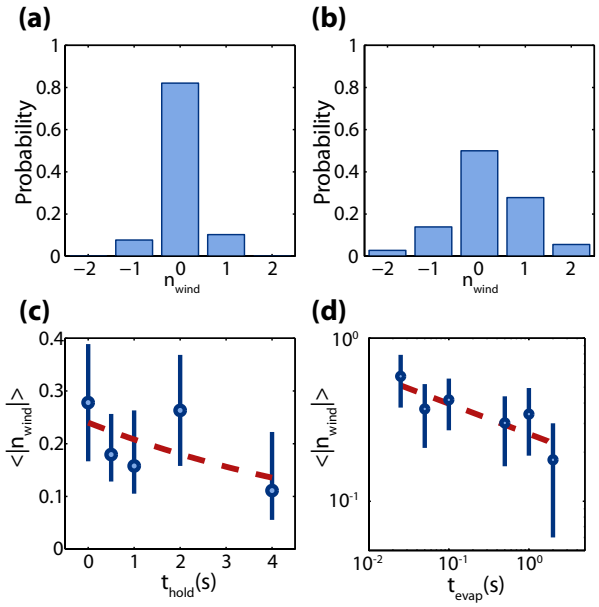

Figure 3. ***Study of the winding number.*** *(a) and (b) Histograms showing the statistical appearance of winding number n_{wind} for $t_{\mathrm{hold}} = 0.5\,s$. (a) We show the result of 39 realizations for $t_{\mathrm{evap}} = 2\,s$. We get $\langle n_{\mathrm{wind}}\rangle = 0.03\,(8)$. (b) We show the result of 36 realizations for $t_{\mathrm{evap}} = 0.025\,s$. We get $\langle n_{\mathrm{wind}}\rangle = 0.19\,(14)$. (c) Mean absolute winding number $\langle|n_{\mathrm{wind}}|\rangle$ as a function of hold time ($t_{\mathrm{evap}} = 2\,s$). The data is fitted with an exponential with a time constant of 7 s. (d) Mean absolute winding number $\langle|n_{\mathrm{wind}}|\rangle$ as a function of evaporation time ($t_{\mathrm{hold}} = 0.5\,s$) in log-log scale. The line is a power-law fit to the data, $\langle|n_{\mathrm{wind}}|\rangle \propto t_{\mathrm{evap}}^{-\alpha}$, gives $\alpha = 0.19\,(6)$. The uncertainty on $\langle n_{\mathrm{wind}}\rangle$ and the bars on figure 3c-d represent the statistical error determined with a bootstrapping approach described in Supplemental Material. Figure from [P9].*

We now discuss the origin of the observed supercurrents, which can be either thermal excitations or result from the quench cooling. If these currents had a thermal origin, their probability of occurrence would be given by the Boltzmann law $p(n_{\mathrm{wind}}) \propto \exp\left[-E(n_{\mathrm{wind}})\,/\,k_{\mathrm{B}}T\right]$, where the (kinetic) energy of the supercurrent is

$$E(n_{\mathrm{wind}}) = n_{\mathrm{wind}}^2\,\frac{\pi\hbar^2\rho}{m}\,\ln\left(R_{\mathrm{out}}/R_{\mathrm{in}}\right). \tag{1}$$

This leads to

$$p(n_{\mathrm{wind}}) \propto \left(R_{\mathrm{in}}/R_{\mathrm{out}}\right)^{n_{\mathrm{wind}}^2\mathcal{D}/2}, \tag{2}$$

which is negligible for $n_{\text{wind}} \neq 0$ for our large phase space densities $\mathcal{D} \geq 100$, in clear disagreement with the typical 20-50% of pictures showing phase winding. Note that the probability for a vortex to appear in the central disk as a thermal excitation is even smaller than (2) because R_{in} and R_{out} should be replaced respectively by the healing length ($\lesssim 0.5\,\mu$m) and R_0.

To check that the quench cooling is indeed responsible for the formation of these supercurrents, we study the variation of $\langle|n_{\text{wind}}|\rangle$ for evaporation times spanning two orders of magnitude. The comparison between the results for a slow quench (figure 3a) and a fast quench (3b) show that the latter indeed increases the probability of occurrence of a supercurrent, as expected for the KZ mechanism [210, 427]. We summarize in figure 3d the experimental variation of $\langle|n_{\text{wind}}|\rangle$ with t_{evap}, and find that it increases from 0.2 ($t_{\text{evap}} = 2\,$s) to 0.6 ($t_{\text{evap}} = 0.025\,$s). A power-law fit to the data, inspired by the prediction for the KZ mechanism, leads to $\langle|n_{\text{wind}}|\rangle \propto t_{\text{evap}}^{-\alpha}$ with $\alpha = 0.19\,(6)$.

To interpret our results we have developed a simple one-dimensional (1D) model following the KZ scenario presented in [98, 427]. We consider a 1D ring of perimeter L and we assume that, when the normal-to-superfluid transition is crossed, N domains of uniform phase ϕ_j, $j = 1, \ldots, N$ are created. Each run of the experiment is modeled by a set $\{\phi_j\}$, where the phases ϕ_j are independent random variables drawn in $(-\pi, \pi]$ (with $\phi_1 = 0$ by convention). For each set of $\{\phi_j\}$ we calculate the total phase variation along the ring $\Phi = \sum_j \phi_j$ and define n_{wind} as the nearest integer to $\Phi/2\pi$. We then average over many draws of the set $\{\phi_j\}$. Our experimental range $0.2 \leq \langle|n_{\text{wind}}|\rangle \leq 0.6$ is obtained for $3 \leq N \leq 10$, corresponding to the approximate power-law scaling (see Supp. Mat.)

$$\langle|n_{\text{wind}}|\rangle \propto N^{0.8}. \tag{3}$$

Then we use the general prediction for the KZ mechanism to relate the typical length $\hat{\xi} = L/N$ of a domain to the quench time t_{evap} (see e.g. [98])

$$\hat{\xi} \propto t_{\text{evap}}^{\nu/(1+\nu z)}, \tag{4}$$

where ν and z define the universality class of the transition: ν is the correlation length critical exponent and z the dynamic critical exponent. Using $z = 2$ and $\nu = 1/2$ relevant for a mean-field description of a 1D ring-shaped system [98], we get

$$\hat{\xi} = \frac{L}{N} \propto t_{\text{evap}}^{1/4}. \tag{5}$$

Combining (3) and (5), we predict with this simple model

$$\langle|n_{\text{wind}}|\rangle \propto t_{\text{evap}}^{-1/4\times 0.8} \approx t_{\text{evap}}^{-0.2}, \tag{6}$$

which is in agreement with the experimental result $\alpha = 0.19\,(6)$.

There are two main assumptions that could limit the validity of this model. First, our system is not uni-dimensional in terms of relevant single particle eigenstates. However,

we find for our parameters that $\hat{\xi}$ is in the range 7–25 μm [9][10]; this is always larger than the width of our annulus and justifies the use of a 1D model for describing the phase coherence properties of the gas. Second, this model does not take into account beyond mean-field effects, related to either the finite size of the system or the crossover between standard BEC and the Berezinskii–Kosterlitz–Thouless mechanism. This could change the value of the critical exponents and even lead to deviations with respect to the power-law scaling of (4) [194].

We now discuss the possible extension of this work to a more thorough test of the KZ mechanism. Power-law scaling is challenging to test in our situation because of the low value of the exponent (≈ 0.2) even if we span two orders of magnitude for t_{evap}. The extreme values of this range are experimentally limited: (i) The evaporation time t_{evap} should be chosen long enough so that at any given time a local thermal equilibrium is achieved in the cloud. (ii) The largest evaporation time is set by the cloud lifetime. These two limits cannot be significantly modified, which fixes the relative range of variation of the number of domains N. It could also be interesting to study situations with absolute larger $N = L/\hat{\xi}$. For a given density the local equilibrium requirement limits the lower value of $\hat{\xi}$ and one can only increase the length of the ring L. Within current experimental techniques, it should be possible to load one order of magnitude more atoms, leading for a given transverse size to an increase of N by the same factor.

Here, we skip a section about extracting information from the interference patterns which goes beyond the determination of the topological number.

In summary, we have created supercurrents in annular Bose gases by a temperature quench. The measured distribution of direction and magnitude of these supercurrents are compatible with the KZ mechanism's predictions. This work could be extended to more refined tests of the KZ mechanism by testing the power-law scaling with the size of the annulus and correlate the number of topological defects with the condensed fraction of the system [98].

2.2.2. Emergence of coherence via transverse condensation in a uniform quasi-2D Bose gas [P8]

Abstract: Phase transitions are ubiquitous in our three-dimensional world. By contrast most conventional transitions do not occur in infinite uniform two-dimensional systems because of the increased role of thermal fluctuations. Here we explore the dimensional crossover of Bose–Einstein condensation (BEC) for a weakly interacting atomic gas confined in a novel quasi-two-dimensional geometry, with a flat in-plane trap bottom. We detect the onset of an extended phase coherence, using velocity distribution measurements and matter-wave interferometry. We relate this coherence to the transverse condensation

[9] An estimate of $\hat{\xi}$ for our geometry is $\pi\,(R_{\mathrm{in}} + R_{\mathrm{out}})/N$

[10] We note that $\hat{\xi}$ is then larger than the size R_0 of the central disk. This confirms the fact that we do not expect the presence of vortices in this disk

phenomenon, in which a significant fraction of atoms accumulate in the ground state of the motion perpendicular to the atom plane. We also investigate the dynamical aspects of the transition through the detection of topological defects that are nucleated in a quench cooling of the gas, and we compare our results to the predictions of the Kibble–Zurek theory for the conventional BEC second-order phase transition.

Bose–Einstein condensation (BEC) is a remarkably simple phase transition that can in principle occur in a fluid even in the absence of interatomic interactions. As a mere result of single-particle statistics, a phase-coherent fraction appears in the fluid, described by a uniform wave-function spanning the whole system. During the last two decades, cold atom experiments have been used to probe many aspects of BEC [249, 312, 317]. However, most of these cold atom studies are performed in the presence of a harmonic confinement. BEC becomes in this case a local transition: the condensate forms at the center of the trap where the density is the largest, and interactions between particles play a dominant role in the equilibrium state of the fluid. In this geometry the non-homogeneous character of the gas makes it difficult to address some important features of BEC, such as the existence of long-range phase coherence. The recent achievement of a three-dimensional (3D) Bose gas undergoing BEC in a box-like potential [142, 151] constitutes an important step forward, realizing the text-book paradigm of an extended and uniform coherent matter wave.

When turning to low-dimensional (low-D) systems, subtle effects emerge due to the entangled roles of Bose statistics and thermal fluctuations. First, in an infinite low-D ideal gas, no BEC is expected at non-zero temperature, because of the modification of the single-particle density of states with respect to the 3D case [183]. In other words, the phase coherence between two points tends to zero when their distance increases, contrary to the 3D situation. Second, Bose statistics may facilitate the freezing of some directions of space required to produce a low-D system. Consider the uniform two-dimensional (2D) case obtained by imposing a tight harmonic trapping potential (frequency ν_z) along the third direction z. The transverse condensation phenomenon [18, 341, 393] allows one to reach an effective 2D situation even in the "thermally unfrozen" regime, where the quantum $h\nu_z$ is smaller than the thermal energy k_BT (h and k_B stand for Planck's and Boltzmann's constants). Third, for the 2D case in the presence of interactions between the particles, the situation gets more involved with the possibility of a superfluid, Berezinskii–Kosterlitz–Thouless (BKT) transition [37, 229] for a large enough phase-space-density, even though the absence of true long-range coherence remains valid [176, 266]. This superfluid transition has been identified and characterized over the recent years with non-homogeneous, harmonically trapped Bose gases [79, 84, 106, 164, 166, 185, 388].

Another key feature of phase transitions for uniform systems is the time needed to establish the coherence/quasi-coherence over the whole sample. As is well known for critical phenomena [177], the coherence length and the thermalization time diverge at the transition point, thus limiting the size of the phase-coherent domains that are formed at its crossing. The Kibble–Zurek (KZ) theory [210, 427] allows one to evaluate the scaling of the domain size with the speed of the crossing. Once the transition has occurred, these

domains start merging together. During this coarsening dynamics singularities taking the form of topological defects can be nucleated at their boundaries, with a spatial density directly related to the characteristic domain size. The KZ mechanism has been studied in a variety of experimental systems (see for example [32, 82, 276, 325, 342, 390]), including cold atomic gases [58, 74, 240, 344, 406] [P9]. In 2D quantum fluids, the singularities take the form of quantized vortices, *i.e.*, points of zero density around which the macroscopic wavefunction of the gas has a $\pm 2\pi$ phase winding.

In this section, we present an experimental realization of a uniform atomic Bose gas in a quasi-2D geometry, addressing both the steady state of the fluid and its quench dynamics. First with the gas in thermal equilibrium, we characterize the threshold for the emergence of an extended phase coherence by two independent methods, based on (i) the measurement of the atomic velocity distribution and (ii) matter-wave interferences. We show in particular that for the thermally unfrozen case $\zeta \gg 1$ (with $\zeta = k_B T/h\nu_z$), the transverse condensation phenomenon induces an extended in-plane coherence. Second, we explore the quench dynamics of the gas prepared in an initial state such that $\zeta \gg 1$ and observe density holes associated to vortices. We study the relation between the cooling rate and the number of vortices that subsist after a given relaxation time, and we compare our results with the predictions of the Kibble–Zurek theory.

Results

Production of uniform gases in quasi-2D geometries. We prepare a cold 3D gas of rubidium (^{87}Rb) atoms using standard laser and evaporative cooling techniques. Then we transfer the gas in a trap formed with two orthogonal laser beams at wavelength 532 nm, shorter than the atomic resonance wavelength (780 nm), so that the atoms are attracted towards the regions of low light intensity (Fig. 4 a). The strong confinement along the z direction (vertical) is provided by a laser beam propagating along the x direction. It is prepared in a Hermite–Gauss mode, with a node in the plane $z = 0$, and provides a harmonic confinement along the z direction with a frequency ν_z in the range $350 - 1500$ Hz. For the confinement in the horizontal xy plane, we realize a box-like potential by placing an intensity mask on the second laser beam path, propagating along the z direction (Fig. 4 b). Depending on the study to be performed, we can vary the shape (disk, square, double rectangle) and the area $\mathcal{A}$ (from 200 to 900 μm^2) of the region accessible to the gas in the plane. The relevance of our system for the study of 2D physics is ensured by the fact that the size of the ground state along the z direction $a_z = \sqrt{h/(m\nu_z)}/2\pi \sim 0.3$ – $0.6\,\mu$m is very small compared to the in-plane extension $\sqrt{\mathcal{A}} \sim 15$ – $30\,\mu$m. The number of atoms N that can be stored and reliably detected in this trap ranges between 1000 and 100 000. We adjust the temperature of the gas in the interval $T \sim 10 - 250$ nK by varying the intensity of the beam creating the box potential, taking advantage of evaporative cooling on the edges of this box. The ranges spanned by ν_z and T allow us to explore the dimensional crossover between the thermally frozen regime ($\zeta \ll 1$) and the unfrozen one ($\zeta \gg 1$). Examples of in situ images of 2D gases are shown in Fig. 4 c,d,e.

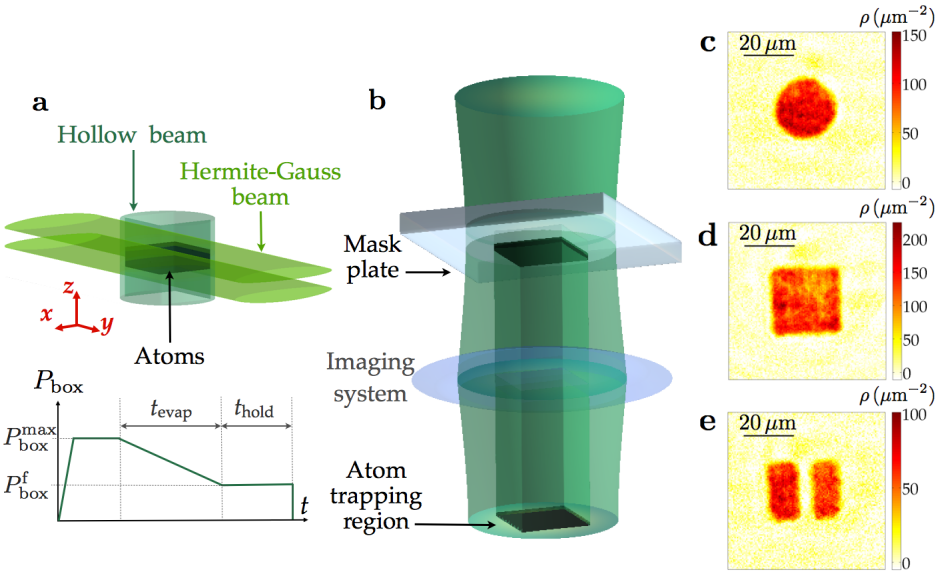

Figure 4. ***Production of uniform Bose gases in quasi-2D geometries.*** *(a) We slice a horizontal sheet from a 3D cold gas of rubidium atoms using a blue detuned laser beam propagating along x and shaped with an intensity node in the $z = 0$ plane. It creates an adjustable harmonic confinement along z of frequency $\nu_z = 350$–$1500\,Hz$. We superimpose a hollow beam propagating along z and producing a uniform confinement in the xy plane (see b). The power P_{box} of this beam is ramped up in $10\,ms$ to its maximal value P_{box}^{max} corresponding to a potential barrier $U_{box} \sim k_B \times 3\,\mu K$ for the rubidium atoms. After holding P_{box} at P_{box}^{max} for $0.5\,s$, we lower it linearly to its final value P_{box}^{f} in a typical time of $t_{evap} = 2\,s$ and keep it constant for a typical $t_{hold} = 0.5\,s$. We vary P_{box}^{f} to adjust the final temperature of the gas via evaporative cooling. (b) The in-plane (xy) confinement is provided by a blue-detuned laser beam shaped by placing a dark intensity mask on its path and imaging it at the position of the atoms. (c, d, e): In-situ density distributions of uniform gases trapped in a disk of radius $R = 12\,\mu m$, a square box of length $L = 30\,\mu m$, and two coplanar and parallel rectangular boxes of size $24 \times 12\,\mu m^2$, spaced by $d = 4.5\,\mu m$. These distributions are imaged using a high intensity absorption imaging technique. Figure from [P8].*

Phase coherence in 2D geometries. For an ideal gas an important consequence of Bose–Einstein statistics is to increase the range of phase coherence with respect to the prediction of Boltzmann statistics. Here coherence is characterized by the one-body correlation function $G_1(\mathbf{r}) = \langle\hat{\psi}^\dagger(\mathbf{r})\,\hat{\psi}(\mathbf{0})\rangle$, where $\hat{\psi}(\mathbf{r})$ [resp. $\hat{\psi}^\dagger(\mathbf{r})$] annihilates (resp. creates) a particle in $\mathbf{r}$, and where the average is taken over the equilibrium state at temperature T. For a gas of particles of mass m described by Boltzmann statistics, $G_1(r)$ is a Gaussian function $\propto \exp(-\pi r^2/\lambda_T^2)$, where $\lambda_T = h/(2\pi m k_B T)^{1/2}$ is the thermal wavelength.

Consider the particular case of a 2D Bose gas (*e.g.*, $\zeta \ll 1$). When its phase-space-density $\mathcal{D} \equiv \rho\lambda_T^2$ becomes significantly larger than 1 (ρ stands for the 2D spatial density), the structure of $G_1(r)$ changes. In addition to the Gaussian function mentioned above, a broader feature $\propto \exp(-r/\ell)$ develops, with the characteristic length ℓ that increases exponentially with $\mathcal{D}$ (see [165])

$$\ell = \frac{\lambda_T}{\sqrt{4\pi}}\,\exp(\mathcal{D}/2). \tag{7}$$

Usually two main effects amend this simple picture:

- In a finite system, when the predicted value of ℓ becomes comparable to the size L of the gas, one recovers a standard Bose–Einstein condensate, with a macroscopic occupation of the ground state of the box potential [313]. The G_1 function then takes non-zero values for any $r \leq L$ and the phase coherence extends over the whole area of the gas.

- In the presence of weak repulsive interactions, the increase of the range of G_1 for $\mathcal{D} \gtrsim 1$ is accompanied with a reduction of density fluctuations, with the formation of a "quasi-condensate" or "pre-superfluid" state [84, 322, 388]. This state is a medium that can support vortices, which will eventually pair at the superfluid BKT transition for a larger phase-space-density, around $\mathcal{D} \sim 8 - 10$ for the present strength of interactions [322]. At the transition point, the coherence length ℓ diverges and above this point, $G_1(r)$ decays algebraically.

Role of the third dimension for in-plane phase coherence. When the thermal energy $k_B T$ is not negligibly small compared to the energy quantum $h\nu_z$ for the tightly confined dimension, the dynamics associated to this direction brings interesting novel features to the in-plane coherence. First, we note that the function $G_1(r)$ can be written in this case as a sum of contributions of the various states j_z of the z motion. The term with the longest range corresponds to the ground state $j_z = 0$, with an expression similar to (7) where $\mathcal{D}$ is replaced by the phase-space-density $\mathcal{D}_0$ associated to this state. Now, consider more specifically the unfrozen regime $\zeta \gg 1$. In this case one expects that for very dilute gases only a small fraction f_0 of the atoms occupies the $j_z = 0$ state; Boltzmann statistics indeed leads to $f_0 = 1 - e^{-1/\zeta} \approx 1/\zeta \ll 1$. However for large total phase-space densities $\mathcal{D}_{\mathrm{tot}}$, Bose–Einstein statistics modifies this result through the

transverse condensation phenomenon ($\mathrm{BEC}_\perp$) [393]: The phase-space-density that can be stored in the excited states $j_z \neq 0$ is bounded from above, and $\mathcal{D}_0$ can thus become comparable to $\mathcal{D}_{\mathrm{tot}}$. This large value of $\mathcal{D}_0$ leads to a fast increase of the corresponding range of $G_1(r)$, thus linking the transverse condensation to an extended coherence in the xy plane. This effect plays a central role in our experimental investigation.

Phase coherence revealed by velocity distribution measurements. To characterize the coherence of the gas, we study the velocity distribution, *i.e.*, the Fourier transform of the $G_1(r)$ function. We approach this velocity distribution in the xy plane by performing a 3D time-of-flight (3D ToF): We suddenly switch off the trapping potentials along the three directions of space, let the gas expand for a duration τ, and finally image the gas along the z axis. In such a 3D ToF, the gas first expands very fast along the initially strongly confined direction z. Thanks to this fast density drop, the interparticle interactions play nearly no role during the ToF and the slower evolution in the xy plane is governed essentially by the initial velocity distribution of the atoms. The time-of-flight (ToF) duration τ is chosen so that the size expected for a Boltzmann distribution $\tau\sqrt{k_B T/m}$ is at least twice the initial extent of the cloud. Typical examples of ToF images are given in Fig. 5 a-f. Whereas for the hottest and less dense configurations, the spatial distribution after ToF has a quasi-pure Gaussian shape, a clear non-Gaussian structure appears for larger N or smaller T. A sharp peak emerges at the center of the cloud of the ToF picture, signaling an increased occupation of the low-momentum states with respect to Boltzmann statistics, or equivalently a coherence length significantly larger than λ_T.

In order to analyze this velocity distribution, we chose as a fit function the sum of two Gaussians of independent sizes and amplitudes, containing N_1 and N_2 atoms, respectively (see Fig. 5 d-f). We consider the *bimodality parameter* $\Delta = N_1/N$ defined as the ratio of the number of atoms N_1 in the sharpest Gaussian to the total atom number $N = N_1 + N_2$. A typical example for the variations of Δ with N at a given temperature is shown in Fig. 5 g for an initial gas with a square shape (side length $L = 24\,\mu$m). It shows a a sharp crossover, with essentially no bimodality ($\Delta \ll 1$) below a critical atom number $N_{\mathrm{c}}(T)$ and a fast increase of Δ for $N > N_{\mathrm{c}}(T)$. We extract the value $N_{\mathrm{c}}(T)$ by fitting the function $\Delta \propto (1 - (N_{\mathrm{c}}/N)^{0.6})$ to the data. We chose this function as it provides a good representation of the predictions for an ideal Bose gas in similar conditions (see methods).

Phase coherence revealed by matter-wave interference. Matter-wave interferences between independent atomic or molecular clouds is a powerful tool to monitor the emergence of extended coherence [14, 142, 166, 175, 223]. To observe these interferences in our uniform setup, we first produced two independent gases of similar density and temperature confined in two coplanar parallel rectangles, separated by a distance of $4.5\,\mu$m along the x direction (see Fig. 4 e). Then we suddenly released the box potential providing confinement in the xy plane, while keeping the confinement along the z direction (2D ToF). The latter point ensures that the atoms stay in focus with our imaging system,

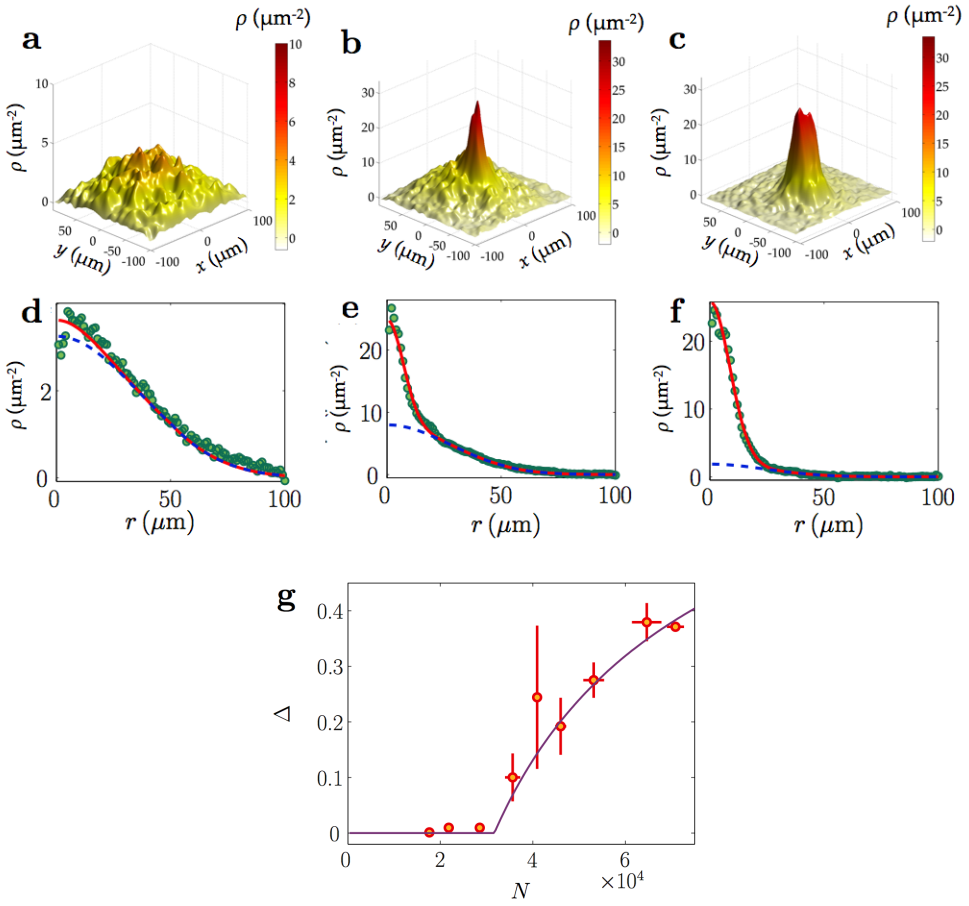

Figure 5. ***Emergence of bimodal velocity distributions.*** *(a-f) Surface density distribution $\rho(x, y)$ (first row) and corresponding radial distributions (green symbols) obtained by azimuthal average (second row). The distribution is measured after a 12 ms time-of-flight for a gas initially confined in a square of size $L = 24\,\mu m$, with a trapping frequency $\nu_z = 365\,Hz$ along the z direction. The temperatures T and atom numbers N for these three realizations are a,d: (155 nK, 28 000), b,e: (155 nK, 38 000), c,f: (31 nK, 19 000). The continuous red lines are fits to the data by a function consisting in the sum of two Gaussians corresponding to N_1 and N_2 atoms ($N = N_1 + N_2$). The Gaussian of largest width (N_2 atoms) is plotted as a blue dashed line. The bimodal parameter $\Delta = N_1/N$ equals a,d: 0.01, b,e: 0.12 and c,f: 0.60. (g) Variation of Δ with N for a gas in the same initial trapping configuration as a-f and for $T = 155\,nK$ (red symbols). Error bars are the standard errors of the mean of the binned data set (with 4 images per point on average). The solid line is a fit to the data by the function $f(N) = (1 - (N_c/N)^{0.6})$ for $N > N_c$, and $f(N) = 0$ for $N \leq N_c$, from which we deduce $N_c(T)$. Here $N_c = 3.2\,(1) \times 10^4$, where the uncertainty range is obtained by a jackknife resampling method,* i.e. *fitting samples corresponding to a randomly chosen fraction of the global data set. Figure from [P8].*

which allows us to observe interference fringes with a good resolution in the region where the two clouds overlap. A typical interference pattern is shown in Fig. 6 a, where the fringes are (roughly) parallel to the y axis, and show some waviness that is linked to the initial phase fluctuations of the two interfering clouds.

We use these interference patterns to characterize quantitatively the level of coherence of the gases initially confined in the rectangles. For each line y of the pixelized image acquired on the CCD camera, we compute the x-Fourier transform $\tilde{\rho}(k, y)$ of the spatial density $\rho(x, y)$ (Fig. 6 b). For a given y this function is peaked at a momentum $k_p(y) > 0$ that may depend (weakly) on the line index y. Then we consider the function that characterizes the correlation of the complex fringe contrast $\tilde{\rho}[k_p(y), y]$ along two lines separated by a distance d

$$\gamma(d) = | \langle \tilde{\rho}[k_p(y), y] \, \tilde{\rho}^*[k_p(y+d), y+d] \rangle | . \tag{8}$$

Here * denotes the complex conjugation and the average is taken over the lines y that overlap with the initial rectangles. If the initial clouds were two infinite, parallel lines with the same $G_1(y)$, one would have $\gamma(d) = |G_1(d)|^2$ [318]. Here the non-zero extension of the rectangles along x and their finite initial size along y make it more difficult to provide an analytic relation between γ and the initial $G_1(r)$ of the gases. However $\gamma(d)$ remains a useful and quantitative tool to characterize the fringe pattern. For a gas described by Boltzmann statistics, the width at $1/e$ of $G_1(r)$ is $\lambda_T/\sqrt{\pi}$ and remains below $1\,\mu$m for the temperature range investigated in this work. Since we are interested in the emergence of coherence over a scale that significantly exceeds this value, we use the following average as a diagnosis tool

$$\Gamma = \langle \gamma(d) \rangle, \text{average taken over the range } 2\,\mu\text{m} < d < 5\,\mu\text{m}. \tag{9}$$

For the parameter Γ to take a value significantly different from 0, one needs a relatively large contrast on each line, and relatively straight fringes over the relevant distances d, so that the phases of the different complex contrasts do not average out.

For a given temperature T, the variation of Γ with N shows the same threshold-type behaviour as the bimodality parameter Δ. One example is given in Fig. 6 c, from which we infer the threshold value for the atom number $N_c(T)$ needed to observe interference fringes with a significant contrast.

Scaling laws for the emergence of coherence. We have plotted in Fig. 7 the ensemble of our results for the threshold value of the total 2D phase-space-density $\mathcal{D}_{\text{tot, c}} \equiv N_c \lambda_T^2/\mathcal{A}$ as a function of $\zeta = k_B T/h\nu_z$, determined both from the onset of bimodality as in Fig. 5 g (closed symbols) or from the onset of visible interference as in Fig. 6 **c** (open symbols). Two trapping configurations have been used along the z direction, $\nu_z = 1460\,\text{Hz}$ and $\nu_z = 365\,\text{Hz}$. In the first case, the z direction is nearly frozen for the temperatures studied here ($\zeta \lesssim 2$). In the second one, the z direction is thermally unfrozen ($\zeta \gtrsim 8$). All points approximately fall on a common curve, independent of the shape and the size of the gas: $\mathcal{D}_{\text{tot, c}}$ varies approximately linearly with ζ with the fitted slope 1.4 (3) for $\zeta \gtrsim 8$ and approaches a finite value ~ 4 for $\zeta \lesssim 2$.

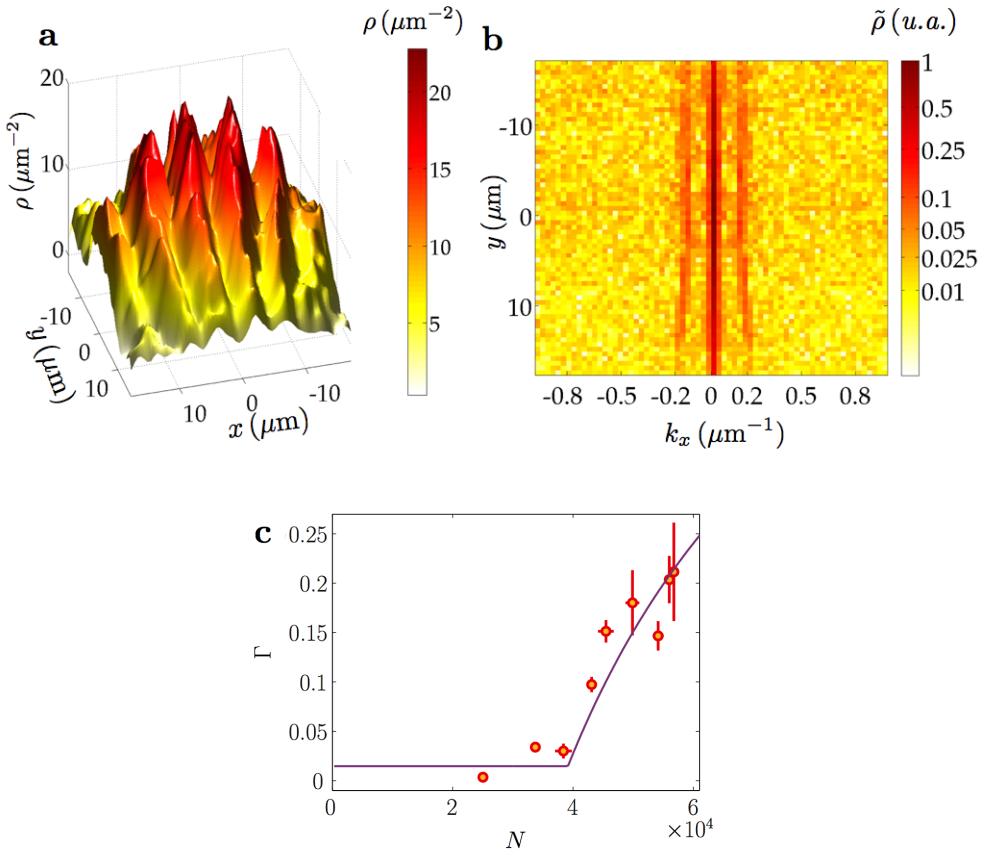

Figure 6. ***Emergence of coherence via matter–wave interference.*** *(a) Example of a density distribution after a 16 ms in–plane expansion of two coplanar clouds initially confined in rectangular boxes of size $24 \times 12\,\mu m^2$, spaced by $d = 4.5\,\mu m$ ($\nu_z = 365\,Hz$). The region of interest considered in our analysis consists of 56 lines and 74 columns (pixel width: $0.52\,\mu m$). (b) Amplitude of the 1D Fourier transform of each line of the density distribution. Each line y shows two characteristic side peaks at $\pm k_p(y)$ above the background noise, corresponding to the fringes pattern of a. Here $\langle k_p \rangle = 0.17(2)\,\mu m^{-1}$. (c) Variation of the average contrast Γ (see text for its definition) for images of gases at $T = 155\,nK$. Error bars show the standard errors of the mean of the binned data set (with on average 3 images per point). The solid line is a fit to the data of the function $f(N)$ defined as $f(N) = b$ for $N \leq N_c$ and $f(N) = b + a\,(1 - (N_c/N)^{0.6})$ for $N > N_c$. The parameter b is a constant for a data set with various T taken in the same experimental conditions. Here we deduce $N_c = 3.9\,(2) \times 10^4$, where the uncertainty range is obtained by a jackknife resampling method. Figure from [P8].*

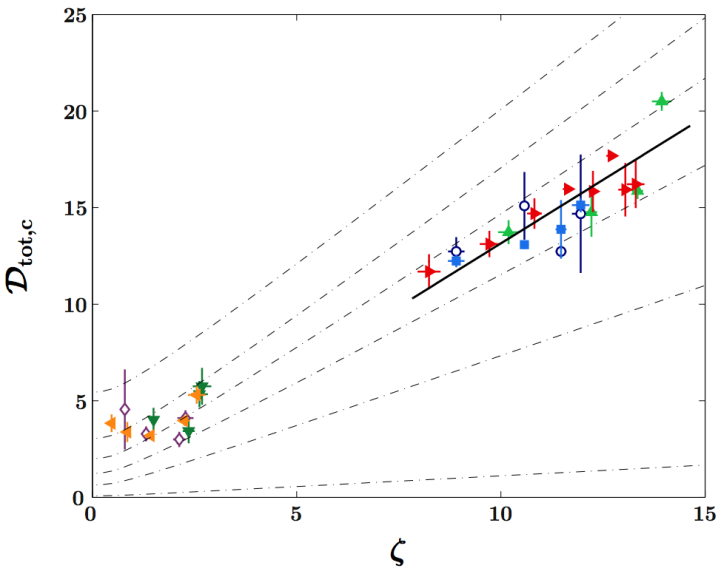

Figure 7. ***Scaling law for the emergence of coherence in a uniform Bose gas in a quasi-2D geometry.*** *Variation of the threshold phase-space-density $\mathcal{D}_{tot,\ c} = N_c\,\lambda_T^2/\mathcal{A}$ for observing a non-Gaussian velocity distribution (full symbols) and distinct matter-wave interferences (open symbols), as a function of the dimensionless parameter $\zeta = k_B T/(h\nu_z)$. For velocity distribution measurements: $\nu_z = 365$ Hz: disk of radius $R = 12\,\mu$m (red left triangles), disk of $R = 9\,\mu$m (light green up triangle), square of $L = 24\,\mu$m (blue square), $\nu_z = 1460$ Hz: disk of $R = 12\,\mu$m (orange right triangles), disk of $R = 9\,\mu$m (dark green down triangles). For interference measurements: $\nu_z = 365$ Hz: dark blue open circles, $\nu_z = 1460$ Hz: violet open diamonds. Error bars show the 95% confidence bounds on the N_c parameter of the threshold fits to the data sets. The black solid line shows a linear fit to the data for $\zeta > 8$, leading to $\mathcal{D}_{tot,\ c} = 1.4\,(3)\,\zeta$. The black dash-dotted lines show contours of identical ratios of the coherence range to the thermal wavelength λ_T. The coherence range is evaluated by the value of r at which $G_1(r) = G_1(0)/20$ (see text) and we plot (in increasing $\mathcal{D}_{tot}$ order) ratios equal to 1, 1.2, 1.5, 2, 3 and 8. Boltzmann prediction corresponds to a ratio of ~ 0.98. Figure from [P8].*

In the frozen case, a majority of atoms occupy the vibrational ground state $j_z = 0$ of the motion along the z direction, so that $\mathcal{D}_{\rm tot}$ essentially represents the 2D phase-space-density associated to this single transverse quantum state. Then for $\mathcal{D}_{\rm tot} \geq 1$, we know from Eq. (7) and the associated discussion that a broad component arises in G_1 with a characteristic length ℓ that increases exponentially with the phase-space-density. The observed onset of extended coherence around $\mathcal{D}_{\rm tot} \sim 4$ can be understood as the place where ℓ starts to exceed significantly λ_T. The regime around $\mathcal{D}_{\rm tot} \sim 4$ is reminiscent of the presuperfluid state identified in [84, 388]. It is different from the truly superfluid phase, which is expected at a higher phase-space-density ($\mathcal{D}_{\rm tot} \sim 8$) for our parameters [322]. Therefore the threshold $\mathcal{D}_{\rm tot,\,c}$ is not associated to a true phase transition, but to a crossover where the spatial coherence of the gas increases rapidly with the control parameter N.

For $\nu_z = 365\,$Hz, the gas is in the "unfrozen regime" ($\zeta \gg 1$), which could be naively thought as irrelevant for 2D physics since according to Boltzmann statistics, many vibrational states along z should be significantly populated. However thanks to the $\mathrm{BEC}_\perp$ phenomenon presented above, a macroscopic fraction of the atoms can accumulate in the $j_z = 0$ state. This happens when the total phase-space-density exceeds the threshold for $\mathrm{BEC}_\perp$:

$$\mathcal{D}_{\rm tot,\,c} \approx \frac{\pi^2}{6}\,\zeta. \tag{10}$$

In the limit $\zeta \to \infty$, $\mathrm{BEC}_\perp$ corresponds to a phase transition of the same nature as the ideal gas BEC in 3D. In the present context of our work, we emphasize that although $\mathrm{BEC}_\perp$ originates from the saturation of the occupation of the excited states along z, it also affects the coherence properties of the gas in the xy plane. In particular when $\mathcal{D}_{\rm tot}$ rises from 0 to $\mathcal{D}_{\rm tot,\,c}$, the coherence length in xy increases from $\sim \lambda_T$ (the non-degenerate result) to $\sim a_z$, the size of the ground state of the z motion. This increase can be interpreted by noting that when $\mathrm{BEC}_\perp$ occurs (Eq. 10), the 3D spatial density in the central plane ($z = 0$) is equal to $g_{3/2}(1)/\lambda_T^3$, where g_s is the polylogarithm of order s and $g_{3/2}(1) \approx 2.612$. For an infinite uniform 3D Bose gas with this density, a true Bose-Einstein condensation occurs and the coherence length diverges. Because of the confinement along the z direction, such a divergence cannot occur in the present quasi-2D case. Instead, the coherence length along z is by essence limited to the size a_z of the $j_z = 0$ state. When $\mathcal{D}_{\rm tot} = \mathcal{D}_{\rm tot,\,c}$ the same limitation applies in the transverse plane, giving rise to coherence volumes that are grossly speaking isotropic. When $\mathcal{D}_{\rm tot}$ is increased further, the coherence length in the xy plane increases, while remaining limited to a_z along the z direction. The results shown in Fig. 7 are in line with this reasoning. For $\zeta \gg 1$, the emergence of coherence in the xy plane occurs for a total phase-space-density $\mathcal{D}_{\rm tot,\,c} \propto \zeta$, with a proportionality coefficient $\alpha = 1.4\,(3)$ in good agreement with the prediction $\pi^2/6 \approx 1.6$ of Eq. (10).

We have also plotted in Fig. 7 contour lines characterizing the coherence range in terms of ζ and $\mathcal{D}_{\rm tot}$. Using ideal Bose gas theory, we calculated the one-body coherence function $G_1(r)$ and determined the distance r_f over which it decreases by a given factor f with respect to $G_1(0)$. We choose the value $f = 20$ to explore the long tail that develops

in G_1 when phase coherence emerges. The contour lines shown in Fig. 7 correspond to given values of r_{20}/λ_T they should not be considered as fits to the data, but as an indication of a coherence significantly larger than the one obtained from Boltzmann statistics (for which $r_{20} \approx \lambda_T$). The fact that the threshold phase-space densities $\mathcal{D}_{\mathrm{tot,\,c}}$ follow quite accurately these contour lines validates the choice of tools (non Gaussian velocity distributions, matter-wave interferences) to characterize the onset of coherence.

Observation of topological defects. From now on we use the weak trap along z ($\nu_z = 365\,\mathrm{Hz}$) so that the onset of extended coherence is obtained thanks to the transverse condensation phenomenon. We are interested in the regime of strongly degenerate, interacting gases, which is obtained by pushing the evaporation down to a point where the residual thermal energy $k_B T$ becomes lower than the chemical potential μ (see methods for the calculation of μ in this regime). The final box potential is $\sim k_B \times 40\,\mathrm{nK}$, leading to an estimated temperature of $\sim 10\,\mathrm{nK}$, whereas the final density ($\sim 50\,\mu\mathrm{m}^{-2}$) leads to $\mu \approx k_B \times 14\,\mathrm{nK}$. In these conditions, for most realizations of the experiment, defects are present in the gas. They appear as randomly located density holes after a short 3D ToF (Fig. 8 a,b), with a number fluctuating between 0 and 5. To identify the nature of these defects, we have performed a statistical analysis of their size and contrast, as a function of their location and of the ToF duration τ (Fig 8 c,d). For a given τ, all observed holes have similar sizes and contrasts. The core size increases approximately linearly with τ, with a nearly 100 % contrast. This favors the interpretation of these density holes as single vortices, for which the 2π phase winding around the core provides a topological protection during the ToF. This would be the case neither for vortex–antivortex pairs nor phonons, for which one would expect large fluctuations in the defect sizes and lower contrasts.

Dynamical origin of the topological defects. In principle the vortices observed in the gas could be due to steady-state thermal fluctuations. BKT theory indeed predicts that vortices should be present in an interacting 2D Bose gas around the superfluid transition point [229]. Such "thermal" vortices have been observed in non-homogeneous atomic gases, either interferometrically [166] or as density holes in the trap region corresponding to the critical region [79]. However, for the large and uniform phase-space densities that we obtain at the end of the cooling process ($\rho\lambda_T^2 \geq 100$), Ref. [146] predicts a vanishingly small probability of occurrence for such thermal excitations. This supports a dynamical origin for the observed defects.

To investigate further this interpretation, we can vary the two times that characterize the evolution of the gas, the duration of evaporation t_{evap} and the hold duration after evaporation t_{hold} (see Fig. 4 a). For the results presented in this section, we fixed $t_{\mathrm{hold}} = 500\,\mathrm{ms}$ and studied the evolution of the average vortex number N_{v} as a function of t_{evap}. The corresponding data, given in Fig. 9 a, show a decrease of N_{v} with t_{evap}, passing from $N_{\mathrm{v}} \approx 1$ for $t_{\mathrm{evap}} = 50\,\mathrm{ms}$ to $N_{\mathrm{v}} \approx 0.3$ for $t_{\mathrm{evap}} = 250\,\mathrm{ms}$. For longer evaporation times, N_{v} remains approximately constant around 0.35 (5).

The decrease of N_{v} with t_{evap} suggests that the observed vortices are nucleated via a

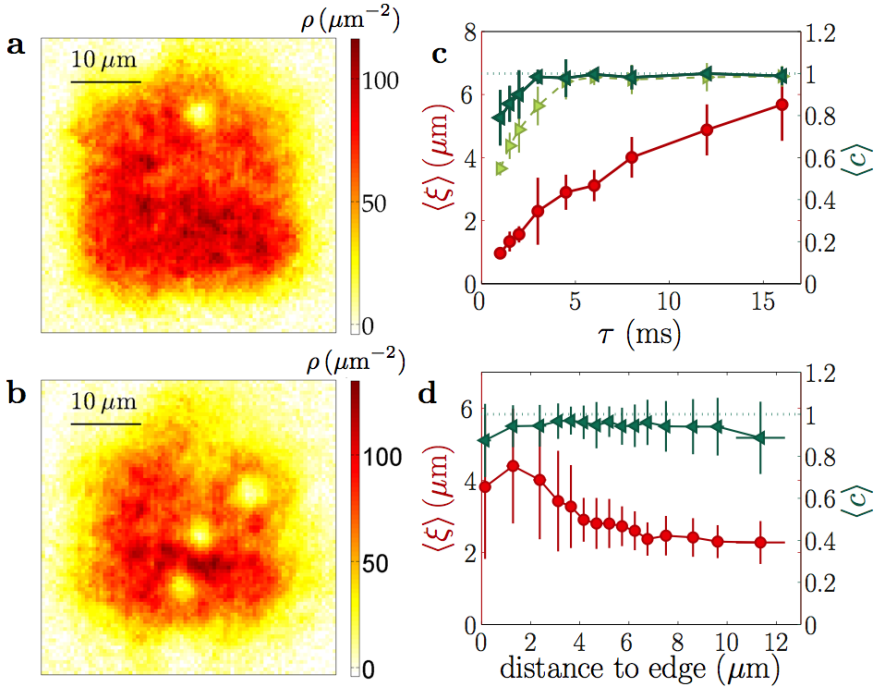

Figure 8. ***Observation of vortices***. *(a,b) Examples of density distributions after a 3D ToF of $\tau = 4.5\,ms$ for a gas initially confined in a square of size $L = 30\,\mu m$ ($\nu_z = 365\,Hz$). The two examples show respectively one (a) and three (b) holes of high contrast, corresponding to topologically protected expanding vortex cores. We fit each density hole by a hyperbolic tangent dip convoluted by a Gaussian of waist $w = 1\,\mu m$ accounting for imaging imperfections (see methods). (c) Evolution of the average size ξ (red circles, left labels) and contrast c (green triangles, right labels) of density holes with the expansion duration τ. No holes are visible for $\tau \lesssim 0.5\,ms$. Red circles and dark green left triangles are results from a fit accounting for imaging imperfections while light green right triangles show contrast resulting from a fit without a convolution by a Gaussian. (d) Variation of the hole size ξ (red circles, left labels) and contrast c (green triangles, right labels) with the distance to the nearest edge of the box (same configuration than a,b: ToF of $\tau = 4.5\,ms$ for a gas in a square of $L = 30\,\mu m$). For a distance larger than $\sim 4\,\mu m$, ξ and c are approximately independent from the vortex location. The average values in c are taken over all holes independent of their positions. One point in c (resp. d) corresponds to 15 (resp. 70) vortex fits. Error bars show standard deviations of the binned data set. Figure from [P8].*

Kibble–Zurek (KZ) type mechanism [15, 210, 427], occurring when the transition to the phase coherent regime is crossed. However applying the KZ formalism to our setup is not straightforward. In a weakly interacting, homogeneous 3D Bose gas, BEC occurs when the 3D phase-space-density reaches the critical value $g_{3/2}(1)$. For our quasi-2D geometry, transverse condensation occurs when the 3D phase-space-density in the central plane $z = 0$ reaches this value. At the transition point, the KZ formalism relates the size of phase-coherent domains to the cooling speed $\dot{T}$. For fast cooling, KZ theory predicts domain sizes for a 3D fluid that are smaller than or comparable to the thickness a_z of the lowest vibrational state along z; it can thus provide a good description of our system. For a slower cooling, coherent domains much larger than a_z would be expected in 3D at the transition point. The 2D nature of our gas leads in this case to a reduction of the in-plane correlation length. In the slow cooling regime, we thus expect to find an excess of topological defects with respect to the KZ prediction for standard 3D BEC.

More explicitly we expect for fast cooling, hence short t_{evap}, a power-law decay $N_{\mathrm{v}} \propto t_{\mathrm{evap}}^{-d}$ with an exponent d given by the KZ formalism for 3D BEC. The fit of this function to the measured variation of N_{v} for $t_{\mathrm{evap}} \leq 250\,\mathrm{ms}$ leads to $d = 0.69\,(17)$ (see Fig. 9 a). This is in good agreement with the prediction $d = 2/3$ obtained from the critical exponents of the so-called "F model" [177], which is believed to describe the universality class of the 3D BEC phenomenon. For comparison, the prediction for a pure mean-field transition, $d = 1/2$, is notably lower than our result.

For longer t_{evap}, the above described excess of vortices due to the quasi-2D geometry should translate in a weakening of the decrease of N_{v} with t_{evap}. The non-zero plateau observed in Fig. 9 a for $t_{\mathrm{evap}} \geq 250\,\mathrm{ms}$ may be the signature of such a weakening. Other mechanisms could also play a role in the nucleation of vortices for slow cooling. For example due to the box potential residual rugosity, the gas could condense into several independent patches of fixed geometry, which would merge later during the evaporation ramp and stochastically form vortices with a constant probability.

Lifetime of the topological defects. The variation of the number of vortices N_{v} with the hold time t_{hold} allows one to study the fate of vortices that have been nucleated during the evaporation. We show in Fig. 9 b the results obtained when fixing the evaporation to a short value $t_{\mathrm{evap}} = 50\,\mathrm{ms}$. We observe a decay of N_{v} with the hold time, from $N_{\mathrm{v}} = 2.3$ initially to 0.3 at long t_{hold} (2 s). To interpret this decay, we modeled the dynamics of the vortices in the gas with two ingredients: (i) the conservative motion of a vortex in the velocity field created by the other vortices, including the vortex images from the boundaries of the box potential [110], (ii) the dissipation induced by the scattering of thermal excitations by the vortices, which we describe phenomenologically by a friction force that is proportional to the non-superfluid fraction of atoms in the gas [128]. During this motion, a vortex annihilates when it reaches the edge of the trap or encounters another vortex of opposite charge. The numerical solution of this model leads to a non-exponential decay of the average number of vortices, with details that depend on the initial number of vortices and their locations.

Assuming a uniform random distribution of vortices at the end of the evaporation,

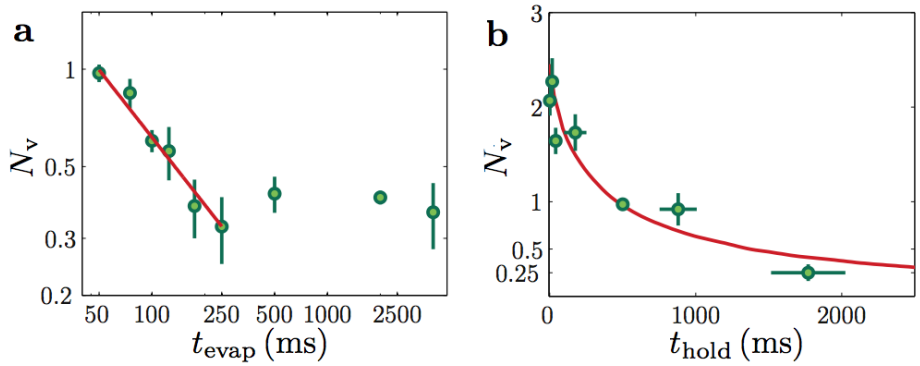

Figure 9. ***Dynamics of vortex nucleation.*** *(a) Circle symbols: evolution of the mean vortex number N_v with the quench time t_{evap} (fixed $t_{hold} = 500\,ms$) for a gas initially confined in a square of size $L = 30\,\mu m$ ($\nu_z = 365\,Hz$) and observed after a 3D ToF of $\tau = 4.5\,ms$. The number of images per point ranges from 37 to 233, with a mean of 90. We restrict to $t_{evap} \geq 50\,ms$ to ensure that local thermal equilibrium is reached at any time during the evaporation ramp [208]. Red line: fit of a power-law decay to the short time data ($t_{evap} \leq 250\,ms$), giving the exponent $d = 0.69\,(17)$. The uncertainty range on d is the 95% confidence bounds of a linear fit to the evolution of $\log(N_v)$ with $\log(t_{evap})$. For longer quench times, the mean vortex numbers are compatible with a plateau at $N_v = 0.35\,(5)$. (b) Circle symbols: evolution of the mean vortex number N_v with the hold time t_{hold} (fixed $t_{evap} = 50\,ms$) in the same experimental configuration as a. The number of images per point ranges from 24 to 181, with a mean of 59. In both figures error bars are obtained from a bootstrapping approach. Red line: results from a model describing the evolution of an initial number of vortices $N_{v,0} = 2.5(2)$ in the presence of a phenomenological damping coefficient [128]. The inferred superfluid fraction is $0.94\,(2)$. Confidence ranges on these parameters are obtained from a χ^2-analysis. Figure from [P8].*

we have compared the predictions of this model to our data. It gives the following values of the two adjustable parameters of the model, the initial number of vortices $N_{\mathrm{v},0} = 2.5\,(2)$ and the superfluid fraction $0.94\,(2)$; the corresponding prediction is plotted as a continuous line in Fig. 9 b. We note that at short t_{hold}, the images of the clouds are quite fuzzy, probably because of non-thermal phononic excitations produced (in addition to vortices) by the evaporation ramp. The difficulty to precisely count vortices in this case leads to fluctuations of N_{v} at short t_{hold} as visible in Fig. 9 b. The choice $t_{\mathrm{hold}} = 500\,\mathrm{ms}$ in Fig. 9 a was made accordingly.

The finite lifetime of the vortices in our sample points to a general issue that one faces in the experimental studies on the KZ mechanism. In principle the KZ formalism gives a prediction on the state of the system just after crossing the critical point. Experimentally we observe the system at a later stage, at a moment when the various domains have merged, and we detect the topological defects formed from this merging. In spite of their robustness, the number of vortices is not strictly conserved after the crossing of the transition and its decrease depends on their initial positions. A precise comparison between our results and KZ theory should take this evolution into account, for example using stochastic mean-field methods [45, 87, 98, 262].

Discussion

Using a box-like potential created by light, we developed a setup that allowed us to investigate the quantum properties of atomic gases in a uniform quasi-2D configuration. Thanks to the precise control of atom number and temperature, we characterized the regime for which phase coherence emerges in the fluid. The uniform character of the gas allowed us to disentangle the effects of ideal gas statistics for in-plane motion, the notion of transverse condensation along the strongly confined direction, and the role of interactions. This is to be contrasted with previous studies that were performed in the presence of a harmonic confinement in the plane, where these different phenomena could be simultaneously present in the non-homogeneous atomic cloud.

For the case of a weakly interacting gas considered here, our observations highlight the importance of Bose statistics in the emergence of extended phase coherence. This coherence is already significant for phase-space densities $\mathcal{D}_0 \sim 3 - 4$, well below the values required for (i) the superfluid BKT transition and (ii) the full Bose–Einstein condensation in the ground state of the box. For our parameters, the latter transitions are expected around the same phase-space-density ($\sim 8 - 10$) meaning that when the superfluid criterion is met, the coherence length set by Bose statistics is comparable to the box size.

By cooling the gas further, we entered the regime where interactions dominate over thermal fluctuations. This allowed us to visualize with a very good contrast the topological defects (vortices) that are created during the formation of the macroscopic matter-wave, as a result of a Kibble–Zurek type mechanism. Here we focused on the relation between the vortex number and the cooling rate. Further investigations could include correlation studies on vortex positions, which can shed light on their nucleation process and their

subsequent evolution [138].

Our work motivates future research in the direction of strongly interacting 2D gases [164], for which the order of the various transitions could be interchanged. In particular the critical $\mathcal{D}$ for the BKT transition should decrease, and reach ultimately the universal value of the "superfluid jump", $\mathcal{D} = 4$ [293]. In this case, the emergence of extended coherence in the 2D gas would be essentially driven by the interactions. Indeed once the superfluid transition is crossed, the one-body correlation function is expected to decay very slowly, $G_1(r) \propto r^{-\alpha}$, with $\alpha < 1/4$. It would be interesting to revisit the statistics of formation of quench-induced topological defects in this case, for which significant deviations to the KZ power-law scaling have been predicted [111, 194].

Here, we skip a "Methods" section detailing all elements necessary to allow interpretation and replication of the results.

2.2.3. Vortex reconnections and rebounds in trapped atomic Bose–Einstein condensates [P6]

Abstract: Reconnections and interactions of filamentary coherent structures play a fundamental role in the dynamics of fluids, redistributing energy and helicity among the length scales and inducing fine-scale turbulent mixing. Unlike ordinary fluids, where vorticity is a continuous field, in quantum fluids vorticity is concentrated into discrete (quantized) vortex lines turning vortex reconnections into isolated events, making it conceptually easier to study. Here we report experimental and numerical observations of three-dimensional quantum vortex interactions in a cigar-shaped atomic Bose–Einstein Condensate. In addition to standard reconnections, already numerically and experimentally observed in homogeneous systems away from boundaries, we show that double reconnections, rebounds and ejections can also occur as a consequence of the non-homogeneous, confined nature of the system.

Introduction

The interaction and reconnection of filaments are key aspects in the description of the dynamics of fluids [28, 211, 357], plasmas [72, 83, 321], nematic liquid crystals [82], macromolecules [377] (including DNA [394]) and optical beams [39, 105]. In quantum fluids, vortices are topological defects of the system's order parameter, around which the circulation of the velocity field is quantized [110, 132, 301, 399]. Their discrete filamentary nature makes quantum fluids an ideal setting for the study of vortex interactions and reconnections. In particular, reconnections trigger a turbulent energy cascade [29] in which vortex lines self-organize in bundles [20] creating the same Kolmogorov distribution of kinetic energy over the length scales, signature of a cascade mechanism which is observed in ordinary turbulence [29, 264, 297, 367]. Cascade processes are central in turbulent motions. A related cascade of wave-like excitations was in fact recently observed in the momentum distribution [289], with an exponent consistent with predictions of

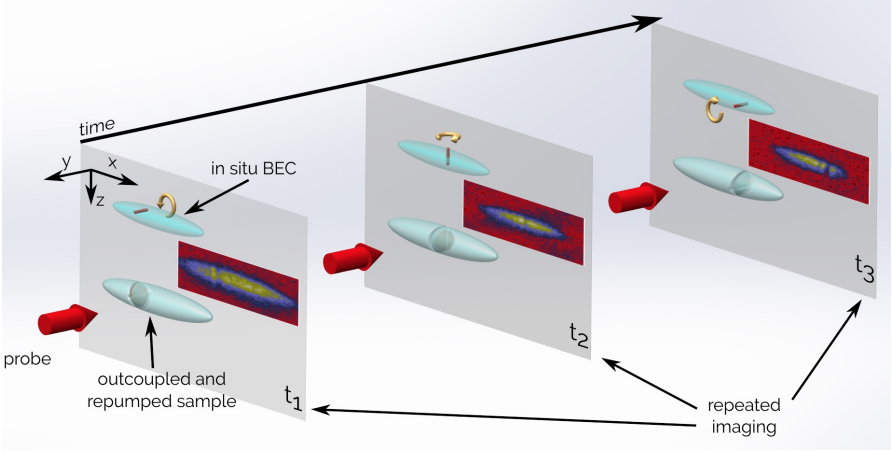

Figure 10. *Sketch of an imaging sequence. A trapped condensate (smaller light-blue ellipsoid) contains a transverse vortex line that moves and rotates around the trap center; the direction of the atomic flow around the vortex filament is indicated by the yellow arrow. A small fraction of atoms is repeatedly extracted, typically every 12 ms; these atoms expand and fall in the gravity field, and are imaged in absorption by a probe laser beam after they are spatially separated from the trapped condensate. Each absorption image contains the essential features associated with the vortex lines. Figure from [P6].*

wave-turbulence theory [419]. Reconnection events also impact on the evolution of the flow's topology [218], redistributing helicity among length scales [86, 351]. Finally, in the low-temperature limit, reconnections are the ultimate process of dissipation of superfluid kinetic energy since they trigger a Kelvin wave cascade [230, 231] that turns incompressible kinetic energy into acoustic modes [247], hence heating. Previous experimental [41, 136], theoretical [290] and numerical [102, 207, 227, 335, 382, 398, 426] studies of reconnections have been performed in homogeneous systems away from boundaries.

Here we focus on elongated Bose–Einstein condensates (BECs) of ultracold atoms confined by magnetic harmonic potentials, ideal systems which allow for different regimes of three-dimensional (3D) vortex-vortex interactions in the close presence of boundaries. Anisotropic boundaries induce vortical filaments to preferentially align along the shortest direction, minimising energy. In flat, cylindrically symmetric, disk-shaped condensates, vortices are the shortest when aligned along the axis of symmetry, moving along two-dimensional trajectories clockwise or anti-clockwise, depending on their sign [11, 138, 288, 292, 384, 406]. Instead, vortices in cylindrically symmetric, cigar-shaped condensates are the shortest when they lie on radial planes. Moreover, the boundaries affect the structure of the vortical flow [56, 109, 226, 389] in such a way that two vortices only interact when their minimum distance is within a range of the order of the transverse size of the condensate.

In the present work, an innovative imaging technique, exploiting self-interference effects of outcoupled atoms, is introduced in order to extract both the position and orientation of 3D vortex lines from a temporal sequence of absorption images. We then

combine experiments and numerical Gross-Pitaevskii (GP) simulations to study the interaction between two vortex lines approaching at various relative speeds and angles. Our experiments and simulations show that the interaction between vortex lines in a finite system is rather different from the one in infinite uniform superfluids. Boundary-induced effects, such as rebounds, double reconnections, and ejections, are here discussed in details. These types of processes may play an important role in the dynamics of trapped condensates in multi-vortex and turbulent-like configurations, and, on a wider perspective, they can represent novel keys for better understanding the behavior of superfluids near boundaries.

Experiment

Preparation of BECs with vortices. Experimentally, we confine sodium atoms in an elongated cigar-shaped harmonic magnetic trap with axial and radial frequencies $\omega_x/2\pi = 9.2$ Hz and $\omega_\perp/2\pi = 92$ Hz, respectively. By means of a radio-frequency forced evaporation the cold atomic sample undergoes the BEC transition and, in the end, condensates containing about $N_0 = 2 \times 10^7$ atoms and a negligible thermal fraction ($T < 150$ nK, $T_c \simeq 500$ nK) are obtained. Thanks to the Kibble–Zurek mechanism [210, 428] the temperature quench through the BEC transition [108, 138, 240, 406] produces different phase domains in the order parameter of the system that quickly evolve into topological defects. In our geometry, these defects are vortex lines mainly oriented in the transverse direction, as those predicted in [56, 226] and characterized in [109]. Similar vortices can be obtained as decay products of phase imprinted dark solitons in a BEC [34] or a Fermi superfluid gas [234, 235]. Here we use a cooling rate of 4 μK/s in order to produce, on average, two vortices in each condensate at the time when the observation starts, about 250 ms after the phase transition. Such vortices move in the non-rotating condensate and can be directly imaged in real-time [138, 328, 359]. In comparison, individual vortex visualisation in superfluid helium is more intrusive, requiring tracer particles whose diameter is about 10^4 times larger than the vortex core [40].

Sample extraction and real-time imaging. A new imaging method allows us to follow the vortex dynamics in real-time, as sketched in Fig. 10. Similar to [138, 328], a small sample of the atomic system ($\sim 10^5$ atoms) is repeatedly extracted from the BEC every 12 ms (up to 75 times). The outcoupled atoms freely expand and fall under the effect of gravity. Each partial extraction is implemented by coupling the trapped state $|F = 1, m_F = -1\rangle$ to the non-magnetic one $|1, 0\rangle$ with a radio frequency (rf) field. The energy difference between the two states is spatially dependent because of the inhomogeneity of the trapping potential.

The novelty of our technique is represented by the fact that the rf field is frequency-swept linearly in time in order to match the resonant condition at different positions throughout the BEC, from top to bottom. An important point to note is that the phase of the released atoms evolves more slowly because they do not feel the trapping potential.

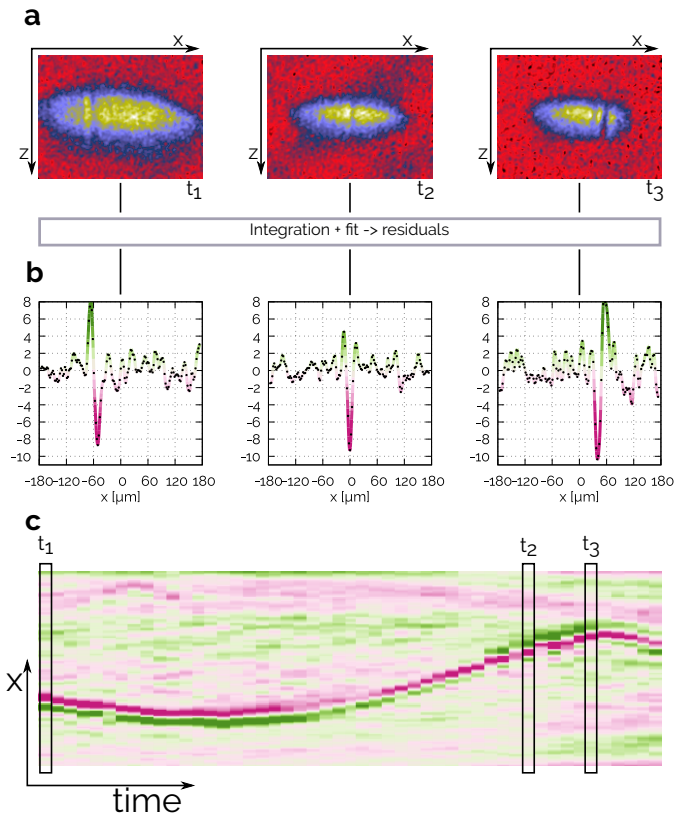

Figure 11. *(a) Examples of absorption images of the outcoupled atoms (the same as in Fig. 10). The vortex axial position is clearly visible. (b) After integrating radially and fitting the absorption images, we determine the residuals, which exhibit minima (pink) and maxima (green) due to interference effects among atoms that are outcoupled from the trapped condensate at different places and times. (c) Full temporal sequence of residuals for a given condensate, showing the real-time evolution of a vortex which moves axially and rotates around the x axis, from an initial orientation along y (green-pink) at t_1 to an orientation along z (green-pink-green) in t_2 and then along $-y$ (pink-green) at t_3. The relation between the shape of the residuals and the orientation of the vortex is extracted from numerical simulations. Figure from [P6].*

As a consequence, the wave function of the outcoupled atoms experiences constructive or destructive self-interference effects, depending on the phase difference accumulated between the early-released (upper) and late-released (lower) atoms, and how this relates to the *in situ* phase on different sides of the vortex core. We use the GP equation to simulate the radio frequency extraction in order to determine how a vortex with given position and orientation in the trapped BEC manifests itself in the observed density distribution of the outcoupled atoms after expansion.

A microwave field remains on to transfer the extracted atoms from $|1,0\rangle$ to $|2,0\rangle$, which is detectable with the probe light. The resonant condition for the transfer is matched at $z_r \approx 280\,\mu$m below the trapped BEC, far enough to leave it unaffected. We probe the

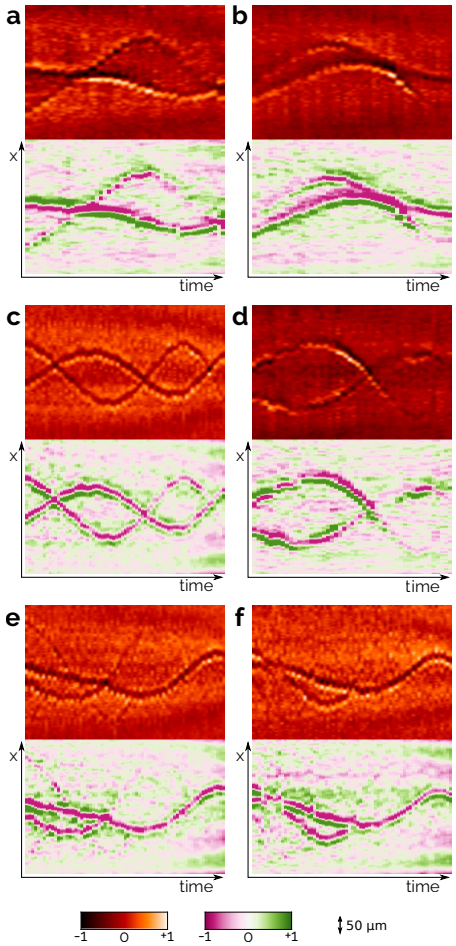

Figure 12. *Examples of different interaction mechanisms observed in the case of two approaching vortices. Each temporal sequence is shown twice with two different color palettes; the red palette enhances the contrast, so that also vortices close to the edges can be seen, whereas the pink-green palette better illustrates the vortex orientation in the radial plane. (a,b) Vortices approach and bounce back; (c) their axial trajectories intersect preserving visibility and orientation; (d) they cross producing sudden changes of visibility; (e,f) the visibility of one vortex is almost completely lost after interacting with the other. Figure from [P6].*

extracted atoms via standard absorption imaging after 13 ms of total time of flight at $z_i \approx 830\,\mu$m below the trap center. Such a time of flight is enough for vortices to become visible with our imaging resolution.

Data analysis. Each absorption image (Fig. 11a) is integrated radially along the z axis and the axial profile is obtained. By fitting the latter, we calculate the density residuals (see Fig. 11b). This procedure is performed on each extraction and then the full temporal sequence is reconstructed in order to follow the vortex trajectories in the

trapped condensate, as in Fig. 11c.

Thanks to the above mentioned self-interference effect, if a vortex is present, the density residuals show a strong local deviation from the unperturbed distribution, as in Fig. 11b, and the fit allows us to extract information on the vortex axial position, as well as on its orientation in the radial plane at any given time.

Figure 12 shows examples of the temporal evolution of the density-residual profiles in BECs containing two vortices. Two different color palettes are used in order to extract different pieces of information. The red palette best highlights the trajectory contrast. One can track the vortex axial location in time and hence determine the orbit amplitude and the axial velocity. Notice that in some cases, very faint trajectories (corresponding to vortices close to the BEC surface) can also be seen. It is also possible to understand how the vortex line is oriented in the radial plane and how it rotates about the long axis of the condensate. The diverging pink-green palette helps to visualize the shape of the density modulation from which one can better track the vortex orientation in time. From numerical simulations we infer that, at least when the orbiting parameter is not too large, the vorticity points along y if the interference pattern is green-pink along x (see row (b) in Fig. 11); its anti-vortex configuration, oriented toward $-y$, corresponds to a pink-green pattern; the symmetric pattern green-pink-green is obtained when the vortex is aligned perpendicularly to the imaging direction, a vortex oriented along $+z$ providing the same density residual as one oriented along $-z$.

Numerical simulations

In order to gain closer insight into vortex interactions, we perform numerical simulations by using the Gross–Pitaevskii equation [96, 317] for a BEC at $T = 0$. Temperature effects are expected to be small. In a previous work [359], we have already observed that the dynamics of single vortices is very weakly affected by thermal excitations. This is expected to be true also for vortex-vortex interaction processes occurring in the central region of our BEC, where the thermal density is negligible. There is also evidence that thermal excitations do not affect the rapid motion of vortex lines during the reconnections [8].

We track the vortices by employing an algorithm based on the pseudo-vorticity vector, achieving sub-grid resolution. Since the experimental BECs are too large for our computational resources, we simulate smaller BECs ($\sim 4 \times 10^5$ atoms); this implies a reduction of the ratio $R_\perp/\xi$ by a factor of three, where ξ is the healing length and $R_\perp$ is the transverse Thomas–Fermi radius. However, such a difference does not affect the qualitative comparison between experiments and simulations.

If we imprint a single straight vortex line off-center on a radial plane, we find that it orbits around the center of the condensate [11, 138] along an elliptical orbit which is orthogonal to the vortex line itself. The orbit, which is a trajectory of constant energy [379] and an isoline of the trapping potential, is uniquely determined by the orbit parameter $\chi = r_0/R_\perp = x_0/R_x$, where r_0 and x_0 correspond to the radial and axial semi-axes of the ellipse, while R_x is the axial Thomas–Fermi radius. The orbital period is

maximum when the vortex moves on a very small orbit ($\chi \ll 1$) and corresponds to $T_0 = 8\pi\mu/[3\hbar\omega_\perp\omega_x \ln(R_\perp/\xi)]$ [359], while it decreases with increasing χ [131, 256, 360, 379].

If instead we imprint two transverse vortices in a given BEC, we find that the evolution can be divided into two stages. In the first stage, when the axial separation of the vortices is larger than $R_\perp$, the vortices move almost independently; in the second stage, when the axial separation becomes smaller than $R_\perp$, we observe a significant interaction which seems to be determined mainly by the relative orientation $\theta_{\rm rel}$ and velocity $v_{\rm rel}$ when they start interacting.

We first perform simulations in which two orthogonal vortices are initially imprinted in radial planes at opposite axial positions $\pm x_0$, see Figs. 13a-c (orthogonality is chosen because of its maximal dissimilarity with respect to flat 2D systems). Different x_0 values are chosen, corresponding to different orbit parameters χ and hence to different impact velocities. The early stage can be described as the combination of two single-vortex motions on mutually perpendicular elliptical orbits.

In fact, in an elongated condensate, the superfluid flow of each vortex becomes negligible at distances of the order of $R_\perp$ from the line, as can be verified by solving the stationary GP equation. This means that when two vortices are at distances larger than $\sim R_\perp$, they behave as non-interacting objects, as indeed observed in time-dependent GP simulations. This is crucial in order to interpret and classify the vortex-vortex interaction as a collision with well-defined initial and final velocities and orientations. In a different 3D geometry, it would be very difficult to define and control a global "relative velocity and orientation" of a vortex line. If a non-rotating condensate is confined in a spherical potential, or is uniform, for instance, the distance between two vortices and their relative velocity and orientation could be defined only locally: vortices do not possess a preferred orientation, they can be easily bent, and each piece of vortex is affected by a long-range interaction with all other vortices in the condensate. Our geometry instead naturally provides well-defined collision events, such as reconnecting or bouncing lines, occurring in a narrow interaction region.

Only when the minimum distance between the vortices becomes of the order of $R_\perp$, the vortices start rotating in the radial plane, attempting to arrange themselves in the preferred (energy-conserving) anti-parallel configuration, as shown in Figs. 13a-c. The axial motion of the vortices towards each other, driven by the inhomogeneous density, is faster if the vortices are close to the condensate's boundary [131, 360, 379]. The anti-parallel configuration which the vortices attempt to achieve induces them to drift radially towards the radial center of the condensate. This drift is similar to the well-known self-induced motion of a pair of straight anti-parallel vortex lines [271, 292, 384] in a homogeneous condensate. The balance between the radial and axial motions which we have described determines the features of the second stage of the interaction.

Briefly, if the axial collision velocity is sufficiently high (*i.e.*, if the vortex lines start interacting in a region sufficiently close to the boundary [131, 360, 379]) the two vortices tend to reconnect before reaching the center of the condensate, as in Fig. 13c.

Vice versa, if the interaction begins in a region sufficiently close to the x-axis, the radial motion of the vortex lines is fast enough (with respect to the axial motion) to get

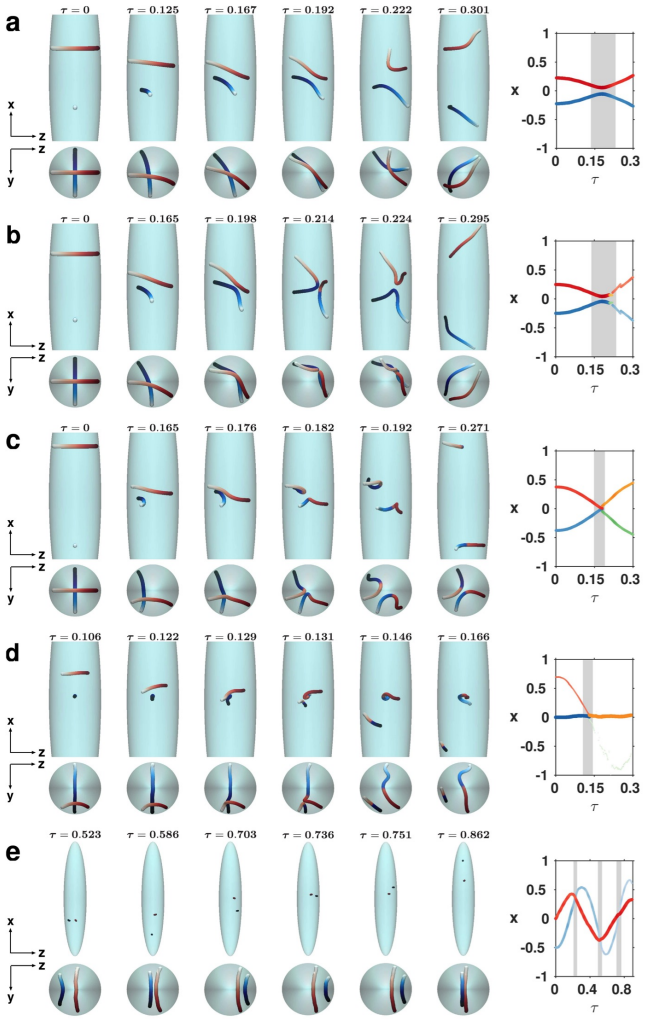

Figure 13. *The first six columns show radial and axial snapshots from the GP simulations of two interacting vortex lines. On the right, the axial coordinate x (in units of R_x) of the center of vorticity of each vortex is plotted vs. normalized time $\tau = t/T_0$. Initial line colors (red/blue) help identify vortices in the snapshots until they reconnect. After the first reconnection, line colors switch to orange/green and again to red/blue if a second reconnection occurs. Line transparency indicates how visible vortices are expected to be, given their orbit amplitude (see Appendix B for further details on line transparency). The grey region highlights the interaction interval where the minimum distance between the vortices is smaller than $R_\perp$. (a-c) Perpendicular vortices are imprinted on opposite radial planes with corresponding orbit parameters $\chi = 0.22, 0.25, 0.375$, respectively: (a) illustrates a vortex rebound; (b) shows the double reconnection interaction, with reconnections occurring at $\tau = 0.208$ and $\tau = 0.221$; (c) depicts a single reconnection occurring at $\tau = 0.179$, with the consequent triggering of Kelvin waves. (d) illustrates a non-symmetrical reconnection (at $\tau = 0.130$) between a vortex imprinted on the central plane of the condensate through its center (blue) and a vortex (red) imprinted orthogonally to the first one with a large orbit parameter $\chi = 0.7$. One of the reconnected vortices lies on an even wider orbit (larger χ), where the BEC density is lower and its visibility becomes consequently greatly reduced. (e) describes the orbiting dynamics between two parallel vortices imprinted on different orbits ($\chi = 0.33, 0.5$). Notice that in (a-c) the first snapshot corresponds to $\tau = 0$, whereas in (d,f) the snapshots are all later in time. Figure from [P6].*

past the radial center of the condensate where they move axially away from each other due to the reversed velocity field induced by the inhomogeneous density: a rebound takes place, as in Fig. 13a.

An intermediate regime occurs if, while drifting radially away from the boundary of the condensate towards the center, the minimum distance between the vortices in the central region of the condensate is sufficiently small: in this case a double reconnection [39] occurs. This happens for instance in the sequence in Fig. 13b, where the two vortex lines touch at a point and exchange their tails both at $\tau = 0.208$ and $\tau = 0.221$, expressed in units of the precession period T_0.

In addition to the simulations with chemical potential $\mu = 10\hbar\omega_\perp$, we have also performed simulations with $\mu = 5\hbar\omega_\perp$. The corresponding dynamics are very similar and the sole discriminant parameter between the distinct vortex interaction regimes is indeed the orbit parameter χ. The critical value χ_c switching from rebound to double reconnection dynamics is $0.25 < \chi_c < 0.28$ for $\mu = 5$ and $0.22 < \chi_c < 0.25$ for $\mu = 10$, supporting our argument that the value of μ does not change the essence of the physics.

Interpretation of the results

Rebounds. The simulations in Fig. 13a show that rebound events are characterized by non intersecting vortex trajectories, as we observe experimentally in a subset of images, e.g. in Fig. 12a,b. For example, Fig. 13a can be related to Fig. 12b, where the orientations extracted from the residuals start from an orthogonal configuration before partially overlapping (however the trajectories do not intersect) and then emerge later showing an anti-parallel configuration. A simpler, non-rotational, bounce is the one in Fig. 12a, where vortices are already anti-parallel before interacting. Both of the observed rebounds are characterized by an increased visibility when vortices are very close to each other. This is because the residuals are generated by subtracting the unperturbed density distributions and vortices become more visible where their cores lie within a region of higher density. The observed increase of vortex visibility in rebound events is thus consistent with the radial drift of the vortices towards the x-axis seen in numerical simulations.

By studying the dynamics of hundreds of different experimental realisations, we make a statistical analysis which reinforces our interpretation. Figure 14a shows the distribution of events as a function of the relative axial velocity of two approaching vortices. It is evident that those events, that are identified as rebounds (with approaching, but not touching, trajectories), preferentially happen when the relative velocity is small. As anticipated, the relative angle θ_{rel} in the radial plane matters when discerning rebound events from reconnections. Fig. 14b shows the rebound probability as a function of the vortex relative angle just before their approach. In order to classify the events in the three bins of Fig. 14b, we use the relation between the shape of the residuals and the orientation of the vortex as extracted from numerical simulations to post-select all collisions for which we can safely estimate the relative angle to be approximately 0, 45, and 90 degrees, within an uncertainty of the order of ~ 30 degrees. Then, in each group

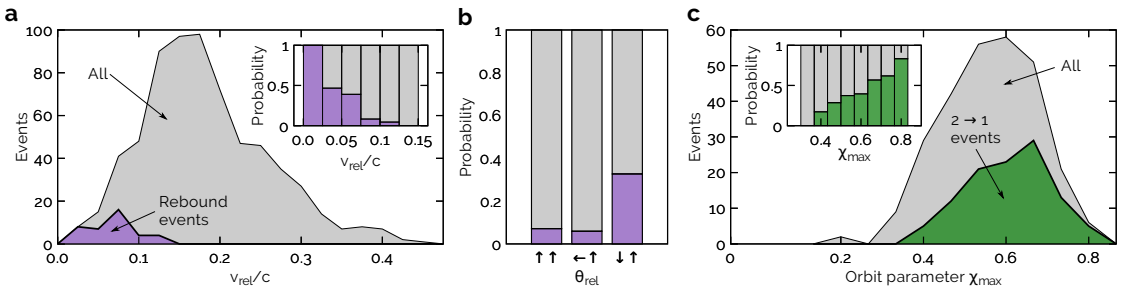

Figure 14. *Statistical analysis of experimental observations. (a) occurrence of rebound events (purple) as a function of the vortex-vortex relative velocity, within the ensemble of all collision events (grey). The velocity v_{rel} is normalized to the speed of sound c evaluated at the center of the BEC. The inset shows the relative occurrence for each bin; (b) fraction of rebound events as a function of the relative angle just before the interaction; (c) occurrence of events (green) in which one vortex line disappears after the interaction, as a function of the largest orbit parameter of the vortex pair χ_{max}, i.e., the amplitude of the outer vortex orbit in the BEC; the inset shows the relative occurrence per bin. Figure from [P6].*

we count the fraction of rebounds. The results confirm that rebounds are most likely to occur between anti-aligned vortices, consistent with the simulations.

Orbiting dynamics. Two parallel vortices can orbit around the center of the BEC in the same direction with distinct orbit parameters χ, only weakly interacting when they are at the closest distance. When imaged from a radial direction, the two vortices appear to cross periodically; in reality, they pass by each other without visible changes of the residual pattern, with, at most, only slight modifications of orbits and visibility. An example of such orbiting dynamics can be observed in the experimental image Fig. 12c, and a similar case in the numerical simulations is shown in Fig. 13e.

Reconnections. If the initial orientations of the vortices are not parallel and the axial collision dynamics is sufficiently fast, single reconnection processes are favored. As simulations show (Fig. 13c,d), these reconnection processes generate cusps which, as they relax, form Kelvin waves [215], *i.e.* helical perturbations of the cores, as for instance the ones visible at $\tau = 0.192$ in Fig. 13c. The excitation of Kelvin waves *via* vortex reconnections was observed in superfluid Helium [136] and similar effects have also been found in numerical simulations of Fermi superfluids [413]). In our experiment, such a perturbation of the vortex lines in a reconnection event implies a sudden change of both the orbit and the residual pattern, along with a significant change of visibility of one or both vortices, as illustrated in Fig. 12d,e. The nonlinear interaction among Kelvin waves might lead to Kelvin wave cascades [230, 231]. However, in the confined geometry of our elongated BEC, the role of Kelvin waves is expected to be reduced compared to a uniform superfluid, due to finite (transverse) size effects. This is consistent with the fact that, if we release the whole condensate from the trap in order to observe the vortex lines by taking absorption images in the axial direction, as done in [109, 359], we typically

observe almost rectilinear vortices with only smooth bends (mostly induced by boundary conditions for off-centered vortices), even in the presence of two or more vortices in the condensate.

Ejections. When a vortex orbits the outer part of the condensate (large χ) a fast interaction with another vortex (either *via* a reconnection or a close orbiting interaction) can cause the expulsion of either vortex towards the surface of the BEC, where the density is too low for observation (the other vortex remaining inside). Examples of such ejection processes are shown in Fig. 12e,f (reconnection-induced and orbiting-induced, respectively). The numerical counterpart of Fig. 12e is illustrated in Fig. 13d (in order to emphasize this vortex-visibility effect in the numerical simulations, the thickness and the color of the lines in the plots reported in the right column of Fig. 13 are modulated by the Thomas–Fermi density at which the corresponding vortex core resides, see Appendix B). A statistical analysis of experimental data is given in Fig. 14c: excluding cases where rebounds occur, we count all events of vortex-vortex interaction as a function of the largest orbit parameter of the vortex pair $\chi_{\max}$. Then, among them, we show in green those in which the visibility of one of the two vortex lines is lost in the interaction. The relative distribution in the inset clearly supports the idea that ejections occur at large χ, *i.e.*, near the boundary of the condensate, in agreement with the result of the numerical simulations. These ejection processes might play a key role in the early post-quench dynamics of the BEC, when most of the vorticity produced by the Kibble–Zurek mechanism is progressively lost at the boundaries, eventually leaving only a few vortex lines in the final BEC [253]. It is also worth noticing that a similar dynamics was previously discussed in Ref. [34]. In that case, pairs of dark solitons are created by an optical phase imprinting technique and their subsequent dynamics is observed. GP simulations show that solitons first decay into vortex rings and then into pairs of solitonic vortices which, in the experimental conditions, are still detected as dark soliton stripes. Hence a collision between two soliton stripes is actually a collision between two pairs of vortices. Such collisions can be inelastic and can also lead to "sling shot" events where one of the solitonic vortices is ejected from the condensate. Due to the different mechanism for the creation of vortices, the configurations discussed in Ref. [34] involve typically more than two vortices in each collision, and thus the dynamics is more complex than in our case, though qualitatively consistent.

Conclusions

In conclusion, we have developed an innovative experimental technique which, combined with numerical simulations, is capable of determining the real-time position and 3D orientation of vortex lines in an elongated BEC. This combined technique allows us to investigate vortex dynamics in a 3D quantum system with unprecedented resolution: novel types of vortex interaction regimes are unambiguously identified beyond standard reconnections already observed in superfluid helium [41]. While in uniform, unbounded and non-rotating superfluids reconnections of vortex lines moving towards each other are

unavoidable, and their effects have been extensively investigated [102, 207, 227, 290, 335, 382, 397, 426], here we show that in a confined and inhomogeneous superfluid, depending on the relative velocity and orientation, two vortex lines can also rebound, perform double reconnections, maintain their orbits with negligible interaction and undergo ejections. These processes should play even more important roles when the BEC contains more than two vortices, for example in the case of turbulence [387].

2.3. Spin superfluidity of binary mixtures of atomic Bose-Einstein condensates

2.3.1. Spin-dipole oscillation and polarizability of a binary Bose-Einstein condensate near the miscible-immiscible phase transition [P7]

Abstract: We report on the measurement of the spin-dipole (SD) polarizability and of the frequency of the SD oscillation of a two-component Bose–Einstein condensate of sodium atoms occupying the $|3^2S_{1/2}, F = 1, m_F = \pm 1\rangle$ hyperfine states. This binary spin-mixture presents the important properties of being, at the same time, fully miscible and rid of the limit set by buoyancy. It is also characterized by a huge enhancement of the SD polarizability and by the consequent softening of the frequency of the SD oscillation, due to the vicinity to the transition to the immiscible phase. The experimental data are successfully compared with the predictions of theory.

Introduction

The study of mixtures of Bose-Einstein condensates (BECs) has opened rich opportunities for novel experimental and theoretical investigations. Mixtures of ultracold atoms offer great flexibility thanks to the variety of atomic species and the additional degree of freedom related to the hyperfine structure [173, 284, 299, 324, 375, 383] (for a recent overview see [372]). For a weakly interacting mixture of two BECs, the ground state of the system can either be a miscible mixture of the two components or a phase separated configuration [88]. Nevertheless, the stability of mixtures very close to the critical region is sensitive to other effects, such as asymmetries in the trapping potential [209]. Moreover, for systems in which the intracomponent coupling constants do not exactly coincide, one of the two components will experience a positive buoyancy and will "float" on the other. Previous experiments involving two internal states of rubidium were affected by both of these problems [122, 167, 169, 295, 408] hence setting strong limits to explore the many-body properties of miscible binary BECs. In particular, such conditions prevent the study of the static and dynamic response of an unpolarized system close to the transition between the miscible and immiscible phases, where interaction effects are particularly important despite the weakly interacting nature of the gas [195].

Here we report on the first measurement of the spin-dipole (SD) polarizability of a two-component BEC, as well as the frequency of the SD oscillation, by using an ultracold mixture of the $|3^2S_{1/2}, F = 1, m_F = +1\rangle \equiv |\uparrow\rangle$ and $|3^2S_{1/2}, F = 1, m_F = -1\rangle \equiv |\downarrow\rangle$ states of atomic sodium. The polarizability characterizes in a fundamental way the

thermodynamic behavior of binary ultracold gases and exhibits a divergent behavior at the transition between the miscible and immiscible phases, with the occurrence of important spin fluctuations [1, 46, 329]. On the other hand, the SD oscillation is the simplest collective excitation supported by the system in the presence of harmonic trapping and is characterized by the motion of the two components with opposite phase around equilibrium. The SD oscillation is the analog of the famous giant dipole resonance of nuclear physics, where neutrons and protons oscillate with opposite phase [52]. Actually, collective modes are a popular subject of research in quantum many body systems (see, *e.g.*, [317]) where experiments are able to determine the corresponding frequencies with high precision, providing a good testbed for detailed comparison with theory and an accurate determination of the relevant interaction parameters. Collective dynamics has been already investigated in quantum binary mixtures of atomic gases like repulsive gases of Fermi atoms [104, 329, 392, 396], Bose-Bose [114, 167, 195, 258, 267, 272, 274, 296, 347, 348, 365, 423] and Bose-Fermi mixtures [129] as well as Bose-Fermi superfluid mixtures [130, 340]. In the case of Bose-Bose mixtures both the polarization and the SD oscillation frequency are predicted to be crucially sensitive to the difference between the value of the intra and intercomponent interactions [195, 347] which is particularly small in our case. The dramatic change of the density profile of the trapped gas, caused by a small displacement of the minima of the trapping potentials of the two species near the miscible-immiscible phase transition, was first investigated theoretically in [195]. Our mixture is not subject to buoyancy as $g_{\uparrow\uparrow} = g_{\downarrow\downarrow} \equiv g$ and is on the miscible side $g_{\uparrow\downarrow} < g$ near the boundary of the phase transition (g and $g_{\uparrow\downarrow}$ are respectively the intra and intercomponent coupling constants). The fact that $(g - g_{\uparrow\downarrow})/g \simeq 7\,\%$, as given by the scattering lengths $a_{\uparrow\uparrow} = a_{\downarrow\downarrow} = 54.54(20)a_0$ and $a_{\uparrow\downarrow} = 50.78(40)a_0$, where a_0 is the Bohr radius [219], ensures the stability of the mixture and, together with the absence of buoyancy, allows us to overcome the ultimate limits to measure both the polarizability and SD oscillation frequency.

Mixture preparation

Our experiment is based on the apparatus introduced in [240] and starts with a nearly pure BEC of ^{23}Na atoms in the $|\downarrow\rangle$ state in a crossed optical dipole trap with frequencies $[\omega_x, \omega_y, \omega_z]/2\pi = [47.7(2), 207.2(3), 156.8(2)]$ Hz. The magnetic fields along the three spatial directions are calibrated with a precision of 1 mG using RF spectroscopy techniques. The first step towards the creation of the spin mixture is to perform a Landau–Zener transition to the $|F = 1, m_F = 0\rangle \equiv |0\rangle$ state with nearly 100 % transfer efficiency. This is realized at a magnetic field of 100 G to isolate a two-level system exploiting the quadratic Zeeman shifts. The second step consists in inducing a Rabi oscillation among the three Zeeman sublevels to obtain a 50/50 spin mixture of $|\downarrow\rangle$ and $|\uparrow\rangle$ [425]. The bias field along $\hat{x}$ is taken small enough to allow us to neglect the quadratic Zeeman shifts compared to the Rabi frequency and is kept on during the whole experimental sequence following the Rabi pulse. The number of atoms in each spin component is $N_\uparrow = N_\downarrow \simeq 10^6$ and the total chemical potential of the cloud is $\mu_{\rm tot}/k_{\rm B} \simeq 200\,$nK. Fig. 15(a) shows typical

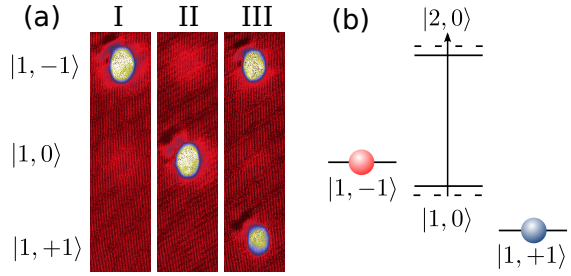

Figure 15. *(a) Absorption images taken after a SG expansion for I) the dipole loading, II) the Landau–Zener transition, III) the Rabi pulse leading to the creation of the binary mixture. (b) Stabilization of the two components by shifting the $|0\rangle$ state using microwave dressing on the transition to $|F = 2, m_F = 0\rangle$. Figure from [P7].*

absorption images of the spinor BEC after a 10 ms Stern–Gerlach (SG) expansion in a magnetic field gradient along $\hat{z}$. In order to prevent the decay of the mixture to $|0\rangle$ by spin changing collisions, we lift this level by ~ 10 kHz using blue detuned microwave dressing on the transition to $|F = 2, m_F = 0\rangle$ (see Fig. 15(b)).

Spin-dipole polarizability

The SD polarizability of a spin mixture describes the ability of the system to adapt itself to a displacement in opposite direction of the trapping potentials of the two components. After realizing a fully overlapped configuration, we adiabatically apply a magnetic field gradient B'_x along $\hat{x}$ using a pair of coils in anti-Helmholtz configuration. The gradient is controlled with a resolution at the level of 4 mG/cm. This displaces the minima of the trapping potentials such that $V_{\uparrow,\downarrow} = m\omega_x^2(x \pm x_0)^2/2$ where $x_0 = g_F\mu_B B'_x/(m\omega_x^2)$ (g_F is the Landé factor, μ_B the Bohr magneton and m the atomic mass). The SD polarizability is defined as

$$\mathcal{P}(x_0) \equiv \frac{d(x_0)}{2x_0}, \tag{11}$$

where $d = x_\downarrow - x_\uparrow$ is the *in-situ* relative displacement between the centers of mass of each component (see Fig. 16(a)). After a 2 ms SG expansion, we measure d by fitting each spin component density distribution to independent Thomas–Fermi (TF) profiles to extract their centers $x_{\uparrow,\downarrow}$. The individual density profiles are not exactly TF-like, but we verified, using a Gross–Pitaevskii equation (GPE) simulation, that this approximate fitting procedure results in an overestimation of $\mathcal{P}$ by at most 6%. Later in the text we discuss the additional correction to the measurement of $\mathcal{P}$ related to interactions during the SG expansion. Fig. 16(a) shows the experimental results where the value of x_0 is estimated after calibrating B'_x. We observe that all data points strongly deviate from the prediction $d = 2x_0$ for a mixture without intercomponent interactions (green solid line), revealing the large SD polarizability of the system.

We use a second experimental protocol to determine the polarizability which will later prove to be useful for measuring the SD oscillation frequency. It consists in realizing the

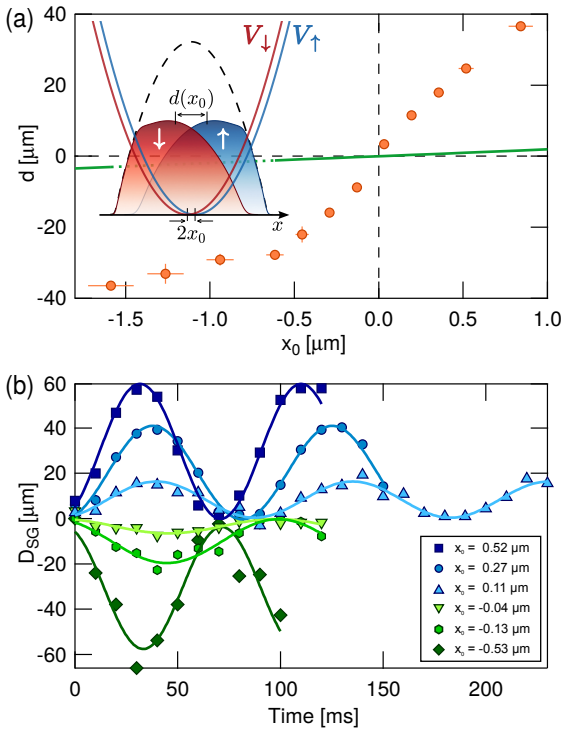

Figure 16. *(a) Relative displacement $d = x_\downarrow - x_\uparrow$ between the spin components as a function of x_0 (orange dots). The green solid line corresponds to the situation of no intercomponent interaction $d = 2x_0$. The figure also shows a sketch of the experimental conditions (the dashed curve is the total cloud density). (b) SD oscillations for different values of x_0 (positive and negative) observed using the second experimental protocol. The solid lines are fit to the data according to Eq. (12). In each figure of the paper, data error bars are the sum in quadrature of systematic and statistical errors (one standard deviation of the mean). Figure from [P7].*

Rabi pulse $|0\rangle \rightarrow |\uparrow,\downarrow\rangle$ in the presence of a magnetic field gradient. As the minima of the trapping potentials for the $|\uparrow\rangle$ and $|\downarrow\rangle$ states are shifted by $\mp x_0$ with respect to the initial state $|0\rangle$, this makes the two components oscillate out of phase after the Rabi pulse. The *in-situ* time evolution of the relative displacement $D(t) = x_\downarrow(t) - x_\uparrow(t)$ is expected to be given by $D(x_0, t) = d(x_0)\,[1 - \cos[\omega(x_0)t]]$. Measurements of such oscillations after a SG expansion of $t_{\mathrm{SG}} = 10\,\mathrm{ms}$ for different values of x_0 varying the magnetic field gradient are reported in Fig. 16(b). After the SG expansion, the displacement between the spin components is given by $D_{\mathrm{SG}}(x_0, t, t_{\mathrm{SG}}) = D(x_0, t) + \partial_t D(x_0, t)\, t_{\mathrm{SG}}$ such that we analyze the data by fitting it with the following function:

$$D_{\mathrm{SG}} = A(x_0, t_{\mathrm{SG}}) \cos[\omega(x_0)t + \phi(x_0, t_{\mathrm{SG}})] + d(x_0), \tag{12}$$

where $A(x_0, t_{SG}) = -d(x_0)\sqrt{1 + \omega^2(x_0)t_{\mathrm{SG}}^2}$ and $\phi(x_0, t_{\mathrm{SG}}) = \arctan[\omega(x_0)t_{\mathrm{SG}}]$. Eq. (12) allows us to extract the value of $d(x_0)$ neglecting here again intercomponent interactions during the expansion.

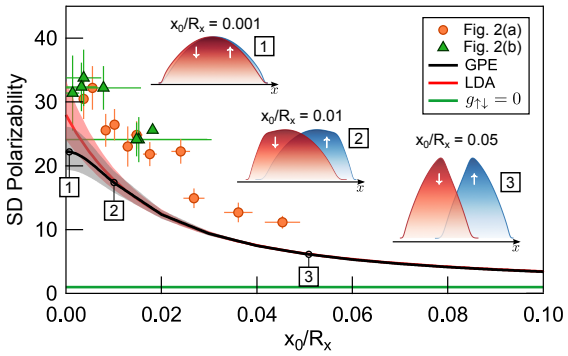

Figure 17. *SD polarizability extracted from the data of Fig. 16(a) (orange dots) and (b) (green triangles). The black (red) solid line is the prediction computed using the GPE (LDA). The shaded regions give the uncertainties taking into account error bars on the value of the coupling constants [219]. The green solid line corresponds to the situation of no intercomponent interaction* $\mathcal{P} = 1$*. We also provide the density profiles* $n_{\uparrow,\downarrow}(x, 0, 0)$ *from the GPE for* $x_0/R_x = 0.001, 0.01, 0.05$*. The experimental points overestimate the actual value of* $\mathcal{P}$ *due to the approximation of the TF fit and the interaction effect during the expansion (see text). Figure from [P7].*

Fig. 17 shows the SD polarizability as a function of x_0/R_x (R_x is the TF radius along $\hat{x}$) using the data of Fig. 16. We notice a strong nonlinear dependence of the polarizability on the separation between the two trapping potential minima, which is maximal in the linear limit ($x_0 \to 0$) and tends to 1 for large separation ($x_0 \gg R_x$). In the same figure, we also plot the theoretical predictions obtained within the local density approximation (LDA) and the numerical integration of the GPE performed with the experimental parameters. We identify three regions along $\hat{x}$, with the outer two regions occupied by either the $|\uparrow\rangle$ or $|\downarrow\rangle$ component and the inner region occupied by both of them. In the linear limit ($x_0 \to 0$) the LDA gives the result

$$\mathcal{P}(x_0 \to 0) = \frac{g + g_{\uparrow\downarrow}}{g - g_{\uparrow\downarrow}}, \tag{13}$$

for the polarizability [347][11], pointing out its divergent behavior near the phase transition occurring at $g_{\uparrow\downarrow} = g$. The agreement between the LDA and the GPE is excellent except in the region of small minima separation where the LDA becomes less and less adequate because of the large value of the spin healing length $\hbar/\sqrt{2mn(g - g_{\uparrow\downarrow})}$ (n is the total density of the cloud). In general, we observe a good agreement between the theoretical predictions and the experimental data. In particular, the huge effect on the polarizability caused by the vicinity to the miscible-immiscible phase transition is clearly revealed and the scaling with x_0/R_x is well reproduced. The data analysis presented so far has however been performed neglecting interactions between the spin components during the SG expansion. Indeed, GPE simulations of the expansion in the presence of interactions

[11] The SD polarizability Eq. (13) should not be confused with the magnetic polarizability $\chi_M = 1/[n(g - g_{\uparrow\downarrow})]$ which is defined in uniform matter in terms of the energy cost $\delta E = M^2/(2\chi_M)$ associated with a small polarization $M = (N_\uparrow - N_\downarrow)/(N_\uparrow + N_\downarrow)$ of the gas.

show that the experimentally measured polarizability is overestimated by 5% (30%) for the 2 ms (10 ms) SG expansion. This explains the remaining difference between the experimental points of Fig. 17 and the theoretical predictions.

Spin-dipole oscillation

A useful estimate of the SD frequency is obtained by employing a sum rule approach [317] based on the ratio $\hbar^2\omega_{\rm SD}^2 = M_1/M_{-1}$, where $M_1 = N\hbar^2/2m$ ($N = N_\uparrow + N_\downarrow$) is the model independent energy weighted sum rule relative to the SD operator $\sum_i(x_{i\downarrow} - x_{i\uparrow})$, and $M_{-1} = N\mathcal{P}(x_0 \to 0)/(2m\omega_x^2)$ is the inverse energy weighted sum rule fixed according to linear response theory by the linear SD polarizability [347]. This leads to the following relation between the SD frequency and polarizability

$$\omega_{\rm SD} = \frac{\omega_x}{\sqrt{\mathcal{P}(x_0 \to 0)}}\,. \tag{14}$$

Using the LDA expression (13) for the polarizability one derives the following prediction for the SD frequency

$$\omega_{\rm SD} = \sqrt{\frac{g - g_{\uparrow\downarrow}}{g + g_{\uparrow\downarrow}}}\,\omega_x\,. \tag{15}$$

The same result can be directly obtained by generalizing the hydrodynamic theory developed in [376] for density oscillations to the case of SD oscillations [317]. Eq. (15) explicitly points out the crucial role played by the intercomponent coupling constant $g_{\uparrow\downarrow}$ in softening the frequency of the SD mode with respect to the value ω_x characterizing the frequency of the in-phase center-of-mass oscillation. We check, using time-dependent GPE simulations of the SD oscillations for our experimental parameters, that the sum rule prediction (4) provides ω_{SD} with an accuracy better than 1% when substituting the value of the static SD polarizability $\mathcal{P}(x_0 \to 0)$ from the GPE. This demonstrates that an accurate SD frequency measurement can be used to determine the value of the SD polarizability.

As shown on Fig. 16(b), the Rabi pulse in the presence of a magnetic field gradient gives rise to the excitation of SD oscillations whose frequency can be extracted as a function of the induced displacement x_0. A first estimate of the SD frequency is obtained considering that $\omega_{\rm SD} = \omega(x_0 \to 0)$. Indeed, for large values of x_0, the oscillation frequency $\omega(x_0)$ approaches ω_x while it decreases to $\omega_{\rm SD}$ as $x_0 \to 0$. Since in the small x_0 limit the amplitude of the oscillation tends to zero, we perform a linear fit to the curve of $\omega(x_0)/\omega_x$ as a function of the oscillation amplitude $A(x_0)$ and extract $\omega_{\rm SD}/\omega_x = 0.18(1)$ from the y-intercept of the linear fit (see Fig. 18(a)). This method shows a good agreement with the LDA prediction Eq. (15) $\omega_{\rm SD}/\omega_x = 0.189(15)$ and with the GPE simulations yielding $\omega_{\rm SD}/\omega_x = 0.213(17)$ (uncertainties take into account error bars on the value of the coupling constants [219]). The different values of $\omega_{\rm SD}$ from the LDA and GPE calculations have the same origin as the one discussed in the case of the polarizability and are due to the large value of the spin healing length in the vicinity of the quantum phase transition.

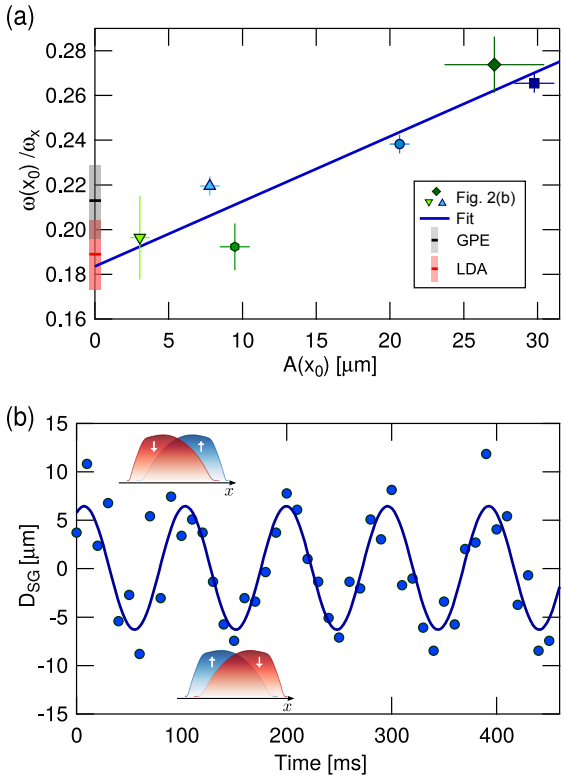

Figure 18. *(a) Ratio $\omega(x_0)/\omega_x$ as a function of the amplitude $A(x_0)$ for the data of Fig. 16(b) (same marker styles). The black (red) marker is the prediction of the GPE $\omega_{SD}/\omega_x = 0.213(17)$ (LDA $\omega_{SD}/\omega_x = 0.189(15)$). Extrapolating the linear fit of $\omega(x_0)/\omega_x$ (solid blue line) for vanishing amplitude gives $\omega_{SD}/\omega_x = 0.18(1)$. (b) SD oscillations using the alternative method (blue dots) giving $\omega_{SD}/\omega_x = 0.218(2)$. We also show two density profiles $n_{\uparrow,\downarrow}(x, 0, 0)$ illustrating the out-of-phase SD oscillations (data obtained from the GPE taking the equilibrium state for $x_0/R_x = 0.01$ as initial condition before setting $x_0 = 0$ to start the oscillations). Figure from [P7].*

An alternative and more efficient way to excite the SD mode and to measure its frequency consists in first creating two perfectly overlapped spin states where $B'_x = 0$ ($x_0 = 0$) and then applying a magnetic field gradient $B'_x = 0.1\,\mathrm{G/cm}$ ($x_0 = 1.3\,\mu\mathrm{m}$) for $3\,\mathrm{ms} \ll 2\pi/\omega(x_0)$ before restoring $B'_x = 0$. This leads to an *in-situ* dipole oscillation shown in Fig. 18(b) after 10 ms of SG expansion. We measure $\omega_{\mathrm{SD}}/\omega_x = 0.218(2)$ which is slightly larger than the previous estimate based on the data of Fig. 16(b) and shows better agreement with the prediction from the GPE simulations. For a precise determination of ω_{SD}, it is important to ensure that the SD mode has a small *in-situ* amplitude: here we estimate $D_{\mathrm{SD}} = D_{\mathrm{SG}}/\sqrt{1+\omega_{\mathrm{SD}}^2 t_{\mathrm{SG}}^2} = 5.4\,\mu\mathrm{m}$ which is relatively small compared to the TF radius $R_x = 40\,\mu\mathrm{m}$. In all experiments, we observe oscillations without noticeable damping on very long timescales (they are ultimately limited by the cloud lifetime). Indeed, the maximal relative velocities of the two superfluid components $v_{\mathrm{max}} = 1.2\,\mathrm{mm/s}$ for the data of Fig. 2(b), and $v_{\mathrm{max}} = 0.4\,\mathrm{mm/s}$ for the data of Fig.

4(b) are smaller than the critical velocity for the dynamical counterflow instability $v_{\rm cr} = \sqrt{\mu_{\rm tot}(1 - g_{\uparrow\downarrow}/g)/2m} = 1.8\,{\rm mm/s}$ [2].

Conclusion

In conclusion, we reported on the experimental measurements of the polarizability and of the frequency of the SD oscillation in a two-component BEC of sodium. Because of the vicinity to the miscible-immiscible quantum phase transition both quantities are very sensitive to the value of the intercomponent interaction and their behavior deviates by large factors from the values predicted in the absence of intercomponent interaction. This represents a major difference with respect to other available superfluid quantum mixtures, like the Bose-Fermi mixtures of lithium gases [103, 130], where the role played by the intercomponent interaction is much less crucial. Similarly to the case of [103, 130] our mixture is characterized by two interacting superfluids oscillating with opposite phase and the observed SD oscillation is undamped for small amplitude as a consequence of superfluidity. For large amplitude motion the Landau's critical velocity will, however, behave very differently, being very sensitive to the value of the intercomponent interaction [2]. Another interesting feature concerns the behavior of the SD oscillation at finite temperature. While the damping of the SD oscillation was actually observed in the old experiments of [104] carried out on a normal Fermi gas, understanding the behavior of the collective modes in the presence of both a condensed (superfluid) and thermal (non-superfluid) components remains extremely challenging [17, 248]. Other topics of interest concern the experimental realization of magnetic solitons [327] and the inclusion of coherent coupling between the two spin components. The Bose mixtures realized and investigated here then represent an ideal platform to explore important equilibrium and dynamic properties of binary superfluids.

2.3.2. Observation of spin superfluidity in a Bose gas mixture [P5]

Abstract: The spin dynamics of a harmonically trapped Bose–Einstein condensed binary mixture of sodium atoms is experimentally investigated at finite temperature. In the collisional regime the motion of the thermal component is shown to be damped because of spin drag, while the two condensates exhibit a counterflow oscillation without friction, thereby providing direct evidence for spin superfluidity. Results are also reported in the collisionless regime where the spin components of both the condensate and thermal part oscillate without damping, their relative motion being driven by a mean-field effect. We also measure the static polarizability of the condensed and thermal parts and we find a large increase of the condensate polarizability with respect to the $T = 0$ value, in agreement with the predictions of theory.

Introduction

In the last years, spin-superfluidity and spin-transport phenomena have attracted a

great interest in the community of condensed matter physics from both the experimental and theoretical point of view [371]. Even in systems where spin is conserved, the behavior of spin transport is highly nontrivial since, at finite temperature, collisions between different spin species yield relaxation of the spin current, a phenomenon known as spin drag. So far the study of superfluidity at finite temperature has mainly concerned the density channel, where both the number of particles and total current are conserved. A major consequence is that, in the collisional regime, sound can propagate both in the superfluid phase, where it takes the form of first and second sound, as well as in the normal phase (ordinary sound). In the presence of collisions, spin sound can instead propagate only in the superfluid phase, so that its observation, in this case, can be considered as an ultimate proof of spin superfluidity. In fact, the propagation of spin sound in the collisionless regime is consistent with superfluidity, but can be predicted also in the normal phase as a consequence of mean-field interactions (see, for instance, the propagation of sound in a normal Fermi liquid [316]). Actually the equations of hydrodynamics applied to a superfluid quantum mixture predict the propagation of three sounds [13, 402]: pressure, temperature and spin sound (see [17] for a recent application of three-velocity hydrodynamic theory to Bose–Bose mixtures).

The dynamic behavior of multicomponent quantum gases has been extensively investigated in the last years (see, for example, [372] for a review on spinor Bose gases). Experiments on spin dynamics have been carried out in gases occupying two different hyperfine states, [42, 104, 167, 169, 258, 286, 296, 363, 392], in larger spinor systems [172, 213, 305, 353, 375, 425], as well as in mixtures of different isotopes or atomic species [129, 130, 272, 273]. Theoretical activity in these systems has also become very popular (see, for example, [2, 16, 17, 70, 195, 248, 282, 329, 334, 348, 396, 418, 422]). Spin-drag phenomena have been experimentally investigated in the unitary Fermi gas [26, 199, 370], in Bose gases [225], in Bose–Fermi mixtures [103], as well as in two-dimensional Fermi gases [228, 254]. The role of spin polarization on the stability of supercurrents [33] and the counterflow instability in Bose–Fermi [130] and in Bose–Bose [174, 213] mixtures have also been experimentally investigated.

In this section, we experimentally study the spin-dipole oscillation and the role of collisions at finite temperature. The main result of our work is the observation of undamped spin oscillations in the collisional regime. This observation actually provides direct evidence of spin superfluidity.

We consider a symmetric BEC mixture of the $|m_F = +1\rangle \equiv |\uparrow\rangle$ and $|m_F = -1\rangle \equiv |\downarrow\rangle$ components of the $F = 1$ hyperfine ground state of sodium atoms, confined in a harmonic trap. Differently from most of the quantum mixtures so far investigated in the literature, our sodium mixture is characterized by an almost perfect symmetry between the two components, both in terms of the number of atoms occupying the two hyperfine states, the confining potential and the intraspecies interaction. Furthermore the mixture is fully-miscible, not subject to buoyancy and is close to the miscible-immiscible phase transition since $(a - a_{\uparrow\downarrow})/a = 0.07 \ll 1$, with $a \equiv a_{\uparrow\uparrow} = a_{\downarrow\downarrow} = 54.54(20)a_0$ and $a_{\uparrow\downarrow} = 50.78(40)a_0$ [219], a_0 being the Bohr radius. This mixture, then, represents an ideal system to investigate the effects of spin superfluidity. The zero temperature behavior of the spin-

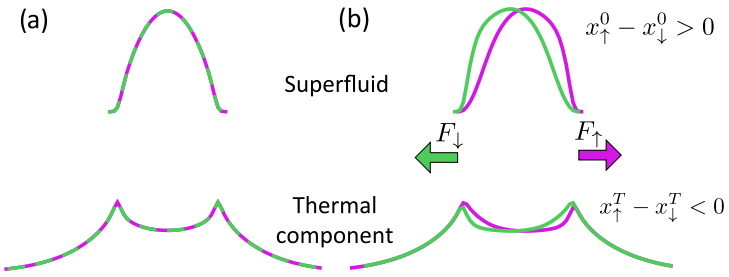

Figure 19. *Computed atomic density distribution $n_{\uparrow,\downarrow}(x,0,0)$ of the binary mixture at finite temperature showing the component $\uparrow$ (violet) and $\downarrow$ (green), each one of these being composed of a superfluid (top) and a thermal part (bottom). (a) In the absence of any external force the centers of mass of all four components overlap. (b) In the presence of a differential force $F_{\uparrow,\downarrow}$, the condensed part shows a large positive polarization, while the thermal component interacting with the condensate is polarized in the opposite direction. The thermal part lying outside the BEC region has a small positive polarization. Figure from [P5].*

dipole oscillation was investigated in [P7]. Here, we report results at finite temperature, both in the collisional and in the collisionless regimes, which are experimentally realized by varying the frequencies of the trapping potential. We prove that in both regimes the mixture is able to support undamped spin oscillations. Furthermore, the vicinity to the miscible-immiscible phase transition is associated with a strong coupling between the two spin clouds. In addition to the softening of the spin-dipole oscillation frequency and the sizable increase of the static spin polarizability, that were already observed at zero temperature [P7], the vicinity to the phase transition causes a further important amplification of the spin polarization of the superfluid component due to the interaction with the thermal part.

We start with an equally populated mixture of the $\uparrow,\downarrow$ states [P7] with $N_\uparrow = N_\downarrow \simeq 4\times 10^5$ (with a spin imbalance fluctuation smaller than 10%) and consider two different trap geometries: (A) a crossed optical trap with frequencies $[\omega_x,\omega_y,\omega_z]/2\pi = [87,330,250]$ Hz and (B) a single-beam optical trap with frequencies $[\omega_x,\omega_y,\omega_z]/2\pi = [12,1350,1350]$ Hz. Using parametric heating, we can adjust the condensed fraction of the mixture, i.e., the ratio between the total number of atoms in the condensates N_0 and the total number of atoms $N = N_\uparrow + N_\downarrow$. A major difference between the two configurations is that, in the long axial direction, configuration (A) is basically characterized by a collisionless regime ($\omega_x\tau_{\uparrow\downarrow} \gg 1$), while configuration (B) by a more collisional one ($\omega_x\tau_{\uparrow\downarrow} \sim 1$). The difference is not due to significant changes in the density, but rather in the value of ω_x. The collisional time between the $\uparrow,\downarrow$ components can be estimated employing the classical expression for $\tau_{\uparrow\downarrow}$, with the density calculated in the center of the trap at $T = T_c$. We estimate $\omega_x\tau_{\uparrow\downarrow}$ of a few tens in configuration (A) and of order unity in configuration (B).

Spin dynamics

The spin oscillation is excited by applying a magnetic field gradient B'_x for a few ms.

This generates a small force $F_{\uparrow,\downarrow} = \pm g_F \mu_B B'_x$ (g_F is the Landé factor, μ_B the Bohr magneton) that tends to separate the two components, as illustrated in Fig. 19. Such a procedure leaves the total center of mass at rest and gives rise to time-varying spin displacements

$$S_0 \equiv x^0_\uparrow - x^0_\downarrow, \qquad S_T \equiv x^T_\uparrow - x^T_\downarrow,$$

of both the condensed S_0 and the thermal part S_T, where $x^0_{\uparrow,\downarrow}$ and $x^T_{\uparrow,\downarrow}$ are the centers of the atomic distribution of the condensed and thermal components of the $\uparrow,\downarrow$ density distributions. In the experiment, we are able to study the dynamics of such four-fluid system by monitoring each of the four components to reconstruct S_0 and S_T as a function of time. The amplitude of oscillation of $\{S_0, S_T\}$ is smaller than the Thomas–Fermi radius R_x of the cloud [for a fully Bose–Einstein condensed mixture at $T = 0$, $R_x = 25\,\mu$m for configuration (A) and $R_x = 230\,\mu$m for (B)]. The two spin states are separately imaged after a Stern–Gerlach expansion in a magnetic field gradient along z, which allows us to extract the centers of mass of the four components of the fluid $\left\{x^0_\uparrow, x^0_\downarrow, x^T_\uparrow, x^T_\downarrow\right\}$.

The spin dynamics of the condensate is shown in Fig. 20a and 20b at relatively high values of T/T_c, corresponding to $N_0/N \sim 0.3$ and $N_0/N \sim 0.4$, respectively. The figure shows that the condensate, in the presence of a large thermal component, exhibits spin oscillations without visible damping in both collisionless (A) and collisional (B) regimes. The absence of friction near the BEC border, where the Landau critical velocity is vanishingly small, is due to the fact that the spin velocity, during the spin-dipole oscillation, is strongly suppressed near the surface of the condensate (see Fig.19b), differently from what happens in the rigid motion of the center-of-mass oscillation, and in agreement with the Steinwedel–Jensen model for the isospin oscillations of nuclear physics [52]. The measured frequencies ($\omega_{\rm SD} = 0.205(2)\,\omega_x$ in (A) and $\omega_{\rm SD} = 0.233(5)\,\omega_x$ in (B)) differ by about 6% from the value reported in Ref. [P7] at very low temperatures ($\omega_{\rm SD} = 0.218(2)\,\omega_x$) and by 7% (A) and 20% (B) from the value $\omega^0_{\rm SD} = \sqrt{(a - a_{\uparrow\downarrow})/(a + a_{\uparrow\downarrow})}\,\omega_x = 0.19(2)\,\omega_x$ [347], predicted by hydrodynamic theory of superfluids at $T = 0$ [12].

The thermal component, instead, behaves very differently in the two regimes. In the collisionless regime (A), after a transient of damped oscillations, it oscillates at the same spin-dipole frequency of the condensate, but with opposite phase and a smaller amplitude (see Fig. 20a), the ratio between the thermal and the condensed amplitudes being 0.18(2). In the collisional regime (B), the thermal part is instead strongly damped and quickly reaches an equilibrium position, where both spin thermal components are at rest in the center of the trap (see Fig. 20b) [13].

[12] The hydrodynamic result $\omega^0_{\rm SD}$ for the collective frequency is independent of the number of atoms and of the density of the condensate. It holds in the limit of small amplitude oscillations and in the Thomas–Fermi approximation which, in the case of spin oscillations, requires the condition that the spin healing length $\xi_s = 1/\sqrt{8\pi n(a - a_{\uparrow\downarrow})}$ be much smaller than the Thomas–Fermi radius [347]. The softening of the frequency for values of the scattering lengths close to the demixing transition is consistent with the softening of the spin sound velocity in uniform matter given, at $T = 0$, by the expression $c_s = \sqrt{\frac{n}{2m}\frac{4\pi\hbar^2}{m}(a - a_{\uparrow\downarrow})}$.

[13] Actually, we observe a small residual oscillations of the thermal part in opposite phase with respect

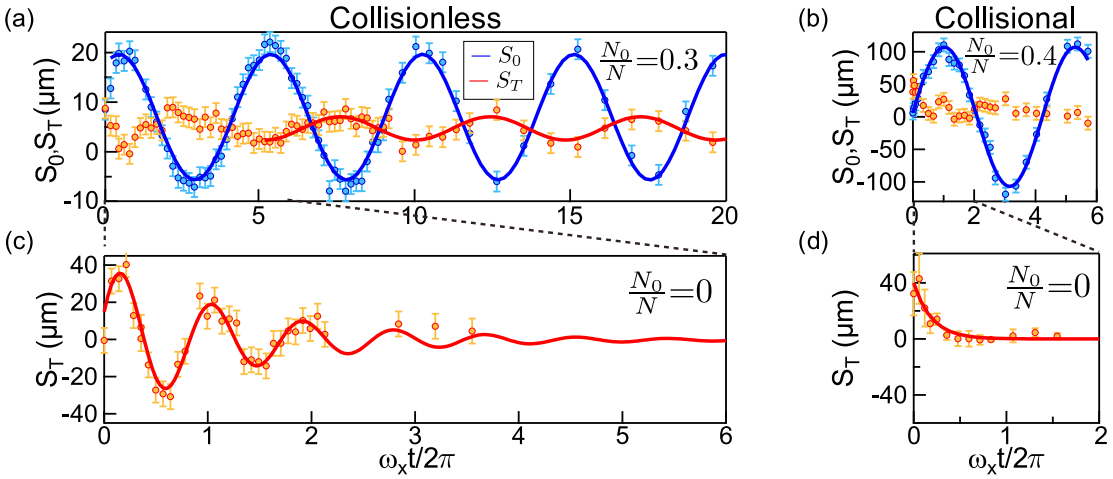

Figure 20. *(a) Spin oscillations for the thermal S_T (red) and condensed S_0 (blue) parts of the mixture with $N_0/N = 0.3$ ($T/T_c \simeq 0.85$) for configuration (A). After a small transient period, S_T oscillates at $\omega_T = 0.207(2)\,\omega_x$ which turns out to be equal, within errorbars, to the oscillation frequency of S_0, $\omega_{SD} = 0.205(2)\,\omega_x$. The ratio of the oscillation amplitude of S_T and S_0 is 0.18(2). (b) Spin oscillations for the condensed and the thermal $\{S_0, S_T\}$ parts for a mixture with $N_0/N = 0.4$ ($T/T_c \simeq 0.75$) in configuration (B). The condensed component oscillates at $\omega_{SD} = 0.233(5)\,\omega_x$, while the thermal relative motion is quickly damped. We measure an exponential decay of S_T corresponding to $\omega_x\tau = 1.5(6)$. (c) Thermal spin current S_T for a non-superfluid mixture (above T_c) in configuration (A) where we observe a few damped oscillations at the trap frequency ω_x with an exponentially decaying envelope from which we extract the decay lifetime, and obtain $\omega_x\tau = 11(2)$. (d) Same measurement for configuration (B) where we observe a purely exponential decay and extract $\omega_x\tau = 1.2(4)$, compatible with the measurement of τ below T_c. To maintain a roughly constant condensed fraction during the measurement, we limit the observation time to the first 500 ms after excitation. This explains why, due to the different trapping frequency ω_x, more oscillations are shown for configuration (A) than for (B). Figure from [P5].*

In Fig. 20, we report the results for spin dynamics above T_c, as well. In configuration (A) the cloud exhibits several oscillations before relaxing, thus revealing that collisions are not very strong (Fig. 20c). *Viceversa*, in the collisional regime (B), the behavior is diffusive, suggesting an overdamped spin oscillation (Fig. 20d). A similar spin-drag effect was observed in the Bose-Fermi mixture of [103], as well as in a Bose gas above T_c in [225]. From our experimental data, we extract $\omega_x\tau = 11(2)$ for (A) and $\omega_x\tau = 1.2(4)$ for (B). These measurements are in agreement with the theoretical estimates of $\omega_x\tau_{\uparrow\downarrow}$ given earlier in the Letter.

Finally, it is worth pointing out that the behavior of the spin-dipole oscillations is very different with respect to the center-of-mass motion, where both the condensed and thermal parts oscillate in phase without damping at the frequency $\omega_x/2\pi$, independent

to the condensed component (the ratio of the oscillation amplitudes of S_T and S_0 is smaller than 0.04(1)) which is expected to disappear in the deep collisional regime $\omega_x\tau_{\uparrow\downarrow} \ll 1$.

of the presence of collisions.

Spin-dipole polarizability

The counter-phase oscillation of the thermal component observed in the collisionless regime (see Fig. 20a) can be physically understood by investigating the behavior of the spin-dipole polarizability of the gas at finite temperature, employing the mean field Hartree–Fock theory [317] in the presence of a static spin-dipole constraint of the form $-m\omega_x^2 x_0 x\sigma_z$ (σ_z is the third Pauli matrix). This additional potential generates a force acting on the two spin components in opposite directions ($F_{\uparrow,\downarrow} = \pm m\omega_x^2 x_0$), x_0 being the displacement of the trap minimum for each component. By neglecting interaction effects induced by the thermal component on the condensate, as well as thermal-thermal interactions, and using the Thomas–Fermi approximation for the condensate, one obtains the following result for the spin density $s_z^0 = n_\uparrow^0 - n_\downarrow^0$ of the condensate [347]:

$$s_z^0 = -x_0 \frac{a + a_{\uparrow\downarrow}}{a - a_{\uparrow\downarrow}} \frac{\partial n^0}{\partial x} \,. \tag{16}$$

For the spin density $s_z^T = n_\uparrow^T - n_\downarrow^T$ of the thermal component one instead finds the results

$$s_z^T = -x_0 \frac{a + a_{\uparrow\downarrow}}{a - a_{\uparrow\downarrow}} \frac{\partial n^T}{\partial x} \tag{17}$$

inside the spatial region occupied by the condensate, where the thermal part feels interaction effects, and

$$s_z^T = -x_0 \frac{\partial n^T}{\partial x} \tag{18}$$

outside. In the above equations, n^0 and n^T are the equilibrium condensate and thermal total densities, respectively. The corresponding contribution to the spin-dipole polarizability is then obtained by integrating the quantities $x s_z^0$ and $x s_z^T$. These results show that the spin polarization of the inner thermal atoms is amplified by the same large factor $(a + a_{\uparrow\downarrow})/(a - a_{\uparrow\downarrow})$ as for the condensate. The corresponding polarization effects have however opposite signs, the density derivative of the condensate, at equilibrium, being opposite to the one of the inside thermal component (see Fig. 19).

For higher temperatures, interaction effects of the thermal component on the condensate can no longer be neglected. The behavior of the spin polarization can be explored more accurately, by solving in a consistent way the coupled Hartree–Fock equations for the condensate and for the thermal part. Figure 21 shows the resulting predictions for the condensate and thermal contributions to the spin polarizability, which are respectively defined as $\mathcal{P}_0 = (\int x s_z^0 d\mathbf{r})/N_0$ and $\mathcal{P}_T = (\int x s_z^T d\mathbf{r})/N_T$. The figure reveals the occurrence of a large enhancement of $\mathcal{P}_0$ with respect to the $T = 0$ case, which is caused by the interaction with the inside thermal component and is strongly enhanced by the smallness of $(a - a_{\uparrow\downarrow})$. The resulting values for the temperature dependence of the polarization of the condensate, as well as of the total polarization, $\mathcal{P}_{\rm tot} = (N_0\mathcal{P}_0 + N_T\mathcal{P}_T)/N$, turn out

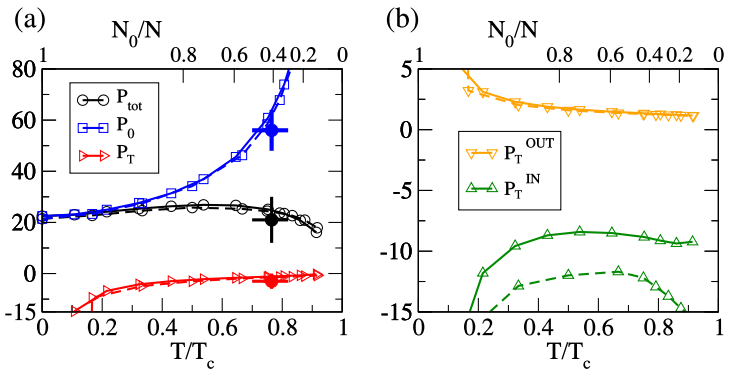

Figure 21. *(a) Static spin-dipole polarizability as a function of temperature showing, respectively, the different contributions from the superfluid (blue), the thermal component (red) and the total one (black). (b) The thermal part lying in the region occupied by the superfluid has a negative polarization (green) whereas the outer part has a small positive polarization. The calculation has been performed for the two different configurations (A) (solid) and (B) (dashed). The static polarizabilities measured for $N_0/N = 0.4$ are also shown and well agrees with the predictions of theory. Figure from [P5].*

to be practically the same in the regimes (A) and (B) considered in this work. Despite the large increase of $\mathcal{P}_0$, the total polarization $\mathcal{P}_{\rm tot}$ turns out to be practically independent of T in a wide range of temperatures. The above discussion suggests that, in the collisionless regime, the thermal atoms are locked to the condensate and oscillate in opposite phase in the spin-dipole dynamics. In the collisional regime (Fig. 20b), instead, the thermal part quickly relaxes to equilibrium, because of spin drag.

Using the experimental method introduced in Ref. [P7] we measure the static spin polarizability for the trap geometry (B) and identify the contributions that arise from the condensate and from the thermal part. Starting with both $\uparrow,\downarrow$ components perfectly overlapped in the harmonic potential, we apply a slowly increasing force $F_{\uparrow,\downarrow}$ to each component that eventually shifts their trap minima by $\pm x_0$. In this way the global center of mass is unaffected, while the superfluid and thermal spin components acquire finite relative displacements $\{S_0, S_T\}$. The spin polarizability of the condensed and thermal fractions $\{\mathcal{P}_0 \equiv S_0/(2x_0), \mathcal{P}_T \equiv S_T/(2x_0)\}$ are extracted in the linear regime, *i.e.*, for values of $\{S_0, S_T\}$ much smaller than the Thomas–Fermi radius of the condensed component [P7] [347]. Figure 22 shows the spin displacements $\{S_0, S_T\}$ of the thermal and condensed components of the mixture as a function of x_0 for $N_0/N = 0.4$. From this data, we extract the polarizability by performing a linear fit around the origin. The region where we fit the data to extract the value of the polarizabilities corresponds to the small x_0 linear regime ($R_x = 230\,\mu$m is the Thomas–Fermi radius along x). The analysis of the data points out the occurrence of a large polarization of the condensate, in accordance with the predictions of theory (see Fig. 21).

Conclusion

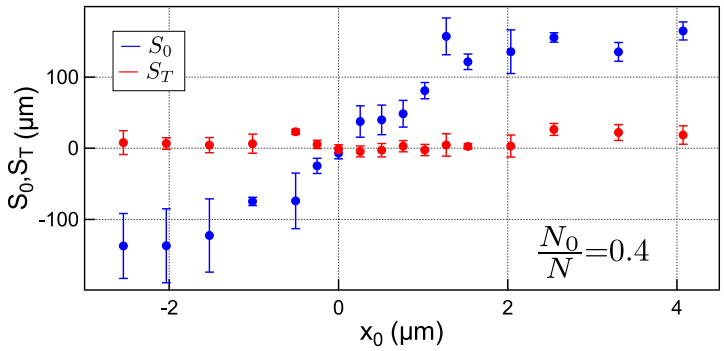

Figure 22. *Measured spin displacements* $\{S_0, S_T\}$ *for the thermal (red) and condensed components (blue) of the mixture as a function of* x_0 *for* $N_0/N = 0.4$ *for configuration (B). From such data, we extract* $\{\mathcal{P}_0, \mathcal{P}_T\}$ *using a linear fit to the data in the linear region around the origin. We obtain* $\{\mathcal{P}_0 = 56(8), \mathcal{P}_T = -3(3)\}$. *Figure from [P5].*

In conclusion, we have investigated the spin dynamics and the spin polarizability of a superfluid Bose–Bose mixture at finite temperature. Our results reveal the occurrence of undamped spin oscillations, which are observed not only in the collisionless regime, where the mean field drives a counter-phase oscillation of the thermal part, but also in the presence of strong collisions, which are responsible for the relaxation of the thermal component, because of spin drag. The absence of friction of the spin motion in the collisional regime provides a direct proof of the spin superfluid nature of the system. We have also shown that, thanks to the vicinity to the miscible-immiscible phase transition, the interaction between the two spin clouds causes, at finite temperature, a large increase of the polarizability of the condensate with respect to the $T = 0$ value. Natural generalizations of the present work concern the study of persistent spin currents in ring geometries and the propagation of spin sound waves and magnetic solitons [327].

3. Quantum fluids of light in propagating geometry

3.1. Context

After exploring the well-established field of atomic quantum gases, I developed a strong interest for the exciting new topic of *quantum fluids of light* that took off around 2010 and benefits from the powerful tools of optics and quantum optics to prepare, detect and characterize the initial and final state of the system. In order to put my work in context, it is convenient to divide this research field into three different categories [67]:

- **Microcavity devices for the exploration of nonequilibrium physics** [68]. Photons trapped inside a single longitudinal mode of a transversely multimode microscopic cavity acquire an effective mass[14]. This led to the observation of Bose-Einstein condensation of photons [217] when elastic photon-photon collisions are engineered by placing a solution of dye molecules inside the mirrors of the microcavity. Due to the unavoidable losses of photons from the microcavity, the system is inherently in an "out-of-equilibrium" setting as it requires constant optical pumping to reach a steady state. Moreover, in the situation where matter (atoms, molecules, excitons, ...) strongly couples to the microcavity, the resulting quasi-particles, called *polaritons*[15], possess an effective mass and interact with weak nonlinear interactions that they inherit from their matter component. This platform led to the observation of polaritonic "out-of-equilibrium" Bose-Einstein condensation either in cryogenic environment [206] or at room temperature [250]. The weak interactions between the polaritons enable to consider this system as an interacting quantum fluid which was first evidenced by the demonstration of polariton superfluidity [10]. Recently, the ability to microstructure the photonic or polaritonic landscape paves the way to use these systems to investigate analogue quantum simulation with photons, including double-well structures [237] and uniform potentials for optical quantum gases [62], 1D or 2D tight binding polariton lattices [354] and topological states of light [303].

- **Propagating geometries for the study of conservative dynamics** [67]. When light propagates inside a nonlinear medium in the paraxial approximation the equation of the evolution of the transverse electric field is a nonlinear wave equation analogous to the 2D Gross-Pitaevskii equation which describes the dynamics of dilute two-dimensional ultracold gases. This analogy enables to consider light in this setting as a quantum fluid. The direction of propagation of light plays the role of an effective-time, diffraction in the transverse plane gives an effective mass to photons and leads to a kinetic term, the presence of a transverse profile of the index of refraction acts as an external trapping potential and the interactions between photons arise from the optical nonlinearity. If absorption can be neglected

[14] This is due to the low-frequency cutoff imposed by the cavity leading to a quadratic dispersion relation for photons.

[15] The polaritons are composite particle of light and matter and are often loosely referred to as "light" in the literature.

during the propagation of light (effective-time evolution) inside the nonlinear medium, the dynamics of the system is conservative contrary to the inherently driven-dissipative nature of microcavity devices. Experimentally, quantum fluids of light in propagating geometries have been investigated on three experimental platforms: thermo-optical media [400], photo-refractive crystals [269, 378] or hot atomic vapors [346] [P4]. They have been used to explore various hydrodynamic phenomena including the generation of optical vortices [91], the condensation of classical nonlinear waves [31, 232, 346, 378], dispersive shockwaves [404] [P3], and superfluid behaviors [269, 400] [P4]. Moreover, contrary to atomic Bose gases, quantum fluids of light in propagating geometry are generally probed far from equilibrium. Indeed, the initial state injected into the nonlinear medium can be engineered (amplitude, phase, quantum fluctuations) and does not correspond to a steady state. In addition, the size of the system over which the dynamics occurs is not sufficient to reach complete thermalization. This led to the observation of interesting physical phenomena like the observation of nonequilibrium prethermal states [P2] or the effect of a quench of the interactions when light enters and exits the medium [P1].

- **Strongly correlated fluids of light** [67]. The two kinds of quantum fluids of light that we previously discussed are associated with relatively weak photon-photon interactions for which mean field theories or semiclassical methods for treating quantum fluctuations (*e.g.* truncated Wigner methods) describe accurately the dynamics of the system. The new frontier of quantum fluids of light is to investigate the situation in which photons interact at the individual particle level leading to intriguing many-body quantum states of light made of many photons. Pioneering experimental efforts enabled to realize the first building block towards this goal: engineer strong photon-photon interactions [71] either in cavity systems or in propagating geometries. This progress led to the very recent observation of few-body strongly correlated quantum fluids of light including a few-photon Laughlin states [85], the chiral currents observed in a few-site plaquette for strongly interacting microwave photons [339], a 8-site photonic Mott insulator [257] and a 7 site strongly correlated fluid of light [350]. Experimental efforts are currently in progress to scale up the number of photons and study strongly correlated fluids of light made of many photons. At this stage, I will refer the interested reader to section 4 of this manuscript for further details on this topic as it is one of the research directions I am pursuing in Strasbourg.

In 2016, the team of quantum fluids of light at Laboratoire Kastler Brossel led by Alberto Bramati, a renowned expert in the field of polariton superfluidity with semiconductor microcavities [10], decided under the initiative of Quentin Glorieux to develop a new experimental platform to explore quantum fluids of light that would be complementary to the microvavity setup: *light propagation in a hot atomic vapor cell*. Note that, at that time, the group of Robin Kaiser was also working on this platform to explore "photon condensation". In September 2017, I joined the group of Alberto Bramati at Laboratoire

Kastler Brossel, excited by the challenge to develop this new platform and convinced that my previous expertise about light-matter interactions and ultracold Bose gases can greatly benefit the project.

After working on this project for four years, our joint efforts have helped establish light propagating in hot atomic vapors as a leading platform for the exploration of quantum fluids of light in propagating geometry. This was achieved by demonstrating several important experimental results, including the measurement of the dispersion relation of elementary excitations [P4][P14], the observation of dispersive shockwaves [P3][P13][P11], the effect of a quench of the photon-photon interactions on light prethermalization [P2] or on the quantum fluctuations of light [P1], theoretical investigations of spin-orbit-coupled fluids of light [P12], the development of new experimental methods to measure the strength of photon-photon interactions [P10], the exploration of attenuation-free non-diffracting Bessel beams [P16] and the first experimental efforts towards optomechanical signatures of light superfluidity [P15].

Among those results, I selected four of my articles which give a good overview of my contribution to this exciting field of research. Two of these articles probes *hydrodynamic phenomena with this new platform*: the dispersion relation of quasi-particle excitations [P4] and the observation of dispersive shockwaves [P3]. The two other articles highlight the *far-from-equilibrium character* of the fluid of light by looking at the *effect of a quench of the photon-photon interactions*: the prethermalization of a quantum fluids of light [P2] and the observation of Sakharov oscillations in the power spectrum of the light intensity (photon density) fluctuations [P1].

3.2. Hydrodynamic properties of quantum fluids of light

3.2.1. Observation of the Bogoliubov dispersion relation in a fluid of light [P4]

Abstract: Quantum fluids of light are photonic counterpart to atomic Bose gases and are attracting increasing interest for probing many-body physics quantum phenomena such as superfluidity. Two different configurations are commonly used: the confined geometry where a nonlinear material is fixed inside an optical cavity, and the propagating geometry where the propagation direction plays the role of an effective time for the system. The observation of the dispersion relation for elementary excitations in a photon fluid has proved to be a difficult task in both configurations with few experimental realizations. Here, we propose and implement a general method for measuring the excitations spectrum in a fluid of light, based on a group velocity measurement. We observe a Bogoliubov-like dispersion with a speed of sound scaling as the square root of the fluid density. This study demonstrates that a nonlinear system based on an atomic vapor pumped near resonance is a versatile and highly tunable platform to study quantum fluids of light.

Introduction

Superfluidity is one of the most striking manifestation of quantum many-body physics. Initially observed in liquid Helium [9, 205], the realization of atomic Bose-Einstein

condensates (BEC) has allowed detailed investigations of this macroscopic quantum phenomenon exploiting the precise control over the system parameters. Recently, another kind of quantum fluid made of interacting photons in a nonlinear cavity has brought new perspectives to the study of superfluidity in driven-dissipative systems, with many fascinating developments [63] such as the observation of polariton BEC [22, 206] and the demonstration of exciton-polariton superfluidity [10, 250].

A different photon fluid configuration, initially proposed by Pomeau and Rica more than twenty years ago [139] but long ignored experimentally, relies on the propagation of a intense laser beam through some nonlinear medium. In this 2D+1 geometry (2 transverse spatial dimensions and 1 propagation dimension analogous to an effective time), the negative third-order Kerr nonlinearity is interpreted as a photon-photon repulsive interaction. Few theoretical works addressing mostly hydrodynamic effects using this geometry have been recently proposed [66, 245] and investigated in photorefractive crystals [269], thermo-optic media [400, 401] and hot atomic vapors [346].

The theoretical framework used to describe quantum fluids of light relies on the analogy with weakly interacting Bose gases where the mean field solution has originally been derived by Bogoliubov [51, 222]. A fundamental property of the Bogoliubov dispersion relation is the linear dependence in the excitation wavevector at long wavelengths (sound-like) and the quadratic dependence at short wavelengths (free-particle like). Although this dispersion has been well characterized in atomic BEC experiments [198, 268, 300, 374], a direct measurement of this dispersion in a fluid of light remains elusive [391, 400]. In this section, we propose a general method to experimentally access the dispersion of elementary density excitations of a photon fluid. We show that the dynamics of these excitations is governed by a Bogoliubov-like dispersion and that our experimental platform, based on light propagation in hot atomic vapor, is promisings to study hydrodynamics effects emerging in fluid of light systems. Our experiment settles the question originally asked by R. Chiao two decades ago [77]: can one observe sound-like excitations and superfluidity of light ?

Even if photons in free space are essentially non-interacting particles, engineering an effective photon-photon interactions is possible by exploiting an optical nonlinear process. In our experiment, the third-order Kerr nonlinearity is induced by the propagation of a near-resonant laser field inside a hot Rubidium atomic vapor. The sign and the strength of the interactions can be finely tuned by adjusting the laser detuning with respect to the atomic resonance. The atomic density, given directly by the vapor temperature, provides an additional control over the strength of the interactions. This system has been extensively studied in the context of quantum and nonlinear optics [148], but the quantum fluid of light framework gives a better and more complete understanding about the physical phenomena discussed in this letter. This framework is derived from the Nonlinear Schrödinger Equation (NSE), describing the propagation along the z-direction of a monochromatic linearly polarized laser field $E(\mathbf{r}_\perp, z)$ in a nonlinear medium, when the paraxial approximation is valid:

$$i\,\frac{\partial E}{\partial z} = -\frac{1}{2k_0}\nabla_\perp^2 E - \left(k_0 n_2 |E|^2 + i\frac{\alpha}{2}\right) E, \tag{19}$$

where $k_0 = 2\pi/\lambda_0$ is the laser wavevector (λ_0 stands for the laser wavelength in vacuum) and $\nabla_\perp$ the gradient with respect to the transverse spatial coordinate $\mathbf{r}_\perp = (x, y)$. When the linear absorption coefficient α is negligible and the nonlinear refractive index $\Delta n = n_2 I$ (I represents the laser field intensity) is negative, the NLSE is mathematically analogous to the Gross-Pitaevski equation, describing the dynamics with respect to an effective time $t = zn_0/c$ (c stands for the speed of light in vacuum) of a 2D-fluid with repulsive interactions. Using the Madelung transformation $E(\mathbf{r}_\perp, z) = \sqrt{\rho(r_\perp, z)} \exp[i\,\Phi\,(r_\perp, z)]$, one obtains a coupled system of hydrodynamic equations for the electric field density ρ and phase Φ :

$$\frac{\partial \rho}{\partial t} + \boldsymbol{\nabla}_\perp \cdot (\rho \mathbf{v}) = 0, \tag{20}$$

$$\frac{c}{k_0}\frac{\partial \Phi}{\partial t} + \frac{1}{2}v^2 + c^2\left(n_2\rho - \frac{1}{2k_0^2}\frac{\nabla_\perp^2\sqrt{\rho}}{\sqrt{\rho}}\right) = 0, \tag{21}$$

where $\mathbf{v} = (c/k_0)\boldsymbol{\nabla}_\perp\Phi$. In this formulation, the laser beam is described as a fluid of density ρ flowing with velocity $\mathbf{v}$ in the transverse plane.

The dynamics of the density fluctuations on top of the photon fluid is governed by the Bogoliubov dispersion relation. For small amplitude modulations moving on a uniform background fluid at rest, the set of hydrodynamic equations can be linearized assuming $\rho = \rho_0(z) + \delta\rho(\mathbf{r}_\perp, z)$ and $\mathbf{v} = \delta\mathbf{v}(\mathbf{r}_\perp, z)$. By taking the transverse gradient of Eq. (21), keeping the first order terms in the expansion and using Eq. (20), one can derive an equation for $\delta\rho$ only. For a plane-wave density fluctuation mode $\delta\rho$ of wave vector $\mathbf{k}_\perp$, the associated response frequency Ω_B will follow the dispersion relation below :

$$\Omega_B(\mathbf{k}_\perp) = c\sqrt{|\Delta n|\,\mathbf{k}_\perp^2 + \left(\frac{\mathbf{k}_\perp^2}{2k_0}\right)^2}. \tag{22}$$

When the wavelength $\Lambda = 2\pi/|\mathbf{k}_\perp|$ of the modulation is longer than the *healing length* $\xi = \frac{\lambda}{2}\sqrt{\frac{1}{|\Delta n|}}$, the dispersion relation becomes linear and the modulations propagate as sound waves. This regime is characterized by the sound velocity $c_s = c\sqrt{|\Delta n|}$, which only depends on the nonlinear index of refraction Δn. Conversely, when $\Lambda \gg \xi$, the dispersion relation becomes quadratic which is similar to the free propagating particle one.

Observing the sound like-regime of the Bogoliubov dispersion relation has been proposed in [66] and first attempted in [400] for propagating geometries. The approach used in [400] relies on the measurement of the phase velocity difference between plane wave density modulations propagating at a given transverse wavevector $k_\perp = 2\pi/\Lambda$ on top of a high and a low density photon fluid. The photon fluid is obtained by sending a wide laser beam through a self-defocusing nonlinear medium; the fluid density is then given by the light intensity. The small amplitude plane wave density modulation is produced by interfering this first beam with a wide and weak probe field, propagating with a small angle with respect to the optical axis. In this configuration, however, a *conjugate* wave

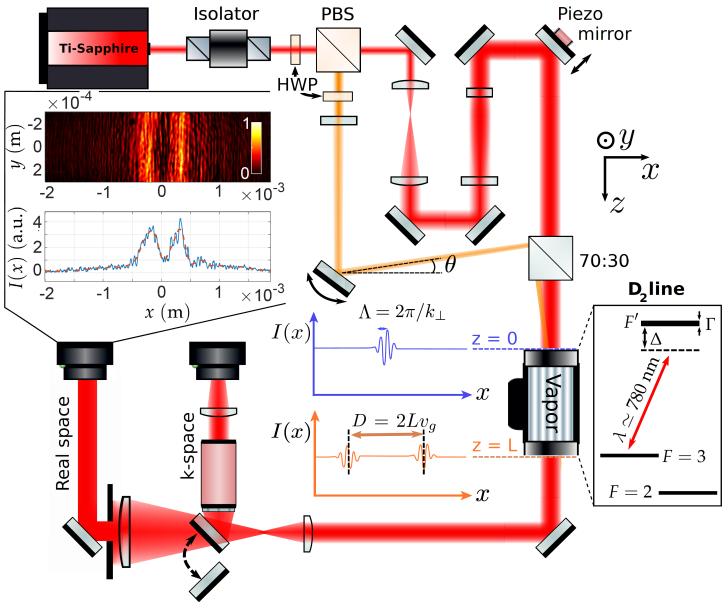

Figure 23. *Experimental setup. PBS and HWP stand for Polarized Beam Splitter and Half-Wave Plate respectively. θ is the angle between the probe (orange beam) and the optical axis defined by the pump (red beam). The probe interferes with the pump and slightly modulates its intensity. Blue inset: integrated intensity profile at the input of the medium ($z = 0$). The wavelength Λ of the density modulation is given by $2\pi/k_\perp$ where $k_\perp = k_0 \sin\theta$. Orange inset: integrated intensity profile at the output of the medium ($z = L$). The distance D between the two wavepackets gives access to the group velocity of the elementary excitations in the transverse plane. The output plane is imaged on a CMOS camera. Inset on the top left: background-subtracted image obtained for $\theta \approx 0$ rad and associated integrated envelope profile (blue: original ; red dotted : high frequency filtered). Figure from [P4].*

propagating in the opposite transverse direction ($-\mathbf{k}_\perp$) is spontaneously generated at the linear/nonlinear interface [245] . Probe and conjugate overlap and interfere, which strongly alters the phase shift measurement used to determine the dispersion relation. Moreover, the large nonlinearity needed to observe the sonic dispersion makes extracting the dispersion relation from this measurement rely on a complex numerical inversion [244]. On the contrary, we present a direct and intuitive method to extract the dispersion relation for arbitrary modulation wavelengths.

Our approach is based on the measurement of the group velocity of a small amplitude Gaussian wavepacket travelling on top of the photon fluid with the transverse wave vector $k_\perp$. This wavepacket is designed by interfering the wide and intense beam forming the fluid (at $\mathbf{k}_\perp = \mathbf{0}$) with a Gaussian probe at $\mathbf{k}_\perp = k_0 \sin\theta\, \mathbf{e}_x$, as depicted in Fig. 23. At the entrance of the nonlinear medium, the effective photon-photon interaction constant undergoes a sudden jump along the optical axis. Two counter-propagating wavepackets are spontaneously created from the initial Gaussian perturbation and evolve over the effective time t through the nonlinear medium, with a transverse group velocity $\pm v_g$.

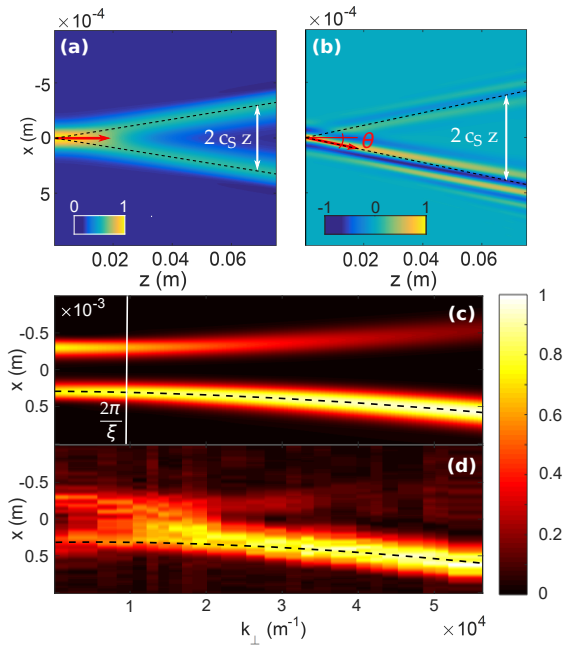

Figure 24. *Simulation of the propagation of a weak transverse modulation through a nonlinear medium (a) with zero transverse speed ($\theta = 0$ rad). The modulation generates two counter propagating modes (Bogoliubov modes) at the medium interface and get amplified until they separate from each other. The wavepacket is not spreading along propagation due to the non-dispersive regime (sound-like behavior). (b) Same as (a), for an incident probe at $\theta = 5 \times 10^{-3}$ rad (high transverse speed). Interference fringes appear and the wavepacket spreads. (c) simulation of the intensity profile envelope in the output plane for different probe wavevector. Dashed black: group velocity given by Eq. (22). (d) experimental data. The parameters in (a), (b) and (c) are those used to obtain the experimental data (d) : $\lambda_0 = 780$ nm, $\Delta n = 1.310^{-5}$ and $\omega_x^p = 180\,\mu$m. The absorption coefficient α was set to 0 in numerical simulations. Colorbars encode the light intensity in arbitrary units. Figure from [P4].*

The separation between these two modulations at a given propagation distance z (*i.e.* at given time t), is a direct measurement of the group velocity. In the output plane ($z = L$), this distance is given by $D(k_\perp) = 2Lv_g(k_\perp)$. The dispersion relation $\Omega_B(k_\perp)$ is reconstructed by scanning the wavevector of the modulation $k_\perp$ (tuning the angle θ between pump and probe) and integrating the group velocity v_g: $\Omega_B(k_\perp) = \int_0^{k_\perp} v_g(q)\,\mathrm{d}q$.

In order to illustrate our method, we solve numerically the NSE Eq. (19) to get the evolution of the transverse electric field (pump + probe). We use the second-order split step Fourier method, for one transverse spatial dimension only (1D+1 geometry) to take advantage of symmetries in the flat fluid density situation (infinitely wide background beam). The probe waist is located in the entrance plane at $z = 0$; its width ω_x^p is the same as the one used in the experiment. For all the density plots in Fig. 24, the uniform background intensity has been subtracted. The evolution of the two counter-propagative modulations generated at the entrance of the nonlinear medium is shown in Fig. 24(a)

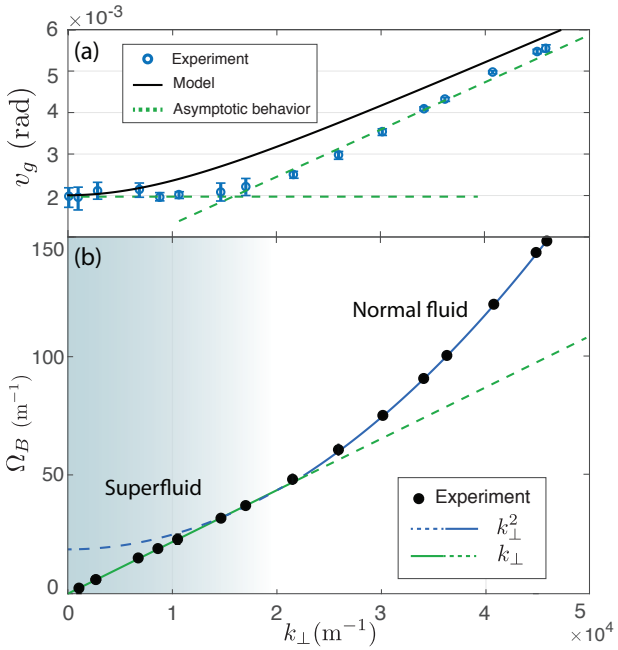

Figure 25. *a) Group velocity as a function of the transverse wavevector $k_\perp$. The circles represent the experimental data obtained for $P = 175$ mW. The theoretical model is plotted in solid dark (parameters extracted from an independent measurement of the nonlinearity – see text for details). The dashed green lines are the asymptotic behaviors: constant group velocity at small $k_\perp$ and linear increase at large $k_\perp$. b) Dispersion relation obtained after integration of the group velocity. Linear (green) and parabolic (blue) dispersion curves are plotted as a reference. Figure from [P4].*

for zero initial transverse speed and presents a sound like-behavior (no spreading of the wavepacket). The Fig. 24(b) is obtained for on high transverse initial speed modulation which behaves like a free-particle. Notice that for small incident angle, corresponding to zero initial transverse speed, the two modulations generated at the entrance of the nonlinear medium acquire a non-zero opposite transverse speed. This nonlinear refraction law comes from the linear nature of the dispersion for $k_\perp \ll 2\pi/\xi$ [245], which is counter-intuitive from the linear optics perspective. The envelope of the intensity profile in the output plane is presented as a function of the probe wavevector in Fig. 24(c), on top of the experimental results in Fig. 24(d). The black dotted line represents the theoretical group velocity v_g, obtained by taking the derivative of Eq. (22). The distance between the two wavepackets is constant for $k_\perp \lesssim 2\pi/\xi$ (linear dispersion; constant v_g) and linearly increase for larger $k_\perp$ (quadratic dispersion; $v_g \propto k_\perp$).

The experimental setup is shown in Fig. 23. A continuous-wave Ti:Sapphire laser beam is split into two beams: a low power probe and a high power pump. The pump is expanded twice before being focused in the center of the nonlinear medium with two cylindrical lenses to create an elliptical beam with a width along x of $\omega_x^0 \approx 3.2$ mm and a width along y of $\omega_y^0 \approx 300\,\mu$m. The pump intensity in the central region can thus be considered as spatially uniform along x. The Rayleigh length $z_{R,y}^0$ associated to ω_y^0 is

37 cm, which is five times longer than the length of the nonlinear medium. Therfore, We can safely consider the pump beam as being collimated and neglect its divergence along the propagation direction. The probe is directly focused with a cylindrical lens on the entrance of the nonlinear medium in order to get a flat phase profile. This beam is elliptically elongated along the y direction. We set the major axis width ω_y^p to 1700 μm and ω_x^p to $180 \pm 10\,\mu$m in order to properly separate the Gaussian wavepackets in the output plane and conserve the probe collimation along its propagation in the nonlinear medium ($z_{R,x}^p \approx 13$ cm). We fix the probe intensity at its waist to 1% of the pump intensity. This pump/probe cross configuration enables us to both get closer to the 1D case and to increase the integration range along y. The angle θ between pump and probe in the (xz) plane can be finely tuned thanks to a piezo-actuated mirror mount.

Both beams propagate through a $L = 7.5$ cm long cell, filled with an isotopically pure ^{85}Rb vapor. The cell is heated up to 150°C by an oven designed to reduce air turbulence close to the cell windows. Adjusting the temperature allows us to control the atomic density and therefore the strength of the optical nonlinearity. In our case, this optical nonlinearity is obtained by tuning the laser frequency close to the ^{85}Rb D_2 resonance line, composed of 2 hyperfine ground states ($F = 2, 3$) and 4 hyperfine excited states ($F' = 1$ to 4). Since the laser is highly red-detuned from the $F = 3 \rightarrow F'$ transitions ($\Delta = -6$ GHz), the Doppler broadening can be safely neglected and the negative nonlinear susceptibility is close to the one of an effective two-levels system with only one excited state of decay rate $\Gamma = 6.06$ MHz. At these temperature and detuning, the transmission coefficient of the laser beams through the cell is above 70%, which allows one to neglect multiple scattering of light (atom-light interaction processes are mainly dominated by Rayleigh scattering events). In comparison to [400], we can consider that the nonlinear interactions are local, as long as the length scale of the ballistic transport of excited atoms stays much shorter than the healing length, which is the case at that temperature.

The output plane of the cell is imaged on a CMOS camera. A microscope objective can be flipped on the beam path to image the far-field (*i.e.* k-space) and measure the probe transverse wavevector $k_\perp = k_0 \sin\theta$. For every angle θ, the pump intensity (background), the probe intensity and the k-space are captured. The relative phase between pump and probe is scanned over 2π. 40 background-subtracted images are taken during the phase scan. They are then integrated over one hundred pixels around (Ox) and averaged in absolute values. Averaged images before integration are shown in inset of Fig. 23(b). The distance D between the counter-propagating wavepackets is estimated by performing a two-Gaussian fit for small $k_\perp$ *i.e.* when the conjugate beam is visible. For large $k_\perp$, the conjugate is not sufficiently amplified anymore and D is directly measure from the distance between the input and output positions of the probe beam. In order to fully characterize our system, the third order Kerr susceptibility n_2 is calibrated independently by measuring the self phase accumulated by a slightly defocusing Gaussian beam propagating through the cell [287, 424]. With the detuning and temperature reported earlier, we found $n_2 = 3.1 \pm 0.2\,10^{-11}$ m^2/W.

The experimental group velocity and dispersion relation as a function of the probe transverse wavevector are shown in Fig. 25. The pump power was set at 175 mW leading

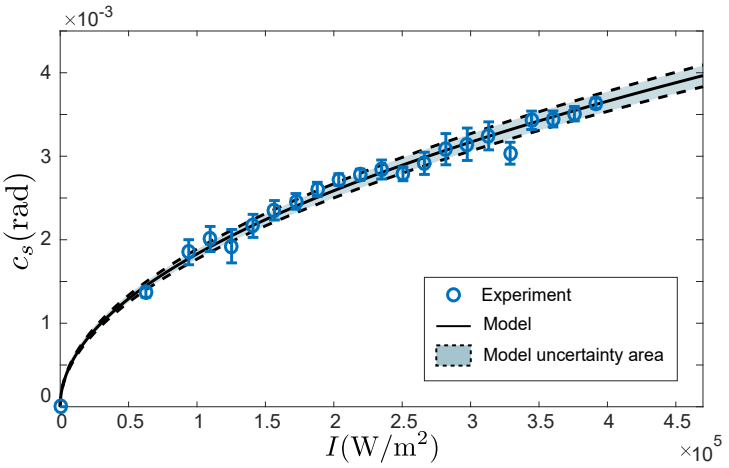

Figure 26. *Speed of sound c_s as a function of the pump intensity. Due to the 2D+1 geometry, the speed of sound has the dimension of an angle. Data is plotted in blue dots. The light intensity corresponds to the fluid density, therefore a scaling as square-root is expected as plotted in black solid. No free parameters are needed as the nonlinearity has been measured independently. Uncertainty area in light blue is extracted from this independent measurement. Figure from [P4].*

to a nonlinear refractive index Δn of $3.9\,10^{-6}$. Two different regimes can be identified on Fig. 25(a): a constant group velocity at low $k_\perp$ and a linear increase at larger $k_\perp$. The group velocity clearly goes toward a non-zero value when $k_\perp \to 0$, breaking the linear trend characteristic of the standard free-particle dispersion. The theoretical model plotted in Fig. 25 is obtained with no free fitting parameters. The offset at large $k_\perp$ between the model and the experimental data results from constructive interferences between the two non-fully separated wavepackets, as can be seen on the experimental data of Fig. 24(d) around $k_\perp \sim 1.5\,10^4$ m^{-1} (the envelope intensity significantly increases in between them leading to a systematic under-estimation of the distance D by the two-Gaussians fit). After propagation in the cell, the counter-propagating wavepackets have respectively accumulated the phase $\pm\Omega_B(k_\perp)\,L$. Constructive interferences occur when $\Omega_B(k_\perp)\,L = n\pi$ (n is a positive integer) *i.e.* for $k_\perp \sim 1.8\,10^4$ m^{-1} when $n=1$. This value gives the position of the end of the plateau-like regime at low $k_\perp$. Another constructive interference should occurs for $k_\perp = 0$ (when $n=0$), but as both envelopes have the same amplitude in that case, the two peaks are still disentangle (see inset of Fig. 23).

More importantly, the dispersion relation of Fig. 25(b) guarantees that light is superfluid in our experiment. Indeed, the Landau criterion for superfluidity defines a critical transverse speed $v_c = \min_{k_\perp}\left[\frac{\Omega_B}{k_\perp}\right]$ for the photon fluid, below which the emission of sound-like excitations is not possible anymore. In our case, $v_c = c_s > 0$ and one could observe superfluid flow of light around a defect if its transverse velocity v (measured in the defect frame) was lower than c_s. To investigate the sonic regime, we set the probe wavevector to zero and record directly the sound velocity as function of the background fluid density

(the pump intensity I). The experimental data are shown in Fig. 26 (blue circles). We observe that the speed of sound scales with the square-root of the fluid density (plotted in black solid) as expected. It is worth mentioning that, once again, the third order Kerr susceptibility measured independently, sets the only parameter of the theoretical model.

Conclusion

In conclusion we have reported two important experimental results: first we measured the dispersion relation for small amplitude density fluctuations, which shows a linear trend at low wavevector, characteristic of a superfluid. We have then assessed the associated sound velocity for different fluid of light densities and obtained a scaling law analogous to the hydrodynamic prediction. This settles the question initially asked by Chiao about the possibility to observe a superfluid dispersion in a photon fluid. These results open a wide range of possible experiments in hydrodynamics with light using a novel versatile platform based on hot atomic vapors.

3.2.2. Quantitative analysis of shock wave dynamics in a fluid of light [P3]

Abstract: We report on the formation of a dispersive shock wave in a nonlinear optical medium. We monitor the evolution of the shock by tuning the incoming beam power. The experimental observations for the position and intensity of the solitonic edge of the shock, as well as the location of the nonlinear oscillations are well described by recent developments of Whitham modulation theory. Our work constitutes a detailed and accurate benchmark for this approach. It opens exciting possibilities to engineer specific configurations of optical shock wave for studying wave-mean flow interaction.

Introduction

In many different fields such as acoustics [157], plasma physics [193], hydrodynamics [101, 238, 302], nonlinear optics [5], ultracold quantum gases [69, 99, 200, 202], the short time propagation of slowly varying nonlinear pulses can be described discarding the effects of dispersion and dissipation. The prototype of such an approach is given by the system of equations governing compressible gas dynamics [332]. This type of treatment typically predicts that, due to nonlinearity, an initially smooth pulse steepens during its time evolution, eventually reaching a point of gradient catastrophe. This is the wave-breaking phenomenon, which results in the formation of a shock wave [92, 420]. If, after wave breaking, dispersive effects dominate over viscosity, the shock eventually acquires a stationary nonlinear oscillating structure for which the width increases with diminishing dissipation [345]. In the case of weak dissipation the time for reaching a stationary regime can be quite long. Gurevich and Pitaevskii [161] made a major contribution to the field when they first realized the interest of studying the evolution of the associated dynamical structure, now called a dispersive shock wave (DSW). Besides, they understood that

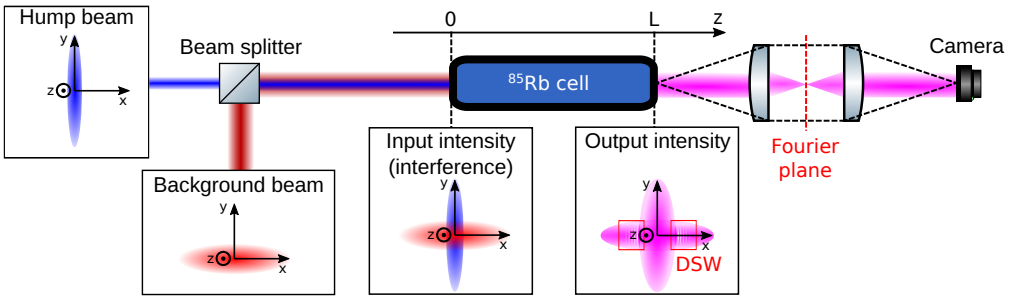

Figure 27. *Sketch of the experimental setup. To create the initial state we overlap the background and the hump beams on a beam splitter with their relative phase precisely adjusted such that they interfere constructively. This state then propagates inside the nonlinear medium consisting of a hot ^{85}Rb vapor cell of length L. The insets represent cuts of the relevant intensity profiles in the plane perpendicular to the direction z of propagation. The output intensity is recorded on a camera by direct imaging through two lenses in $4f$ configuration. Figure from [P3].*

a DSW can be described as a modulated nonlinear traveling wave and studied in the framework of the Whitham theory of modulations [410].

In the present work we study the propagation of an optical beam in a nonlinear defocusing medium. Wave-breaking and (spatial or temporal) dispersive shocks have already been observed in such a setting [30, 94, 120, 126, 143–145, 197, 298, 337, 404, 409, 415, 416]. However, all previous theoretical descriptions of experimental optical shocks either remained only qualitative or resorted to numerical simulations for reaching accurate descriptions. Indeed, a realistic quantitative characterization of the experimental situation requires to take into account a number of nontrivial effects which sum up to a quite difficult task. For instance, saturation effects, such as occurring in semiconductor doped glasses [93] and in photorefractive media [216], can only be taken into account by using a nonintegrable nonlinear equation, even for a medium with a local nonlinearity. Besides, both "Riemann invariants" typically vary during the prebreaking period and this complicates the description of the nondispersive stage of the pulse spreading, even in a quasi unidimensional (1D) geometry. Moreover, for realistic initial intensity pulse profiles, the post-breaking evolution corresponds, at best, to a so-called "quasisimple" dispersive shock [158], the characterization of which requires an elaborate extension of the Gurevich-Pitaevskii scheme. Finally, the nonintegrability of the wave equation significantly complicates the post-breaking description of the nonlinear oscillations within the shock. Despite these difficulties, it has recently become possible to combine several theoretical advances [116–119, 137, 159, 160, 186, 187, 204, 221, 233] to obtain a comprehensive treatment of the nonlinear pulse spreading and the subsequent formation of a dispersive shock in a realistic setting [188, 189]. In this Letter, we provide a nonambiguous experimental evidence for the accuracy of this theory with a precise description of the main features of the shock. This universal and quantitative benchmark is a major advance for manipulation and engineering of optical shockwaves.

We study the propagation of a laser field in a $L = 7.5$ cm-long cell filled with an isotopically pure ^{85}Rb vapor (99% purity) warmed up to a controlled temperature of

120 °C to adjust the atomic vapor density. We use a Ti:sapphire laser detuned by −3.9 GHz with respect to the $F = 3 \to F'$ transition of the D2-line of ^{85}Rb at $\lambda_0 = 2\pi/k_0 = 780$ nm. For such a large detuning, the natural Lorentzian shape of the line dominates and the Doppler broadening $k_0 v \simeq 240$ MHz can be safely neglected. In these experimental conditions, the system is self defocusing (repulsive photon-photon interaction) and the transmission through the cell is 60 %. We find that this medium is well described by local photon-photon interactions, but contrary to previous works [54, 269, 346] [P4] [P14] we find it important to take into account the saturation of the nonlinearity to quantitatively describe the dynamics of the shock waves.

The input intensity profile is a cross-beam configuration of two vertically polarized laser beams, both propagating along the axis of the cell (denoted as Oz), with their respective phase precisely adjusted such that the two beams interfere constructively, see Fig. 27. One of the beams (which is denoted the *hump*) is extended along the y direction and significantly more intense than the other one (the *background*) which is extended along the x direction. At the entrance of the cell ($z = 0$) both beams have an elliptic Gaussian profile. The background beam has a power P_0 and waists $w_{x,0} > w_{y,0}$, whereas the hump has power P_1 and waists $w_{x,1} < w_{y,1}$. During the initial nondiffractive stage of evolution, nonlinearity acts as an effective pressure which favors spreading of the hump in the x direction along which is initially tighter collimated. Conversely, the low intensity background experiences almost no spreading and behaves as a pedestal which triggers wave breaking of the hump during its spreading. Each beam has a maximum entrance intensity $\mathcal{I}_\alpha = 2P_\alpha/(\pi w_{x,\alpha} w_{y,\alpha})$ ($\alpha = 0$ or 1), and we explore the DSW dynamics for a fixed ratio $\mathcal{I}_1/\mathcal{I}_0$. We work in the deep nonlinear regime, with $\mathcal{I}_1 = 20\,\mathcal{I}_0$. This large value corresponds to a wave breaking distance typically shorter than the cell length, and makes it possible, by changing the total power $P_{\rm tot}$ of the beams, to observe several stages of evolution of the DSW. The total power can be increased up to 700 mW and is limited by the laser maximum output power.

We image the total field intensity $I_{\rm out}(x, y)$ at the output of the cell on a camera. In order to minimize the effect of absorption and increase the visibility of the DSW, we determine the *normalized* output intensity

$$\widetilde{I}_{\rm out}(x, y) \equiv \frac{I_{\rm out}(x, y) - I^0_{\rm out}(x, y)}{\mathcal{I}^0_{\rm out}}, \tag{23}$$

where $I^0_{\rm out}(x, y)$ is the intensity profile at the cell output when *only* the background beam propagates through the medium (the hump beam is blocked). $\mathcal{I}^0_{\rm out}$ is the maximal value of $I^0_{\rm out}(x, y)$. $\widetilde{I}_{\rm out}(x, y)$ is represented in Fig. 28(a). Our theoretical description relies on only two parameters which characterize the photon-photon interaction, namely, the Kerr coefficient, n_2, and the saturation intensity $I_{\rm sat}$ [cf. Eq. (24)]. Their values $n_2 = 1.5 \times 10^{-4}$ mm^2/W, and $I_{\rm sat} = 0.6$ W/mm^2 have been determined by comparing the experimental results with large-scale 2D numerical simulations. The excellent agreement reached in Fig. 28 indicates that two effects – saturable nonlinearity and linear absorption – are the relevant physical ingredients for a theoretical description of our experiment.

In the regime $w_{1,x} \ll w_{0,x}$ and $\mathcal{I}_1 \gg \mathcal{I}_0$ we consider, the normalized output density

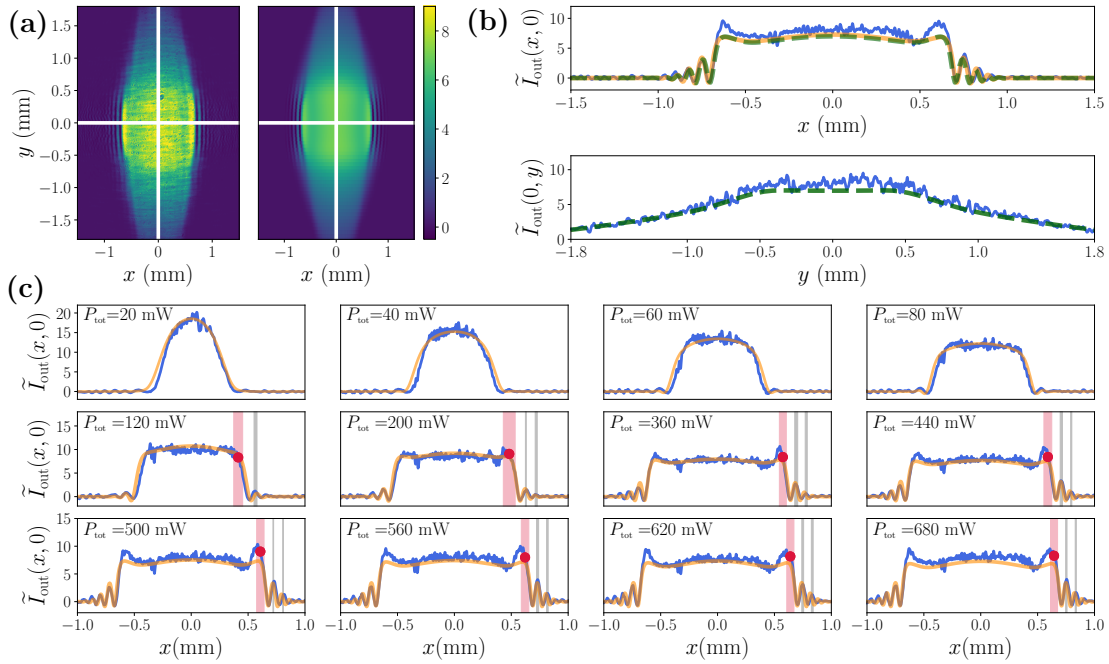

Figure 28. *(a) Left: experimental profile $\widetilde{I}_{out}$ taken for $P_{tot} = 680\,mW$. Right: Two-dimensional numerical simulations at the same total entrance power. (b) x and y profiles along the cuts represented by the two white lines on the two-dimensional profiles (a). The solid blue line represents the experimental data, the dashed green line the two-dimensional numerical simulation. On the x profile, the orange line is a one-dimensional numerical simulation, from Eqs. (24) and (25). (c) $\widetilde{I}_{\rm out}(x,0)$ for various total beam powers. The color code is the same as in (b). The vertical pink and gray bars on the right part of each intensity profile indicate the positions of the solitonic edge of the DSW and of the first maxima of oscillations within the DSW. The thickness of each bar represents the experimental uncertainty. Figure from [P3].*

$\widetilde{I}_{\rm out}$ becomes independent on the precise shape of the background beam. As a result, $\widetilde{I}_{\rm out}(x,0)$ can be described by using a simplified 1D theoretical description, where a hump propagates over a background of *uniform* intensity $\mathcal{I}_0$. Within the cell, the complex field amplitude at $y = 0$, denoted as $\mathcal{A}(x,0,z) \equiv a(x,z)$, then obeys a 1D nonlinear Schrödinger equation where the position z along the axis of the beam plays the role of an effective "time" [241]. The equation, once included the nonlinearity saturation and the linear absorption [216], reads

$$i\,\partial_z a = -\frac{1}{2n_0 k_0}\partial_x^2 a + \frac{k_0\, n_2\, |a|^2}{1+|a|^2/I_{\rm sat}}\, a - \frac{i}{\Lambda_{\rm abs}}\, a, \tag{24}$$

where $n_0 \simeq 1$ is the linear index of refraction and $\Lambda_{\rm abs} = 30$ cm, which corresponds to a 60 % transmission for a cell of length $L = 7.5$ cm. The value of the effective amplitude

at the entrance of the cell is taken as

$$a(x,0) = \sqrt{\mathcal{I}_0} + \sqrt{\mathcal{I}_1}\exp\left(-\frac{x^2}{w_{x,1}^2}\right), \tag{25}$$

In order to evaluate the accuracy of the mapping to the 1D model of Eq. (24), we compare in the upper panel of Fig. 28(b) the corresponding value of $|a(x,L)|^2\exp(2L/\Lambda_{\rm abs})/\mathcal{I}_0 - 1$ with the experimental $\widetilde{I}_{\rm out}(x,0)$ and with the result of 2D simulations. The excellent agreement is confirmed in Fig. 28(c) for the whole range of beam powers $P_{\rm tot}$.

The mapping to a 1D problem enables us to compare our measurements with recent analytical predictions. In particular, if one neglects the linear absorption within the cell, for the initial intensity profile (25), wave breaking occurs at a propagation distance [186]

$$z_{\rm WB} = 4\sqrt{\frac{n_0 I^*}{n_2}}\,\frac{(1+I^*/I_{\rm sat})^2}{3+I^*/I_{\rm sat}}\cdot\frac{1}{\max\left|\frac{dI(x,0)}{dx}\right|}, \tag{26}$$

where $I(x,0) = |a(x,0)|^2$ is the entrance intensity and I^* is the value $I(x^*,0)$ at point x^* where $|dI(x,0)/dx|$ reaches its maximum. For low entrance power, no DSW is observed because $z_{\rm WB}$ is larger than the cell length. Wave breaking first occurs within the cell for a total power $P_{\rm WB}$ such that $z_{\rm WB} = L$. For our experimental parameters we obtain $P_{\rm WB} = 48$ mW. Numerical tests show that taking absorption into account does not modify notably this value.

For a total power larger than $P_{\rm WB}$, the DSW is formed and develops within the cell. The physical phenomenon at the origin of the DSW is the following: large intensity perturbations propagate faster than small ones, so there exist values of x reached at the same "time" by different intensities. When this occurs first, the density gradient is infinite. This corresponds to the onset of a cusp catastrophe [150, 203], the nonlinear diffractive dressing of which is a dispersive shock wave. This takes the form of a modulated oscillating pattern consisting asymptotically (i.e. at large z, or equivalently large $P_{\rm tot}$) in a train of solitons which, away from the center of the beam, gradually evolves into a linear perturbation. The position of its "solitonic edge" on the $y = 0$ axis at the cell output ($z = L$) is denoted as x_s. It is located in Figs. 28(c) by a vertical red bar whose thickness represents the uncertainty on the estimation of x_s from the experimental $\widetilde{I}_{\rm out}(x,0)$. This uncertainty limits the experimental determination of x_s to powers larger than 120 mW. The following maxima of oscillations, represented by vertical gray lines, are more precisely determined experimentally. The technique devised in Ref. [189] makes it possible to theoretically determine x_s and the corresponding intensity $\widetilde{I}_{\rm out}(x_s,0)$. As illustrated in Fig. 29 the results of this analytical approach (green solid lines) compare well with the experimental data, although it does not take absorption into account. Importantly, omission of the nonlinearity saturation leads to incorrect results (brown solid line).

One may study the DSW in an even more detailed way by locating the position of the maxima of the nonlinear oscillations. While the theoretical results for x_s essentially rely on an approach due to El [116, 160, 204] which is valid for any type of nonlinearity, the precise intensity profile within the DSW can be computed only for exactly integrable

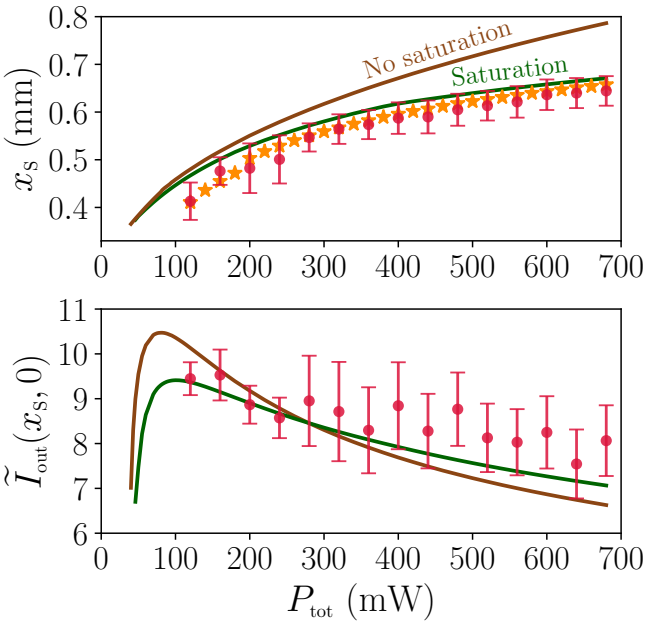

Figure 29. *Characterization of the solitonic edge of the DSW as a function of the beam's power. The upper panel represents the position x_s of the shock, and the lower one the corresponding intensity $\widetilde{I}_{\rm out}(x_s, 0)$. In each panel, the red points with error bars are experimental results, from Fig. 28(c) and, in the upper one, the orange stars are the results of 1D numerical simulations of Eq. (24). The green solid line is the theoretical result, from Ref. [189]. The brown solid line is the theoretical result in the absence of saturation. Figure from [P3].*

systems, i.e., by neglecting saturation effects. The position-dependent oscillation period $\mathcal{L}(x, z)$ was computed in this framework in Ref. [188] for a parabolic initial intensity distribution. Fitting the center of the intensity profile (25) by an inverted parabola, the positions x_1, x_2, and x_3 of the first maxima of oscillation of the DSW at the output of the cell are determined by

$$x_1 - x_s = \mathcal{L}\left(\frac{x_s + x_1}{2}, L\right), \tag{27}$$

and by similar formulas obtained by replacing x_1 by x_2 (then x_3) and x_s by x_1 (then x_2). The results are compared with the experimental ones in the upper half ($x > 0$) of Fig. 30. The small offset in the position of the theoretical maxima with respect to the experimental ones observed in the figure is due to an initial small overshoot in the theoretical position of x_s (cf. the green solid line in Fig. 29) which is itself due to the absence of absorption in the model. Indeed, the 1D numerical simulations – which do take absorption into account – are in slightly better agreement with the experimental results for x_s (cf. the orange stars in Fig. 29). Using the numerical x_s in Eq. (27) instead of the analytical one yields, for the maxima of oscillations, an excellent agreement with

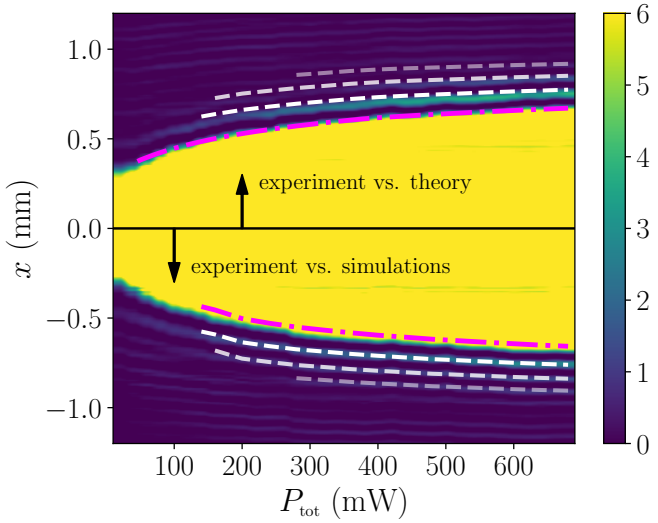

Figure 30. *Color plot of the experimental intensity profiles $\widetilde{I}_{out}(x,0)$ as a function of P_{tot}. The purple dot-dashed line represents the edge x_s of the DSW extracted from Whitham theory (upper part of the figure: $x>0$) and from 1D numerical simulations (lower part, $x<0$). In each half of the figure ($x \lessgtr 0$) the white dashed lines are the corresponding analytic predictions (27) for the maxima of oscillation. Figure from [P3].*

experiment, cf. the lower half of Fig. 30. Such a good agreement despite the fact that Eq. (27) does not take saturation into account is not surprising: the rapid decrease of intensity away from the solitonic edge (cf. Fig. 28) significantly reduces the importance of saturation within the DSW.

Conclusion

It thus appears possible to give a detailed description of precise experimental recordings of the intensity pattern of an optical shock wave, not only thanks to numerical simulations, but on the basis of Whitham's modulation theory. This is an important validation of recent advances in this approach, which is no longer restricted to integrable systems or idealized initial configurations. We are reaching a point where these progresses make it possible not only to study DSWs *per se*, but also as tools for prospecting new physical phenomena, such as the type of wave-mean flow interaction recently identified in Ref. [90]: our platform is ideally designed to investigate scattering of elementary excitations by a DSW, a study which is also relevant to the domain of analogue gravity. Indeed, a dispersive shock can be considered as an exotic model of acoustic white hole, and the good experimental control and theoretical understanding of this structure demonstrated in the present work opens the prospect of a detailed investigation of the corresponding induced background fluctuations.

3.3. Out-of-equilibrium dynamics of a quantum fluid after an interaction quench

3.3.1. Nonequilibrium prethermal states in a two-dimensional photon fluid [P2]

Abstract: We report on the observation of a prethermal state in a nonequilibrium, two-dimensional fluid of light. Direct measurements of the first order coherence function of the fluid reveal the dynamical emergence of algebraic correlations, a quasi-steady-state with properties close to those of thermal superfluids. By a controlled increase of the fluctuations, we observe a crossover from algebraic to short-range (exponential) correlations. We interpret this phenomenon as a nonequilibrium precursor of the Kosterlitz-Thouless transition.

Introduction

Thermalization is the dynamical process by which any subpart of a many-body system evolves toward a thermal equilibrium state that maximizes its entropy. While a general description of how thermal equilibrium establishes in quantum systems remains elusive, a variety of scenarios have been identified [149, 319]. Examples include the nonequilibrium dynamics of near-integrable systems [214], the relaxation toward thermalization in correlated gases [386], the spontaneous emergence of universal scaling laws [121, 147, 323] following a quantum quench, and even the absence of thermalization in the presence of disorder [3]. In nonequilibrium many-body systems, the phenomenon of prethermalization plays a peculiar role [38, 224, 260, 279]. Prethermalization describes a significant slowing down of the dynamics, where the system initially relaxes toward a quasisteady, long-lived state after a perturbation. The establishment of thermal equilibrium eventually occurs over a much longer timescale. In a prethermal state, the system retains a partial memory of its initial conditions, while showing a strong resemblance to its true thermal equilibrium state [27, 38, 75, 224, 246, 260, 261, 279, 358]. Experimentally, most studies of this phenomenon have been conducted in ultracold atomic gases: relaxation and prethermalization have been observed in one-dimensional (1D) Bose gases [155, 242, 243, 380], where the dynamical emergence of prethermal states arises because the system is close to integrability. Recently, signatures of prethermal states were also identified in unitary Bose gases [115].

In parallel, fluids of light in the propagating geometry [68] have emerged as a complementary platform to study two-dimensional (2D) Bose gases, with the observation of Bogoliubov-like dispersion [P4] [P14] [315, 400], signatures of photon condensation [346, 378] and spontaneous nucleation of vortices in a lattice [366]. This platform relies on the formal analogy between a laser field propagating through a nonlinear medium and the temporal evolution of a 2D quantum fluid. In this propagating geometry, the initial state can be engineered at will using wavefront shaping techniques, as illustrated by observations of dispersive shock waves [P3] [P13] [337, 415]. Moreover, upon entering the nonlinear medium, the beam experiences a sudden change of refractive index, which effectively reproduces the dynamics of a Bose gas after an interaction quench [27, 246]

[P1]. This makes it a natural system for exploring nonequilibrium physics.

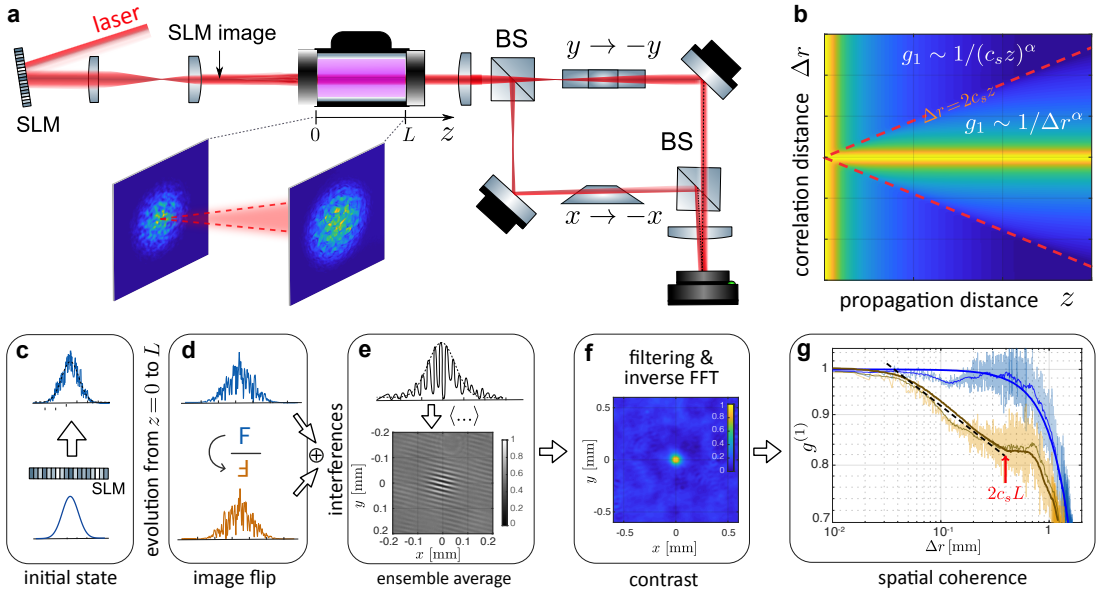

Figure 31. *Measurement of the coherence function demonstrating light-cone spreading of algebraic correlations in a 2D photon fluid. (a) Experimental setup. (b) Scenario of pre-thermalization in 2D. Upon propagation, the initial short-range speckle fluctuations are amplified and exhibit algebraic correlations associated with long-lived phononic excitations and spreading within a light cone of boundary $\Delta r = 2c_s L$. Out of the light cone, g_1 is independent of $\Delta \boldsymbol{r}$, reproducing the initial state long-range coherence. (c) The initial state is prepared using a SLM with a random phase mask superimposed on a Gaussian laser beam. This results in a weakly fluctuating field that propagates in a hot ^{87}Rb vapor cell of length L. (d) After propagation in the cell, the beam is split within a Mach-Zehnder interferometer and flipped using two Dove prisms. (e) The two inverted copies interfere and the fringe visibility is recorded. (f) The coherence function $g^{(1)}(\Delta \boldsymbol{r} = 2\boldsymbol{r}) = \langle \Psi^*(\boldsymbol{r}, L)\Psi(-\boldsymbol{r}, L)\rangle$ is obtained by computing the ensemble average of the measured contrast over 2000 realizations. (g) Experimental $g^{(1)}$ functions at $z = 0$ and $z = L$. Light colored data are raw signals, and thin solid curves their azimuthal average. Thick solid curves are the final measurements, obtained by subtracting laser background imperfections. The light cone position at $2c_s L$ is indicated by the red arrow. The dashed line is a guide emphasizing the algebraic decay. Figure from [P2].*

In this section, we study the dynamical emergence of a prethermal state in a nonequilibrium, 2D fluid of light after an interaction quench. We first present direct measurements of the fluid's first-order correlation function that reveal the spontaneous emergence of long-range algebraic correlations spreading within a light cone, a characteristic signature of prethermalization bearing strong similarities with 2D thermal superfluids [84, 152, 166, 278, 283, 313]. We then provide a detailed experimental characterization of the algebraic order and find an agreement with recent theoretical predictions [27]. Finally, by a controlled increase of the fluid fluctuations, we unveil a crossover from algebraic to short-range (exponential) correlations, analogous to the celebrated Kosterlitz-Thouless

transition observed at thermal equilibrium.

Experimentally, our fluid of light is created by letting propagate a laser beam through a 10 mm-long vapor cell of ^{87}Rb heated to a temperature of 150 °C. Effective photon-photon interactions are achieved by tuning the laser close to resonance (detuned by -1.5 ± 0.1 GHz) with respect to the $F = 2 \rightarrow F'$ transition of the D2-line at $\lambda_0 = 2\pi/k_0 =$ 780 nm, as described in [P4] [P10]. Under these conditions, the vapor is self defocusing, corresponding to repulsive photon-photon interactions. As proposed in [27], we carefully prepare an initial state consisting of weak random speckle field $\psi_s(\mathbf{r})$ superimposed on a more intense laser beam having a wide Gaussian profile (waist $w_0 = 1.8$ mm) and denoted $I_t(r) = I_0 \exp(-2r^2/w_0^2)$. The optical field impinging on the cell is of the form $\Psi(\mathbf{r}, z = 0) = \sqrt{I_t(r)}[1 + \epsilon\psi_s(\mathbf{r})]/\sqrt{1+\epsilon^2}$, where $\epsilon \ll 1$ is a dimensionless parameter quantifying the fluctuations and controlled via SLM patterns. The key idea here is that the background field, being close to a plane wave, is almost a stationary state of the problem. The weak speckle fluctuations thus mainly drive the thermalization process. For $\epsilon \ll 1$, however, the latter becomes slow and leaves room to a prethermal stage where the dynamics becomes governed by independent phonons of long lifetime [27]. Notice that the chosen initial state can be seen as the optical analogue of a 2D trapped Bose-Einstein condensate [of spatial profile $I_t(r)$ and condensate fraction $1/(1+\epsilon^2)$], on top of which small thermal fluctuations (here described by the random speckle) are present.

At the cell entrance, the photon fluid effectively experiences an interaction quench due to the nonlinear index change. The cell exit plane is imaged on a camera after propagating within a balanced Mach-Zehnder interferometer. The images of both arms are inverted with the help of two Dove prisms in a perpendicular configuration [97, 338], see Fig. 31(a). The coherence function, $g^{(1)}$, is obtained by Fourier filtering the interference contribution, and averaging the field at the cell exit $\Psi(\mathbf{r}, z = L)$ over 2000 speckle realizations:

$$g^{(1)}(\Delta\mathbf{r} = 2\mathbf{r}) = \langle \Psi^*(\mathbf{r}, L)\Psi(-\mathbf{r}, L)\rangle, \tag{28}$$

where $\langle \ldots \rangle$ refers to ensemble averaging [see Figs. 31(c-f)].

Typical $g^{(1)}$ measurements are presented in Fig. 31(g). We show the raw data (light curves) obtained for a given Δr, their azimuthal average performed by exploiting the statistical rotational invariance of $g^{(1)}$ and, finally, the data after background residual inhomogeneity correction in dark colors. While, at $z = 0$, the coherence function nearly coincides with the background profile $I_t(r)$ due to small initial fluctuations, at $z = L$ one observes a characteristic structure (within the background envelope) where $g^{(1)}$ first decays algebraically and then saturates at a constant value forming a plateau. A low-energy effective theory for the propagation of excitations in the vapor, assuming an homogeneous background laser, provides the dynamical scenario of 2D pre-thermalization sketched in Fig. 31(b) [27]. After a short propagation distance $z \sim 1/(2gI_0)$ after the quench, the initial weak speckle fluctuations are amplified, and a quasi long-range order emerges spontaneously within a light cone of radius $\Delta r \sim 2c_s z$, where $c_s = \sqrt{gI_0/k_0}$ is the speed of sound in the fluid. The position of the light cone can be calculated from the interaction constant g, measured independently with the method of [P10], and is shown with a red arrow on Fig. 31(g). Its position agrees with the observed onset of the $g^{(1)}$

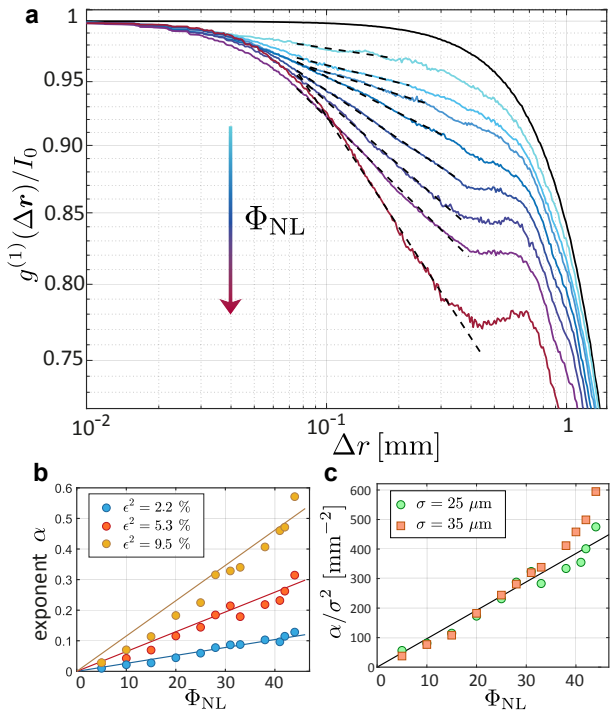

Figure 32. *Direct observation of the long-range algebraic order in a 2D pre-thermal state of light. (a) Normalized coherence function $g^{(1)}(\Delta \boldsymbol{r})/I_0$ vs Δr for increasing values of the nonlinear phase Φ_{NL}, at fixed $\sigma = 25\,\mu m$ and $\epsilon^2 = 2.2\%$. Notice the double logarithmic scale. Dashed curves are algebraic fits to $1/\Delta r^{\alpha}$ in the central region. (b) Extracted algebraic exponents α vs Φ_{NL}, for three fluctuation strengths (blue: $\epsilon^2 = 2.2\%$, red: $\epsilon^2 = 5.3\%$, yellow: $\epsilon^2 = 9.5\%$) (c) Algebraic exponent α/σ^2 at fixed $\epsilon^2 = 5.3\%$, for two different speckle correlation lengths σ (green circles: $\sigma = 25$ μm, red squares: $\sigma = 35$ μm). All data points fall on the same curve, confirming the scaling $\alpha \propto \sigma^2$. Solid curves are linear fits to Eq. (30). Figure from [P2].*

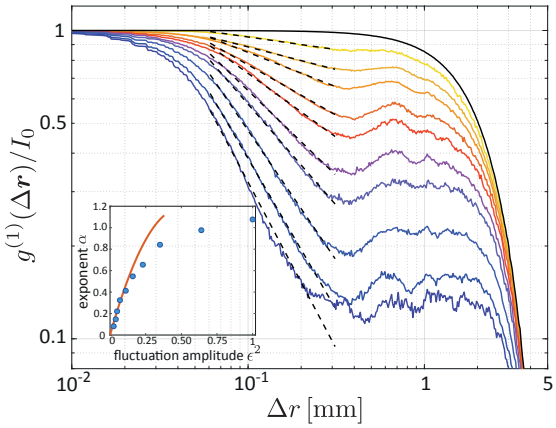

Figure 33. *Impact of the initial fluctuation amplitude ϵ on the pre-thermal state. Normalized coherence function $g^{(1)}(\Delta\mathbf{r})/I_0$ vs Δr for increasing values of the fluctuation amplitude ϵ ($\epsilon^2 = 0, 0.027, 0.04, 0.05, 0.07, 0.11, 0.16, 0.23, 0.35$ from top to bottom). Here $\sigma = 35\,\mu m$ and $\Phi_{NL} = 20$ rad. Dashed curves are algebraic fits to $1/\Delta r^\alpha$ in the central region. The inset shows the extracted algebraic exponents (blue dots), together with the prediction (30) [with no free parameters since we set the proportionality coefficient with that of Fig. 32]. Figure from [P2].*

plateau at a propagation length L.

The above observations fall in line with the common picture of prethermalization, where the short-time dynamics is governed by collisionless quasi-particles (here phonons) of long lifetime. To confirm this, following [27], we can show from a low-energy Bogoliubov approach that the post-quench dynamics starting from $\Psi(\mathbf{r}, z = 0)$ can indeed be described in terms of long-lived phonons, giving the following scaling laws for the coherence function at the cell exit plane when $\epsilon \ll 1$:

$$g^{(1)}(\Delta\mathbf{r}) \propto I_t(r) \begin{cases} (\xi/\Delta r)^\alpha & \text{for} \quad \Delta r < 2c_s L \\ \text{const} & \text{for} \quad \Delta r > 2c_s L, \end{cases} \tag{29}$$

where $\xi = 1/\sqrt{4k_0 g I_0}$ is the healing length. The algebraic exponent is given by

$$\alpha \propto \epsilon^2 \Phi_{\mathrm{NL}} \sigma^2, \tag{30}$$

where $\Phi_{\mathrm{NL}} = g I_0 L$ is the nonlinear phase accumulated by light upon propagating through the vapor and σ is the speckle correlation length. Eqs. (29) and (30) emphasize another property of the pre-thermal state: within the light cone, the fluid of light resembles a 2D superfluid at thermal equilibrium, characterized by a quasi long-range order [84, 152, 166, 278, 283, 313]. This is not a strict thermal equilibrium though, since the characteristic dependence of α differs from the one of a thermal superfluid, for which $\alpha \propto \epsilon^2/\sigma^2$ and varies weakly with the interaction.

To confirm the above scenario, we confront the experimental results to the prediction (30). We first show in Fig. 32(a) experimental coherence functions obtained for increasing values of the interaction $g \propto \Phi_{\mathrm{NL}}$ at fixed ϵ, σ. Algebraic exponents extracted from fits

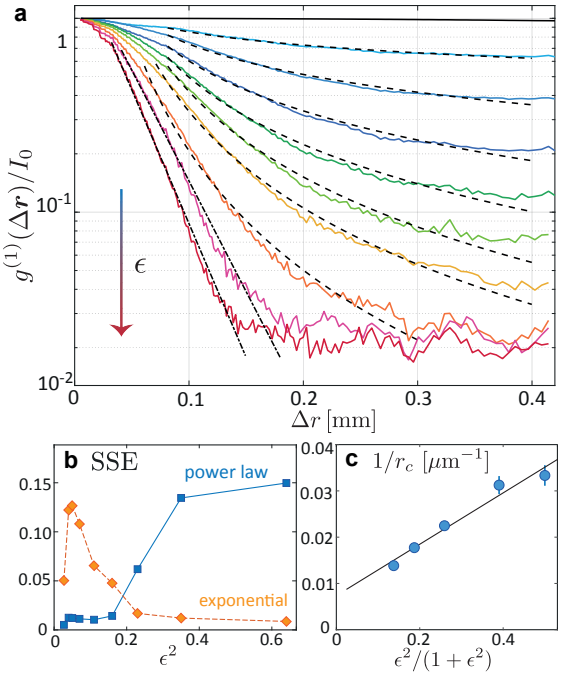

Figure 34. *Cross-over from algebraic to short-range (exponential) correlations at stronger fluctuation amplitudes, with the interaction strength set to a value $\Phi_{NL} = 44$ rad twice larger than in the previous data (notice the log scale). (a) Normalized coherence function $g^{(1)}(\Delta \boldsymbol{r})/I_0$ vs Δr when increasing more significantly ϵ ($\epsilon^2 = 0, 0.027, 0.04, 0.05, 0.07, 0.11, 0.16, 0.23, 0.35, 0.64$ from top to bottom). Here $\sigma = 35$ μm is fixed. (b) Sum-squared error between experimental data and exponential (orange) vs algebraic (blue) fit. For $\epsilon^2 > 0.35$ the exponential fit becomes more accurate than the algebraic fit. (c) Rate $1/r_c$ of the exponential decay, see Eq. (31), vs the fluctuation amplitude. The linear fit (black) confirms the theoretical scaling of Eq. (32). Figure from [P2].*

of $g^{(1)}(\Delta \mathbf{r})$ in the central region are shown in Fig. 32(b), and confirm the linear scaling of α with the interaction strength predicted by Eq. (30), at least for fluctuations ϵ^2 below 10%. The solid lines in Fig. 32(b) are linear fits to Eq. (30) and are used to set the proportionality coefficient of Eq. (30), such that there is no adjustable parameters for all other results presented in this work. A second set of measurements, using two different correlation lengths σ, is presented in Fig. 32(c). By normalizing the exponent $\alpha(\Phi_{\mathrm{NL}})$ to σ^2, we observe that $\alpha(\Phi_{\mathrm{NL}})/\sigma^2$ measured at different σ is independent of σ, which is again in agreement with the scaling law of Eq. (30).

Additionally, we investigated the behavior of $g^{(1)}$ with ϵ, setting $\sigma = 35\,\mu$m and the interaction strength $\Phi_{\mathrm{NL}} = 20$ rad to a relatively weak value. The results are reported in Fig. 33. We observe an increase of the algebraic exponent α with ϵ. A comparison of the extracted $\alpha(\epsilon)$ with Eq. (30) is shown in the inset. We find that the theory provides a good description of experimental results, as long as the initial fluctuations remain small, typically $\epsilon^2 \lesssim 0.25$. In fact, deviations at higher ϵ values should not come as a surprise,

since the characteristic algebraic, "low-energy" behavior (29) of the coherence function is expected to hold for $\epsilon \ll 1$ only. Indeed, in our 2D system the emergence of a pre-thermal state can be seen as a consequence of a weak breaking of translation invariance stemming from the initial speckle, a scenario for pre-thermalization put forward in [260].

To further characterize the non-equilibrium dynamics, we have studied the evolution of $g^{(1)}(\Delta\mathbf{r})$ up to larger values of ϵ, setting a stronger interaction strength $\Phi_{\mathrm{NL}} = 44$ rad. From the above discussion, one could naively expect that, upon increasing ϵ, the low-energy state (29) leaves room to a non-universal dynamics, where no pre-thermalization stage arises and where $g^{(1)}(\Delta\mathbf{r})$ has no specific structure. Instead, we have experimentally observed that the coherence function smoothly turns from algebraic to exponential as ϵ is increased:

$$g^{(1)}(\Delta\mathbf{r}) \sim \exp(-\Delta r/r_c). \tag{31}$$

The cross-over from Eq. (29) to this exponential behavior is presented in the measurements of Fig. 34(a). We have confirmed it by a computation of the sum of squared estimate of errors (SSE) that measures the discrepancy between the $g^{(1)}$ data and a fit to either Eq. (29) or (31), see Fig. 34(b). Note that such an exponential decay differs from the Gaussian correlations of the initial speckle and, in that, is associated with a genuine new dynamical regime emerging from the quench. Another statistical test, coefficient of determination R^2 confirms the transition at $\epsilon^2 \sim 0.2$. We also observed this cross-over in *ab initio* numerical simulations and found it to be a generic feature of $g^{(1)}$ in the pre-thermal regime as ϵ or Φ_{NL} are increased to moderate values. This phenomenon was also previously pointed out in [27]. At a physical level, this algebraic-to-exponential crossover is reminiscent of the celebrated Kosterlitz-Thouless (KT) transition, which drives 2D Bose gases at thermal equilibrium from a superfluid to a normal-fluid state when the temperature is raised. Although out-of-equilibrium, our fluid of light displays a similar behavior in the pre-thermal regime. This unexpected phenomenon can be understood by noticing that, at low ϵ and/or small interaction strength, the energy injected into the system during the quench is low, and so is the effective pre-thermalization "temperature". This results in an pre-thermal state with quasi long-range order, which can be seen as the dynamical counterpart of a 2D, equilibrium superfluid at low temperature. When ϵ and/or g is increased, on the other hand, one reaches pre-thermal states of effectively larger temperature. The resulting fluid displays exponentially-decaying correlations, analogous to the normal phase of a 2D Bose gas above the KT temperature. At the cross over between the two regimes, the exponent value is $\alpha = 1.7 \pm 0.1$, in strong contrast with a KT phase transition in thermal equilibrium homogeneous systems where the exponent is 0.25 [283].

To gain more insight on the pre-thermal regime of exponential correlations, we studied the dependence of the correlation length r_c of the exponential decay, see Eq. (31), on the initial fluctuation amplitude ϵ. To unveil this dependence, one can take advantage of total energy conservation $E_t = \int d\mathbf{r}(1/(2k)|\nabla\psi(\mathbf{r})|^2 + g/2|\psi(\mathbf{r})|^4)$ during the non-equilibrium evolution. Equating E_t to the normal state energy (31), we obtain:

$$\frac{1}{r_c} \propto \frac{\epsilon^2}{1+\epsilon^2} \tag{32}$$

We have also confirmed this law from extensive numerical simulations. Experimental values of $1/r_c$, extracted from our measurements of $g^{(1)}$, are shown in Fig. 34(c). When plotted vs $\epsilon^2/(1+\epsilon^2)$, they show a good agreement with the prediction (32).

Conclusion

In summary, our experimental description of a 2D fluid of light through a direct probe of its spatial coherence has revealed the dynamical emergence of algebraic prethermalization following an interaction quench. Unlike previous studies involving near-integrable systems in 1D, prethermalization emerges as a result of the weak breaking of translation invariance after the quench. Our results further point toward the existence of a crossover from algebraic to exponential correlations in the prethermal regime of 2D systems, an intriguing phenomenon that we interpret as a nonequilibrium precursor of the thermodynamic KT transition. This effect opens exciting perspectives for further studies of nonequilibrium quantum fluids. While a comprehensive description of 2D thermalization processes remains open, our analysis emphasizes the assets of photon fluids for probing the dynamics of far-from-equilibrium many-body systems.

3.3.2. Analogue cosmological particle creation in an ultracold quantum fluid of light [P1]

Abstract: The rapid expansion of the early universe resulted in the spontaneous production of cosmological particles from vacuum fluctuations, some of which are observable today in the cosmic microwave background anisotropy. The analogue of cosmological particle creation in a quantum fluid was proposed, but the quantum, spontaneous effect due to vacuum fluctuations has not yet been observed. Here we report the spontaneous creation of analogue cosmological particles in the laboratory, using a quenched 3-dimensional quantum fluid of light. We observe acoustic peaks in the density power spectrum, in close quantitative agreement with the quantum-field theoretical prediction. We find that the long-wavelength particles provide a window to early times. This work introduces the quantum fluid of light, as cold as an atomic Bose-Einstein condensate.

Introduction

The expansion of a universe stretches all length scales, including the wavelengths of the particle modes. Thus, the frequencies of the modes evolve with time [355], which implies that the modes at early and late times are related by a Bogoliubov transformation [64, 156, 281, 307, 308]. This field theory approach avoids the microscopic details, and predicts the spontaneous production of cosmological particles, including the primordial density fluctuations which led to the acoustic peaks in the cosmic microwave background (CMB) spectrum [64, 156, 309]. It is particularly relevant since the acoustic peaks can be described by linear perturbation theory [179].

The field theory approach inspired the subject of analogue cosmological particle creation, in which laboratory experiments mimic the dynamics of scalar fields in curved space times [23, 24, 127, 134, 191, 320, 407]. The experiments even allow for measurement over time, which is impossible in the real universe, for which there is only one time of observation. Since the model is independent of the microscopic description of the medium, various quantum fluids were proposed for the study of cosmological particle creation in analogue universes [23, 24, 127, 134, 191, 320, 407]. In a two-dimensional atomic Bose-Einstein condensate, a qualitative comparison with cosmological particle creation was reported[184]. In a 1-dimensional experiment not related to quantum fluids, a rapid switch in the trapping field of two ions led to phonon pair creation and formation of spatial entanglement [412].

Analogue cosmological particle creation is a type of dynamical Casimir effect [107, 140, 277], which was observed in a superconducting circuit [411] and an optical fiber [395]. The classical, stimulated version of the effect was reported in a Bose-Einstein condensate [192], but the observation of the quantum effect in a quantum fluid has not been reported. Pairs can also be produced by a modulational instability [73].

We simulate expanding and contracting universes in a 3-dimensional quantum fluid of light, as coherent as an atomic Bose-Einstein condensate, and we observe time-resolved analogue cosmological particle creation out of vacuum fluctuations. Our quantum fluid is a near-resonant laser pulse traversing a warm atomic vapor cell, as illustrated in Fig. 35a. Within the vapor cell, the repulsive interactions between photons are mediated by the atoms, due to Kerr nonlinearity induced by the atomic resonance [P4]. The interactions are suddenly quenched to zero when the laser beam exits the vapor cell [245]. This configuration mimics an expanding universe, since a rapid reduction of the interactions causes a sudden red shift of the energy spectrum [23, 24, 127, 191, 407]. We also observe the reverse process at the cell entrance, in which the interaction suddenly appears, mimicking a contracting universe. We demonstrate that both processes produce pairs of analogue cosmological particles, which confirms the predictions of Ref. [245].

Results

Theoretical techniques. Our approach relies on the analogy between light propagation in a Kerr nonlinear medium, and the temporal dynamic of an atomic Bose-Einstein condensate. The effective time is $\tau = z/c$, where z is the position in the direction of propagation, and c is the speed of light. This effective time is equivalent to true time for the sake of quantum mechanical quasiparticle creation [239, 245]. With no approximation other than the usual paraxial and slowly-varying envelope approximations [66], we extend the standard monochromatic limit [66] and find that our fluid is described by the 3-dimensional Gross-Pitaevskii equation

$$i\hbar\frac{\partial\psi}{\partial\tau} = -\frac{\hbar^2}{2m}\nabla^2\psi + U(\mathbf{r},\tau)\psi + g(\mathbf{r},\tau)\left|\psi\right|^2\psi \tag{33}$$

where ψ is the slowly-varying envelope of the electric field, $|\psi|^2$ is the volume density of

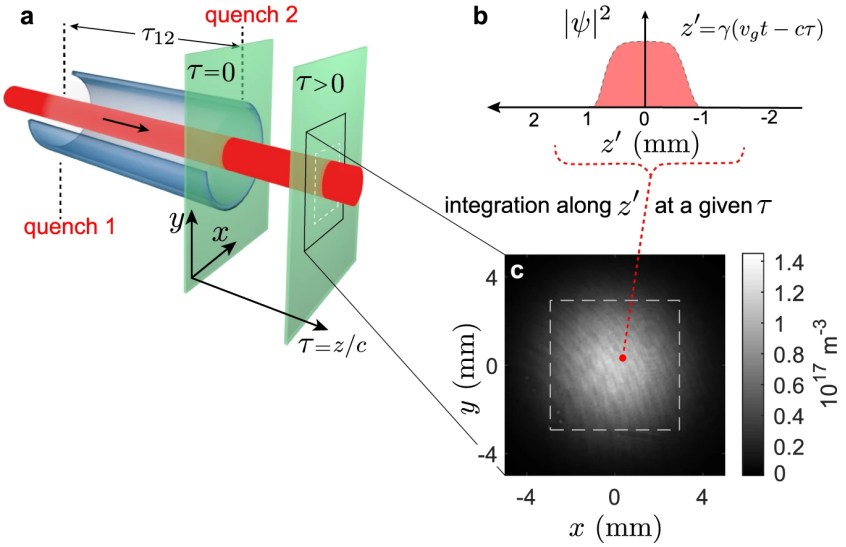

Figure 35. ***The analogue universe.*** ***a*** *The fluid of light (red) is a laser pulse traversing a heated* ^{85}*Rb vapor cell. The axial position gives the effective time* τ*. The quenches occur at the entrance and exit of the vapor cell.* $\tau = 0$ *corresponds to quench 2. The time between the two quenches is* τ_{12}*.* ***b*** *The true time gives an effective third spatial dimension* z'*.* ***c*** *Typical image of the fluid of light integrated along* z'*, given in units of photon density. An effective time* $\tau = 130\,ps$ *after quench 2 is shown. Figure from [P1].*

the photons, m is their effective mass, U is an external potential, and $g\,|\psi|^2$ is the mean-field interaction energy. The three spatial dimensions of ∇ correspond to the transverse coordinates (x, y) and to $z' = \gamma\,(v_g t - c\tau)$, which is a coordinate comoving with the laser pulse at the group velocity v_g, and compressed by the factor $\gamma = \left(-v_g^2 k_0 D_0\right)^{-1/2}$, where k_0 is the wavenumber of the laser, and D_0 is the group velocity dispersion. In other words, a laser pulse viewed in the z' coordinate would appear stationary and compressed relative to its length in the z coordinate.

We study the analogue cosmological particles using the static structure factor, in analogy with the CMB power spectrum. The static structure factor has been used to study density fluctuations in Bose-Einstein condensates [184, 352], and we apply this technique to a fluid of light. It is given by $S(k_x, k_y, k_{z'}) = \langle|\delta\rho(k_x, k_y, k_{z'})|^2\rangle/M$, where $\delta\rho(k_x, k_y, k_{z'})$ is the spatial Fourier transform of the density fluctuation at time τ, and M is the total number of particles in the fluid. With this definition, a zero-temperature, non-interacting gas has $S(k) = 1$, reflecting the presence of spatial shot noise. The operator $\hat{b}^\dagger_{\mathbf{k}}$ corresponds to the creation of a quasiparticle after the quench, in mode $\mathbf{k} = (k_x, k_y, k_{z'})$ oscillating at frequency ω_k. In the presence of quasiparticle populations $N \equiv \langle\hat{b}^\dagger_{\mathbf{k}}\hat{b}_{\mathbf{k}}\rangle$ and correlations $C \equiv \langle\hat{b}_{\mathbf{k}}\hat{b}_{-\mathbf{k}}\rangle$, the static structure factor within the Bogoliubov approximation is given by

$$S(k) = 1 + 2N + 2\,\mathrm{Re}\left(Ce^{-2i\omega_k\tau}\right)\,. \tag{34}$$

The populations and correlations are given by

$$N = \beta^2 + N_0\left(\alpha^2 + \beta^2\right) + 2\alpha\beta\,\mathrm{Re}\left(C_0\right) \tag{35}$$

$$C = \alpha\beta + C_0\alpha^2 + C_0^\star\beta^2 + 2\alpha\beta N_0 \tag{36}$$

where $N_0 \equiv \langle \hat{a}_{\mathbf{k}}^\dagger \hat{a}_{\mathbf{k}} \rangle$ and $C_0 \equiv \langle \hat{a}_{\mathbf{k}} \hat{a}_{-\mathbf{k}} \rangle$ are the populations and correlations before the quench, respectively, $\hat{a}_{\mathbf{k}}^\dagger$ corresponds to the creation of a quasiparticle before the quench, and the operators are related by the Bogoliubov transformation $\hat{b}_{\mathbf{k}} = \alpha\hat{a}_{\mathbf{k}} + \beta\hat{a}_{-\mathbf{k}}^\dagger$. For our series of two quenches, Eqs. (35) and (36) are applied twice. Since each quench either starts or ends with no interactions, α and β are the same Bogoliubov coefficients which diagonalize the Hamiltonian of a weakly-interacting quantum fluid. In the absence of quasiparticles before a given quench, the pair production is spontaneous, and Eqs. (35) and (36) become $N = \beta^2$ and $C = \alpha\beta$. On the other hand, a distribution of quasiparticles before the quench, thermal or otherwise, will stimulate additional pairs.

Experimental design. To create the fluid of light, we use a laser pulse with a 4 mm Gaussian waist and a power of 100 mW, propagating in an ^{85}Rb vapor cell heated to 150 °C. A pulse length of 100 ns is employed to avoid saturating the camera used for observation. The laser is detuned −1.5 GHz (90 natural linewidths, 6 times the Doppler broadening) from the D2 $5S_{1/2}$, $F = 3 \rightarrow 5P_{3/2}$ transition, giving $v_g = 0.007c$. The interaction energy and healing length $\xi = 60\,\mu$m are determined by the nonlinear change in the refractive index Δn, which is computed from the experimental parameters. By taking into account the compression factor γ, this configuration leads to a weakly interacting photon gas with a thickness of 2 mm in the z' coordinate, and a dimensionless interaction coefficient $\rho a_s^3 = 7\,10^{-14}$, where ρ is the average photon density, and a_s is the effective scattering length.

The fluid of light is imaged on a sCMOS camera, as shown in Fig. 35c. We tune the imaging system to pick out a certain z after the cell (fixing the effective time τ after the second quench), and the camera integrates over true time (thus integrating over z'), as illustrated in Fig. 35b. According to the Fourier slice theorem, this integration in position space gives a slice in k-space [50]. Thus, an ensemble of 200 images is obtained for each τ, and the power spectrum $S(k_x, k_y, k_{z'} = 0)$ is computed by 2-dimensional Fourier transforms within the dashed square shown in Fig. 35c. The computation partially removes the effects of any drifts such as thermal convection, and accounts for the measured quantum efficiency of the camera.

Observation of analogue cosmological particle creation. In Fig. 36a we observe ring patterns in $S(k_x, k_y, k_{z'} = 0)$, oscillating as a function of k. These oscillations are the experimental signature of analogue cosmological particle creation, in close analogy with the acoustic peaks in the angular spectrum of the CMB. Pairs of quasiparticles with momenta $\pm\mathbf{k}$ are generated at the moment of the quench with a random overall phase, but a definite phase relationship between $+\mathbf{k}$ and $-\mathbf{k}$, and oscillate with various frequencies ω_k. Only certain k-values interfere constructively at the observation time τ,

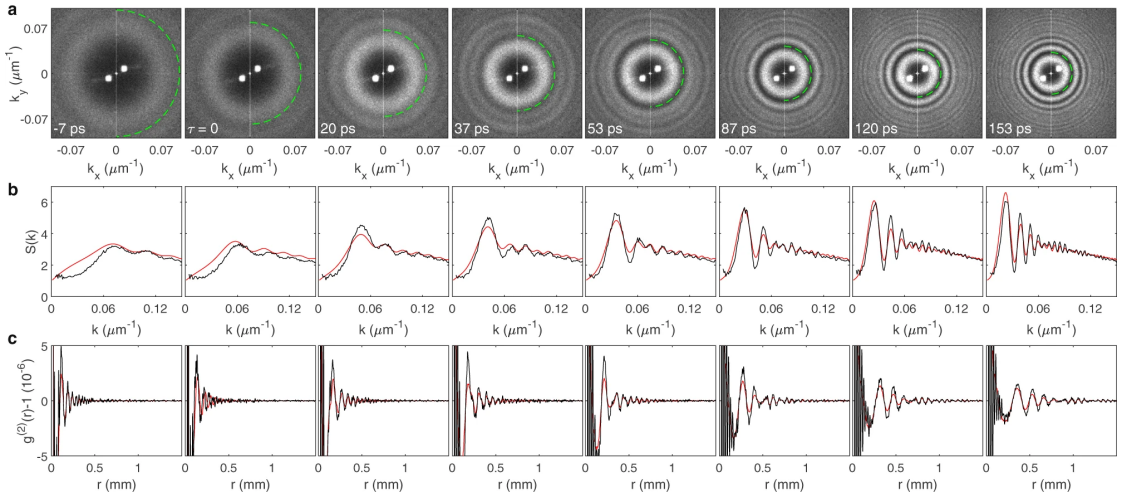

Figure 36. ***Analogue cosmological particle creation in a quantum fluid of light.*** ***a*** *The static structure factor $S(k_x, k_y, k_{z'} = 0)$ at various times after the second quench. The dashed green curves indicate the first minimum of the red curves in (b). The symmetric white points near the center of all panels are due to spurious fringes in the imaging system.* ***b*** *Radial profiles of (a). The black curves are the experimental data. The red curves are the prediction for analogue cosmological particle creation, from Eq. (34).* ***c*** *Density-density correlations. The experimental (black) and theoretical (red) curves are obtained from b by the spherical Fourier transform of Eq. (37). Figure from [P1].*

resulting in a ring pattern. The rings shrink with τ since lower frequencies take longer to develop oscillations. The shrinking pattern of rings is described quantitatively by Eq. (34). The radius of the first minimum in Fig. 36a is seen to be in good agreement with the theoretical prediction of Eq. (34), indicated by the dashed green curve. The azimuthal averages $S(k)$ of $S(k_x, k_y, k_{z'} = 0)$ are indicated in black in Fig. 36b. The red curves are calculated from Eq. (34), taking into account the two quenches, and the variations in α, β, and ω_k which result from the measured absorption. Very good agreement between the experimental black and theoretical red curves is seen.

We also determine the spatial density correlations produced by the analogue cosmological particle creation. We derive the density-density correlation function $g^{(2)}(r)$ from $S(k)$ by the 3-dimensional spherically-symmetric Fourier transform

$$g^{(2)}(r) - 1 = \frac{1}{2\pi^2 \rho} \int \mathrm{d}k\, k^2\, \frac{\sin(kr)}{kr}\, [S(k) - 1] \ . \tag{37}$$

Figure 36c shows $g^{(2)}(r) - 1$, found by applying Eq. (37) to Fig. 36b. The oscillations are spherical shells propagating outward. The correlations are seen to reach increasing distances as time increases. They are on the order of 10^{-6}, which implies that the relative density fluctuations are on the order of 10^{-3}. The oscillations are clear despite the small signal, due to the high sensitivity of the optical detection. The theoretical red curves are obtained by applying Eq. (37) to Eq. (34), and quantitative agreement with the experimental curves is seen.

Spontaneous particle creation in the first quench. The low-k behavior of $S(k)$ provides a window into the early times before the quenches, since the frequency of these modes approaches zero, so the modes do not have sufficient time to evolve during the experiment. The first peak in $S(k)$ corresponds to the frequency $1/(4\tau)$, the lowest frequency which has time to oscillate. Well below this k-value, Eq. (2) reduces to $S(k) = 1 + 2N_1$, where N_1 is the incoherent population before the first quench, and the unity term corresponds to the quantum shot noise, which is scale invariant (independent of k). Thus, the value of $S(k)$ gives a direct measure of N_1. Figure 37a shows the $S(k)$ curves for all τ plotted together. We observe that $S(k)$ is at most 1.4 for low k, as indicated by the dashed green line, giving $N_1 \leq 0.2$. This value is finite and approximately scale invariant, which implies a negligible thermal component, since a thermal population diverges like $1/k$. Furthermore, it is less than unity, implying that the spontaneous contribution dominates. Thus, the analogue cosmological particle creation is spontaneous in the first quench. This is verified by the blue and green curves in Fig. 37c, which show that stimulation in the first quench by thermal noise and white noise, respectively, would produce larger values of $S(k)$ than those of the experiment, for low k.

Stimulated particle creation in the second quench. The quasiparticles spontaneously created during the first quench stimulate pair creation in the second quench. However, if the particle production in the second quench were stimulated by the first-quench quasiparticles only, $S(k)$ would oscillate about unity, as indicated by the magenta curve in Fig. 37d. Rather, $S(k)$ features an upward shift relative to unity, and a downward slope for large k. The downward slope is due to the finite resolution of the imaging system, measured to be $10\,\mu$m, and is included in the theoretical curves. The upward shift results from absorption and spontaneous reemission of photons from the atomic medium. By the first two terms of Eq. (34), $S(k)$ oscillates about the value $1 + 2\,(N_1 + N_b)$, where N_b is the background population present in the fluid between the two quenches. The population spontaneously created in the first quench does not contribute to this expression, since its spectrum (given by β^2 in Eq. (35)) does not extend to large k. The upward shift in Fig. 37a suggests $N_b = 1.2$, a value which agrees well with our estimate for spontaneous reemission. The theoretical curves in Fig. 36b include this additional stimulation. While this incoherent, flat spectrum of 1.2 quasiparticles per mode implies that the fluid is not in its ground state, like a finite-temperature Bose-Einstein condensate, it does not negate the oscillatory behavior of $S(k)$, and it even enhances the visibility of the oscillations. We can control this population by tuning the atomic density, the pulse duration, intensity, and detuning. In Fig. 37e we verify that this population vanishes for long weak pulses as expected, due to the finite coherence time of the spontaneous reemission. The unity value of $S(k)$ confirms that the fluid is shot-noise limited, when the effect of the atomic medium is absent.

Although our fluid of light is not in thermal equilibrium between the two quenches, we can put an upper limit on the effective temperature of the thermal component before the second quench. The blue curve in Fig. 37d includes thermal stimulation with an effective temperature $2mc_s^2 = 30\,\mathrm{mK}$, where c_s is the speed of sound for the Bogoliubov

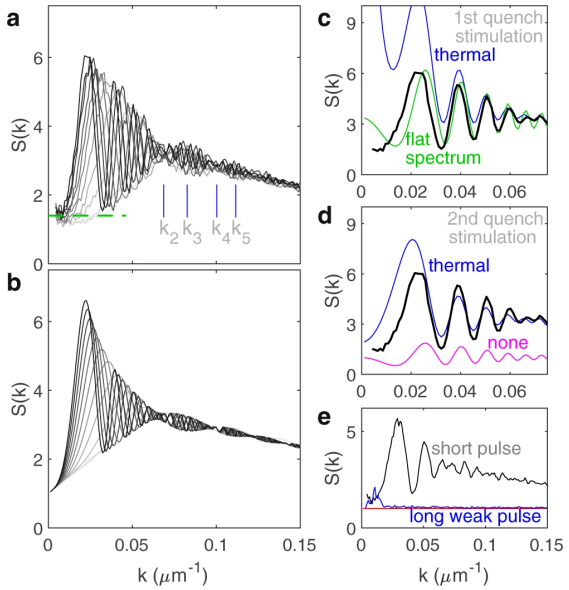

Figure 37. ***Spontaneous and stimulated cosmological particle production.*** ***a*** *The envelope of $S(k)$. The black curves of Fig. 36b are among the curves shown. Darker gray indicates later time. The low-k limit is indicated by the green dashed line. The k_p mark the nodes and antinodes.* ***b*** *The envelope of the theoretical curves.* ***c*** *The effect of stimulation in the first quench, on $S(k)$ after both quenches. The blue curve includes additional stimulation by a thermal distribution in the first quench. The green curve includes stimulation by a flat distribution in the first quench rather than the second. $\tau = 153\,ps$ is shown.* ***d*** *The effect of stimulation in the second quench. The blue curve includes additional stimulation by a thermal distribution in the second quench. The magenta curve includes no extra stimulation in either quench. $\tau = 153\,ps$ is shown.* ***e*** *Effect of the interactions. The black curve is from Fig. 36b. The blue curve employs a pulse which is 500 times weaker and longer. The red curve is the theoretical prediction for the long, weak pulse. $\tau = 87\,ps$ is shown. Figure from [P1].*

quasiparticles, which results in a greatly enhanced first peak. Since this enhanced peak is absent from the experimental curve, we estimate the effective temperature of the thermal component to be less than $2mc_s^2$, as in an atomic Bose-Einstein condensate. For the second quench, the thermal component does not diverge like $1/k$ since the zero-temperature static structure factor in the fluid of light goes to zero for low k (Ref. [315]).

Interference pattern and the dispersion relation. Figure 37a exhibits a beating pattern in the envelope of the various curves, resulting from interference between analogue cosmological particles created in the two quenches. The theoretical curves in Fig. 37b show a similar pattern. The envelope has nodes and antinodes at $\omega_{12\,k_p} = \pi p/(2\tau_{12})$, where p is an integer. By identifying each k_p as shown in Figs. 37a, 4 points on the dispersion relation are found, as indicated by blue points in Fig. 38a. These points agree well with the dispersion relation in the medium, calculated from the interactions, and

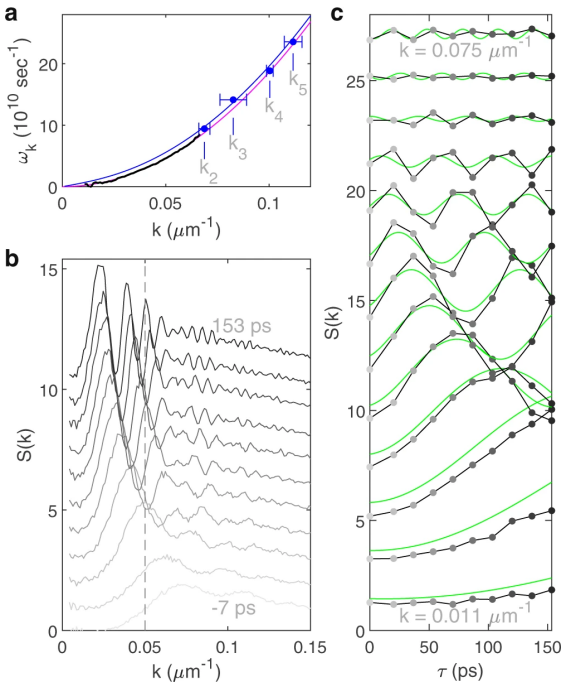

Figure 38. ***Individual modes of the analogue cosmological particles.*** ***a*** *The dispersion relation. The blue points are derived from the k_p in Fig. 37a. The error bars indicate one standard deviation. The black curve is obtained by sinusoidal fits to the gray curves in (c). The magenta curve is the free-particle dispersion relation. The blue curve is the dispersion relation in the interacting fluid of light.* ***b*** *The static structure factor at various times. The curves are from Fig. 37a, and are shifted vertically. The vertical dashed line is used to find the values in (c).* ***c*** *Each curve shows the τ-dependence of a definite k, given by the values along a vertical line in b, such as the dashed line. The grayscale is the same as in (b). The k-values shown are equally spaced by $5.4\,10^{-3}\,\mu m^{-1}$. The green curves are computed with Eq. (34). Each pair of black and green curves has been shifted vertically. Figure from [P1].*

indicated by the blue curve.

Individual modes. Figure 38b shows the curves of Fig. 37a, one above the other. By plotting the $S(k)$ values along the dashed line, we obtain the time dependence of a given mode k, as shown in Fig. 38c. Each mode is seen to oscillate sinusoidally after the second quench, with no visible damping. The frequencies of the oscillations, indicated by the black curve in Fig. 38a, agree well with the free-particle spectrum, which is relevant after the second quench.

Comparison with the CMB power spectrum. We compare and contrast our observed spectra with the CMB power spectrum in Fig. 39. Since 1990, several successive space missions have improved the resolution of the CMB measurements [4, 36, 294, 369], and Fig. 39b shows the latest results [4]. In the CMB spectrum, the oscillations occur as

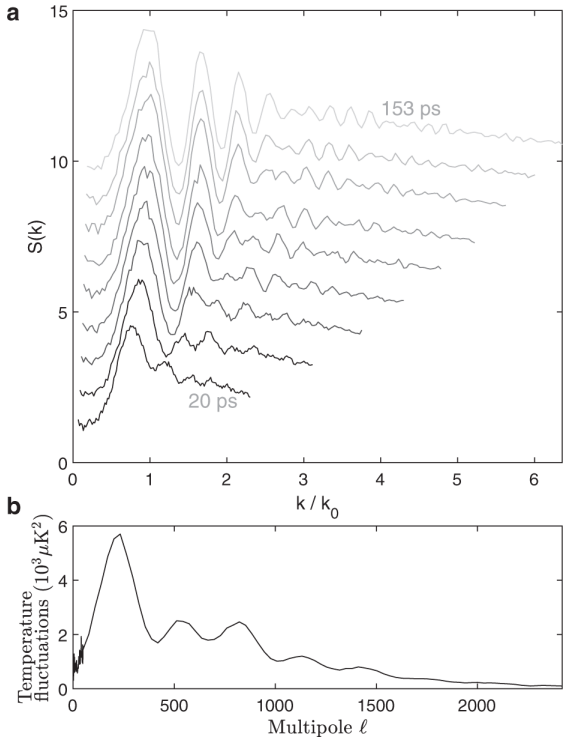

Figure 39. ***Comparing the measured power spectrum with that of the CMB. a*** *The static structure factor for $\tau > 0$. The wavenumbers are normalized such that unity can be compared with the first peak of the CMB spectrum in (b).* ***b*** *The power spectrum of temperature fluctuations in the CMB, as a function of multipole number, from Ref. [6]. Figure from [P1].*

a result of the well-defined phase between the cosmological particles [6, 311], which is also true for our spectra. In the early universe, the density fluctuations relevant for the acoustic peaks oscillated until the effective time of observation τ, when the photons decoupled from matter [57]. The mode number ℓ shown in Fig. 39b is proportional to k, when mapped back to the density fluctuations in the early universe, and the first peak likely corresponds to $\omega_k \tau \approx \pi$ (Refs. [180–182]). In contrast, the Bogoliubov transformation predicts a first peak in the CMB spectrum at $\omega_k \tau \approx \pi/2$ (Ref. [281]). Figure 39a shows our spectra for $\tau > 0$. For visual comparison with the CMB spectrum, k is divided by k_0, which satisfies $\omega_{k_0} \tau = \pi/2$, where ω_k is the magenta curve of Fig. 38a. There are features which are common to our spectra and that of the CMB, in addition to the oscillations: the decay of the oscillations for large k or ℓ and the approximately scale-invariant region for small k or ℓ. The oscillations in the CMB spectrum decay for large ℓ due to damping by photon diffusion [180]. In contrast, the oscillations in our spectra decay because the β Bogoliubov coefficient in Eq. (36) decreases for high k. The scale-invariant region of the CMB spectrum arises from quantum fluctuations [25, 163, 171], assuming that the inflation model is correct [162, 252, 349, 373]. Similarly, the scale invariant part of our spectra reflects the quantum nature of the particle production, as a result of the vacuum

of incoming particles. However, our incoming vacuum is a property of our shot-noise limited laser, as opposed to red-shifting of the modes which possibly occurred during inflation [7, 25, 190]. Red-shifting was observed in the laboratory [113], and it would be interesting to combine it with analogue cosmological particle production.

Discussion

This work establishes the paraxial fluid of light as a quantum fluid. The results demonstrate that quantum field theory applies to a system in which a spatial coordinate plays the role of time. The effective temperature is less than twice the interaction energy, which is comparable to many atomic Bose-Einstein condensates. On the other hand, the apparatus is an order of magnitude simpler, smaller, and less expensive. The direct detection of the photon fluid is also an advantage.

In conclusion, we observe both spontaneous and stimulated analogue cosmological particle creation in a quantum fluid of light. The particle production in the first quench is seen to be spontaneous, while the second includes stimulation by the first quench quasiparticles, as well as by an incoherent background. We quantitatively confirm the quantum field-theoretical prediction. The long wavelength part of the spectrum provides a window into early times before the particle creation. From an alternative perspective, we observe the spontaneous and stimulated dynamical Casimir effects in a quantum fluid.

Here, we skip a "Methods" section detailing all elements necessary to allow interpretation and replication of the results.

4. Conclusion and future directions

4.1. Context

After spending eight years exploring quantum fluids of matter or light, I am now interested in investigating the new frontier of quantum fluids of light in which photons are strongly interacting. Towards this goal and given my expertise in atomic physics, I was naturally drown to using Rydberg atoms to enhance photon-photon interactions by several orders of magnitude. After writing a successful CNRS research project on this topic, I started working as a CNRS researcher in October 2021 in the Exotic Quantum Matter group lead by Shannon Whitlock. Working in this team allows me to benefit from their long standing experience in atomic quantum gases excited to Rydberg states. In the following, I discuss about the evolution and the new trends of the field of quantum fluids of light and then present two research directions I started investigating in Strasbourg. This research is being pursued on the experimental setup of potassium atoms of the Exotic Quantum Matter group in parallel to the other research activities of the team. I successfully obtained two research grants to support my new research line: an ANR JCJC on "Strongly interacting quantum fluids of light in propagating geometries" and an ITI QMat grant of the University of Strasbourg on "Scalable cavity quantum electrodynamics without cavities" which allowed me to hire two PhD students to work on these topics and buy some specific research equipment to complement the existing experimental setup.

In addition to the research line I am leading, I am also involved in the other research activities of the team which includes quantum many-body physics with Rydberg atoms and the new direction recently initiated by Shannon Whitlock about digital quantum computing on atomic platforms. Within this framework, I participate to two academic research projects MSCA Doctoral Networks on "Machine Learning for Quantum" and on "Quantum and Classical Ultrasoft Matter" and to a SATT Conectus prematuration project about "Qubit control module for scalable atomic quantum processors".

4.2. Evolution of the field

Quantum simulation with photons

Quantum simulation and computation are two important research tools based on the laws of quantum mechanics to explore and understand the complexity of the quantum world. Besides its importance for fundamental academic research, it also has the potential to become a world-wide technology with important applications to accelerate the investigation of societal and industrial problems like pharmaceutical chemistry, genome sequencing, network grid optimization, stock market, etc. Quantum simulators are special purpose devices designed to provide insight about specific quantum problems. They are simpler to implement and potentially more noise tolerant than generally programmable "digital" quantum computers, which would be capable of solving a wider class of quantum problems. Quantum simulations are now daily running in research laboratories on a great variety of experimental platforms [385] ranging from superconducting qubits [178] to

ultracold atoms [48], arrays of single atoms trapped in optical tweezers [61], photons [19], nuclear magnetic resonance systems [326] or trapped ions [47]. For more than twenty years, quantum simulation has pushed the frontier of our understanding of many-body quantum systems by reaching several milestones like the observation of the MOT-to-superfluid transition in optical lattices [152], many-body localization [78, 368], quantum many-body spin systems [291, 331], dipolar supersolids [80] or topological bands [303].

Photons, massless and non-interacting particles in vacuum, are considered an extremely promising candidate for quantum simulation as they feature several key advantages like the ease of creation, manipulation and detection, the relatively low hardware requirements, the possibility to generate initial states with complex multi-photon entanglement, their mobility (high speed, low-loss transmission) and the intrinsic scalable processing via light-matter interaction. While weak photonic nonlinearities are currently a major drawback to overcome for a practical implementation of photonic quantum simulation, the recent progress of quantum optics now enable the creation of photon-photon interactions at the individual particle level using either strongly coupled atom-cavity systems [44, 220, 236], quantum nonlinear optics using atomic ensembles [135, 168] or quantum nonlinear optics through atom-atom interactions [255, 275]. Beyond their applications for few-photon all-optical quantum devices, strong photon-photon interactions have been used to create few-body strongly correlated states of light including molecules made of two or three photons [133, 251], a two photon Laughlin state of light [85], an 8-site photonic Mott insulator [257] and a 7 site strongly correlated fluid of light [350]. Yet, bringing photonic quantum simulation to systems containing a large number of particles is both a major challenge and an exciting frontier of the field as this would enable the creation of scalable photonic quantum simulators and the development of detection and characterization methods for many-body quantum states of light.

The ambition of the research line I am currently pursuing in Strasbourg is to extend the scope of photonic quantum simulation from the few-body regime to the many-body regime for which the outcome of the simulation cannot be simulated on classical computers. Towards this goal, fully leveraging on my past experience and that of the Exotic Quantum Matter team, I will follow two original routes by exploring on a cold atom Rydberg setup

- Strongly-interacting quantum fluids of light in propagating geometries
- Arrays of strongly coupled atom-cavity systems.

Quantum simulation with quantum fluids of light

As illustrated in figure 40, quantum fluids of light can be classified with a simple diagram [71] where two important parameters are at play : the strength of photon-photon interactions and the number of photons. On the one hand, optical nonlinearities at the single photon level in a blockaded single photonic mode were created using Rydberg electromagnetic induced transparency (EIT) [65, 71, 133, 196, 314] and paves the way towards all-optical quantum technologies (optical switches, photon transistors, photonic quantum gates, etc). On the other hand, weakly interacting photon gases have been

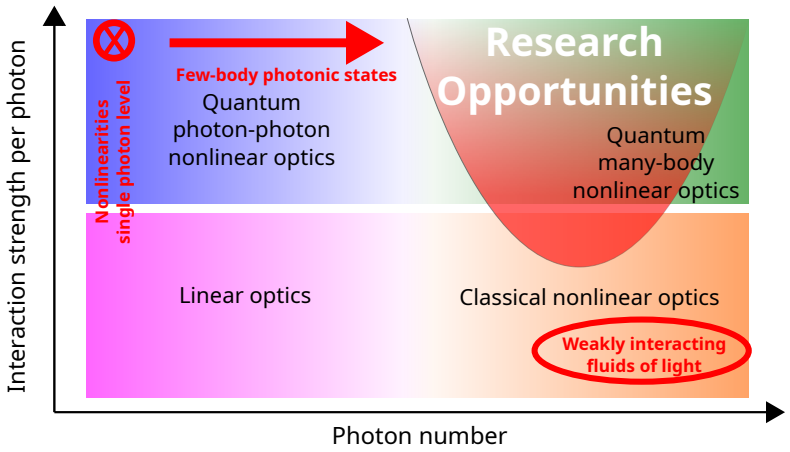

Figure 40. ***This diagram from [71] illustrates the different regimes of nonlinear optical phenomena.*** *"Weakly interacting fluids of light" represent the polariton [67, 68] or the hot atomic vapor platforms [P4] [P3]. "Optical nonlinearities at single photon level" paves the way to all-optical quantum technologies [65, 71, 133, 314]. "Few-body photonic states" were recently observed: molecules made of photons [133, 251], Laughlin states made of light [85], a 8-site photonic Mott insulator [257] and a 7 site strongly correlated fluids of light [350].*

studied: they consists of a lot of photons per mode (high laser intensities are used) with weak photon-photon interactions. For such systems, mean field equations (e.g. the nonlinear Schrödinger equation) are relevant to describe the system dynamics. This regime corresponds to the historical platforms for quantum fluids of light in polariton micro-cavities [67, 68] or quantum fluids of light in propagating geometries (see e.g. [P4] [P3]). The new frontier is now to explore regimes where the optical non-linearities are so important that photons are strongly interacting particles and the fluid develops strong quantum correlations. Very recently, building upon the realization of optical nonlinearities at the single photon level, an important experimental breakthrough led to the observation of few-body photonic states [85, 251]. Yet, these states were limited to few particles or few spatial modes: molecules made of photons [133, 251] and Laughlin states made of light [85]. This progress paves the way towards the realization of quantum simulation with strongly correlated fluids of light made of many photons (many optical modes) in settings where we have a good control over the parameters of the system (external potential and strength of the interactions) and easy and efficient access to relevant observables to characterize the quantum correlations of the system. Note that an early experimental implementation of a weakly-interacting photon gas based on Rydberg EIT has been recently reported [212].

Quantum simulation with strongly coupled atom-cavity systems

Engineering controllable, strongly interacting many-body quantum systems is a key requirement for quantum simulation and quantum information processing. In this

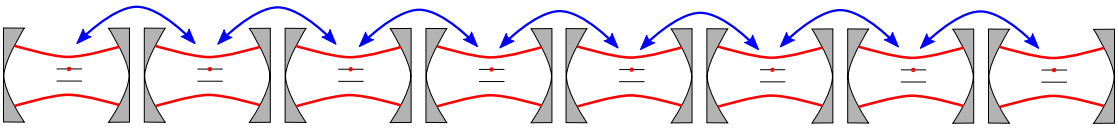

Figure 41. ***Series of coupled CQED systems which enables to simulate Jaynes-Cumming-Hubbard like models.***

context, cavity quantum electrodynamics (CQED), for which the interaction between light confined in a cavity and atoms under the conditions where the quantum nature of light is significant, is a powerful platform for controlling quantum systems. While CQED was initially developed with macroscopic high-Q cavities and atoms [44, 220, 236], alternatives based on solid state technologies have emerged: NV centers [123, 170] or quantum dots [141, 270, 310] coupled to nano-fabricated cavities, and circuit QED where the photon is stored in a one-dimensional on-chip resonator and the quantum object is an artificial atom [403]. All these platforms offer prominent advantages towards applications in quantum information processing and are excellent candidates for future quantum computation. However these applications are often hindered by scalability issues, not least because of imperfections in the fabrication process. Recent advances in CQED technologies have enabled to envision to couple several of these systems together (see figure 41). Such CQED arrays have been drawing a lot of attention for the ease of creation and detection offered by optical techniques as well as for the intrinsically out-of-equilibrium nature of the system. This line of research led to the emergence of new quantum photonic phases: an 8-site dissipatively stabilized Mott insulator of photons [257] and a 7-site strongly correlated fluid of light [350]. While these first discoveries had a huge transversal impact in condensed matter, atomic physics and quantum technologies, these photonic states were still limited to the few-body regime (less than ten particles).

4.3. Towards quantum simulation with strongly interacting photons

4.3.1. Strongly interacting quantum fluids of light in propagating geometry

We will advance the state of the art of quantum simulation by bringing 2D quantum fluids of light in the propagating geometry to the strongly interacting regime by mapping the strong interactions that exists between Rydberg atomic states onto the photons using Electromagnetic Induced Transparency (EIT) (see figure 42). The resulting interactions on the probe photons in will be strong, nonlocal and potentially long ranged (if we involve another Rydberg state and couple it with a microwave field to the one that is addressed by the control laser). This will simulate the out-of-equilibrium quantum dynamics ("effective time" evolution as the light field propagates inside the atomic medium) of a strongly interacting 2D fluid of light with exotic properties. This system can be considered as a quantum simulator since by precisely controlling the parameters of the lasers, we can adjust either the strength of the interactions between the photons and the shape and amplitude of the external potential. This will open a new approach for exploring emergent quantum phenomena like supersolidity, crystallization of light on a novel hybrid

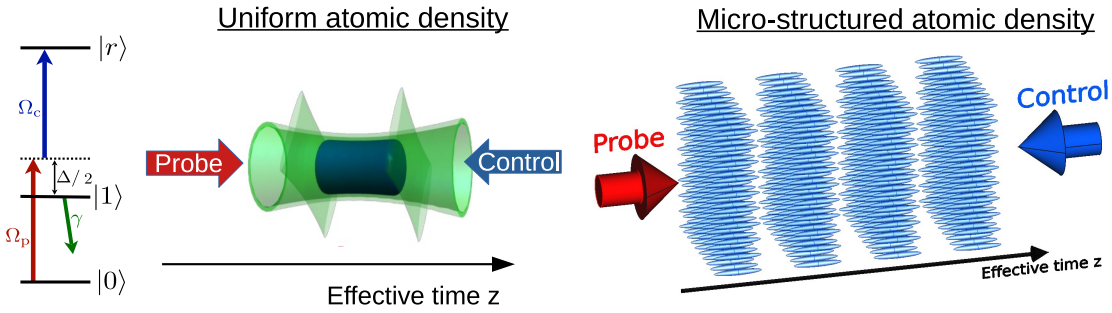

Figure 42. ***Overview of the experimental platform to explore strongly interacting quantum fluids of light in propagating geometry.*** *The strong interactions between atoms excited to Rydberg states are mapped to the probe photons using Rydberg EIT. Either uniform or micro-structured atomic densities will be investigated, leading to uniform or micro-structured photon-photon interactions.*

atom-light platform for quantum simulation. Note that these new phases of matter have recently attracted a lot of attention since their first observation with ultracold atoms [Cho22]. Our platform provides full control over the initial (input) state (intensity, phase, light quantum fluctuations) and enables to probe the final (output) state with a large variety of easily accessible observables like the intensity, phase, coherence $g^{(1)}$, static structure factor and quantum correlations $g^{(2)}$ which are typically more difficult to access in purely atomic systems. Finally, we will push the limits of our quantum simulator deep into the quantum regime by exploring the photonic Mott-to-Superfluid (SF) transition by engineering extremely large photon-photon interactions and adding a 2D periodic potential for the photons. The Mott-to-SF transition can be crossed by either changing the strength of the photon-photon interactions or by modifying the parameters of the 2D periodic potential. The output state of the quantum simulation will be fully characterized by measuring the cross correlations between the optical modes.

4.3.2. Strongly-coupled atom-cavity systems

We will create an original platform to simulate coupled CQED systems using small ensembles of strongly interacting three-level atoms without the need of an actual optical cavity (see figure 43). Combined with our ability to create large arrays of atomic micro-ensembles in arbitrary geometry [405], our approach will overcome the scalability problem encountered in the fabrication process of solid state devices as our implementation is naturally resistant to the defects that are common to solid state systems. Indeed, in the CQED implementation proposed in this project, the Q-factor and resonant frequency of the cavity, the transition frequency of the emitter, the atom-field coupling term, and the couplings between the sites are all fixed by the natural properties of the atoms and by the parameters of our very precisely controlled laser system. First, we will show that a Rydberg blockaded ensemble of three-level atoms that are coupled by lasers maps to the Jaynes-Cummings (JC) model by revealing the spectrum of the dressed states of the system which are polaritons: superposition of a Rydberg excitation and of the excitations

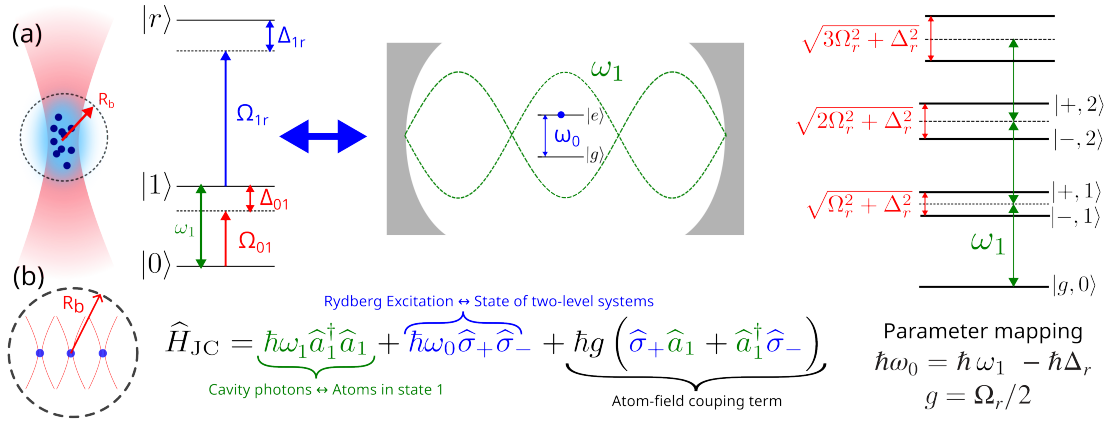

Figure 43. *Mapping of either [**(a)** a Rydberg blockaded ensemble of three-level atoms trapped in a single optical tweezer] or [**(b)** several individual three-level atoms in optical tweezers inside a blockaded sphere] to the JC model which also describes a strongly coupled atom-cavity system. The spectrum the system is nonlinear and called the JC ladder. The dressed-states (polaritons) will be exploited to encode and process quantum information as a qudit.*

of a bosonic mode played by the number of atoms in the intermediate state (two-level system excitation and photons in the original CQED system) (see figure 43). We will then exploit the dressed states to store quantum information and realize arbitrary unitary transformation on the Hilbert space spanned by the dressed states. This will enable to use an ensemble of N three-level atoms as a qudit of dimension $2N$, thus going well beyond the state of the art that uses an atomic ensemble to collectively encode a qubit (dimension 2) [265].

We will then explore several strategies to couple two Rydberg blockaded atomic ensembles (atom-cavity systems) together either by coupling them through their Rydberg excitations (equivalent of having an interaction between the two-level systems in neighboring cavities) or by engineering coupling schemes to coherently transfer population of the intermediate state between two atomic ensembles (equivalent of coupling the atom-cavity systems through photon tunneling between to neighboring cavities). This will pave the way to develop an entangling gate between two neighboring Rydberg blockaded atomic ensembles (qudits) which together with the ability to realize arbitrary unitary operations on a single qudit will enable to explore new ways to process quantum information with large arrays of strongly-coupled atom-cavity systems.

Moreover, as displayed in figure 44 large arrays of Rydberg blockaded atomic ensembles will also provide a novel approach to realizing quantum simulation of coupled atom-cavity models with

- Full control over the parameters of the Hamiltonian: the coupling strength between the Rydberg excitation and the bosonic mode (the light-matter coupling between the two-level system and the photons) and the coupling strength between the sites (photon tunneling rate between the sites)

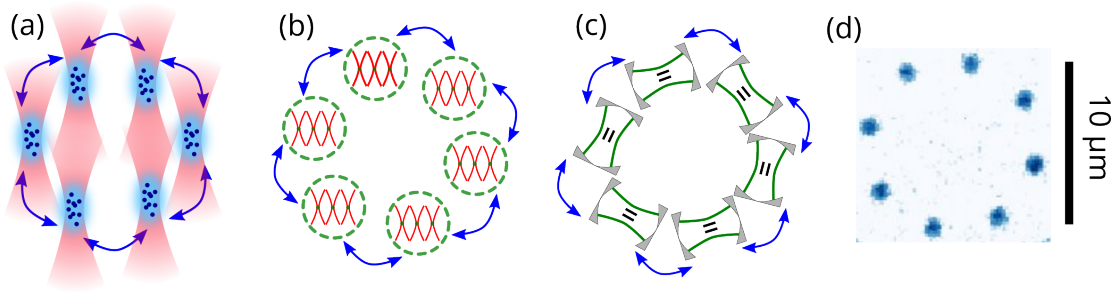

Figure 44. *Engineering couplings between the sites of an array of* ***(a)*** *Rydberg blockaded atomic ensembles,* ***(b)*** *groups of single atoms in optical tweezers inside blockaded spheres* ***(c)*** *strongly-coupled atom-cavity systems all pave the way towards (i) the creation of an entangling quantum gate between the sites (qudits) for quantum information processing on a large qudit register (ii) the quantum simulation of Jaynes-Cummings-Hubbard-like models which leads to a quantum phase transition for photons.* ***(d)*** *Absorption imaging of a 8-site 1D array of potassium micro-ensembles in optical tweezers from the EQM lab that will simulate* ***(a)****. Source: Own experimental data from the potassium experiment of CESQ in preparation of this project. Note that we can also produce large arrays of potassium micro-ensembles in 1D or 2D with hundreds of sites [Wan20].*

- Easy access to observables with single-site resolution (including measuring the presence of a Rydberg excitation or the number of excitation of the bosonic mode) or more global spectroscopic methods.

This will enable to use this quantum simulator to investigate the photonic Mott-to-SF transition which will be monitored by measuring the variance of the total polaritonic excitations at a given site when the coupling strength between the Rydberg excitation and the bosonic mode is varied.

A. Appendix

A.1. Career overview

Over the last 14 years, I have built a unique international research profile in experimental atomic, molecular and optical physics. My expertise includes the experimental investigation of cooperative effects in cold atomic clouds, atomic ultra-cold Bose gases and quantum fluids of light.

During my PhD, I finished building an experimental setup of rubidium atoms to study cooperative effects in light scattering by a cloud of cold atoms. My major achievements were the observation of a cooperative radiation pressure force, the development of a blue detuned box potential to dynamically compress the cold atomic cloud to large densities and a seminal theoretical work on how to control subradiance in large cloud of cold atoms that subsequently guided the observation of this effect in 2016 in the group of R. Kaiser.

As a postdoc I decided to explore the physics of ultracold Bose gases. Towards this goal, I first joined the group of Prof. Dalibard in Paris where I supervised the construction of a new experimental setup for the exploration of two dimensional Bose gases with rubidium atoms that led to a publication about an optical accordion to confine and dynamically compress a gas of cold atoms in two dimensions [P19] and another one about cooperative light scattering in a dense cold atomic layer in connection with my PhD research topic [P17]. In addition, I supervised a second ultracold rubidium setup where we trapped 2D Bose gases in uniform potentials to explore the creation of topological defects when the system is quenched through the normal-to-superfluid transition [P9] [P8]. In my second postdoc, I joined the group of Prof. Ferrari in Trento where I continued working on the physics of topological defects in Bose-Einstein condensates (BECs), this time on an ultracold sodium setup. I developed a technique to follow in a non destructive way the dynamics of vortex lines to analyze their interactions [P6] [P18]. The vortex lines were created by quench cooling [P20]. I also supervised a new research topic in Trento about spinor BEC which led me to observe for the first time spin superfluidity in binary mixture of BECs [P7] [P5].

As a lecturer at École Normale Supérieure I decided to combine my past experiences to explore the emerging field of quantum fluids of light in the group of Prof. Bramati. While the historical experimental platform of the group was polaritons in semi-conductor micro-cavities, together with Assoc. Prof. Glorieux, we led a small team to develop a new platform for the exploration of quantum fluids of light: light propagating in a hot atomic vapor. We established this experimental system in the community as a promising and complementary setup for the investigation of quantum fluids of light by obtaining outstanding results including the measurement of the dispersion relation of quasi-particle excitations [P4] [P14], the observation of dispersive shockwaves [P3] [P13] [P11], the study of pre-thermalization [P2], the exploration of the effect of a quench of the photon-photon interactions [P1] and spin-orbit-coupled fluids of light [P12]. In addition, we also developped a powerful experimental technique to measure the strength of the photon-photon interactions [P10]. As side projects complementary to the quantum fluids of light activity I developed a displacement sensor exploiting a nanofiber [P15] and

a technique to generate attenuation-free non-diffracting Bessel beams [P16].

As a CNRS researcher at the European Center for Quantum Sciences / ISIS. The next step of my career was driven by my desire to push the frontier of quantum fluids of light to a complete new regime where photon-photon interactions are strong. This led me into the physics of Rydberg atoms which enables the creation of strongly correlated fluids of light by exploiting the extreme properties of Rydbgerg atoms. Towards this objective, I joined the European Center for Quantum Sciences (CESQ) in October 2021 as a CNRS permanent researcher to benefit from the expertise of my colleague Prof. Whitlock about cold Rydberg systems and start developing my own projects on the potassium setup of CESQ. In 2022, I secured two research grants to hire two PhD students and buy specific equipment to complement the potassium setup and initiate my independent research team on strongly interacting quantum fluids of light with Rydberg atoms.

A.2. Publications (2014 – 2023)

Publications covered in this report

[P1] *Analogue cosmological particle creation in an ultracold quantum fluid of light*
J. Steinhauer, M. Abuzarli, T. Aladjidi, **T. Bienaimé**, C. Piekarski, W. Liu, E. Giacobino, A. Bramati and Q. Glorieux
Nat. Commun. **13**, 2890 (2022). Editors' Highlights

[P2] *Non-equilibrium pre-thermal states in a two-dimensional photon fluid*
M. Abuzarli, N. Cherroret, **T. Bienaimé** and Q. Glorieux
Phys. Rev. Lett. **129**, 100602 (2022). Editors' Suggestion

[P3] *Quantitative Analysis of Shock Wave Dynamics in a Fluid of Light*
T. Bienaimé, M. Isoard, Q. Fontaine, A. Bramati, A. M. Kamchatnov, Q. Glorieux and N. Pavloff
Phys. Rev. Lett. **126**, 183901 (2021).

[P4] *Observation of the Bogoliubov dispersion relation in a fluid of light*
Q. Fontaine, **T. Bienaimé**, S. Pigeon, E. Giacobino, A. Bramati and Q. Glorieux
Phys. Rev. Lett. **121**, 183604 (2018). Editors' Suggestion

[P5] *Observation of Spin Superfluidity in a Bose Gas Mixture*
E. Fava, **T. Bienaimé**, C. Mordini, G. Colzi, C. Qu, S. Stringari, G. Lamporesi and G. Ferrari
Phys. Rev. Lett. **120**, 170401 (2018).

[P6] *Vortex reconnections and rebounds in trapped atomic Bose-Einstein condensates*
S. Serafini, L. Galantucci, E. Iseni, **T. Bienaimé**, R. N. Bisset, C. F. Barenghi, F. Dalfovo, G. Lamporesi and G. Ferrari
Phys. Rev. X **7**, 021031 (2017).

[P7] *Spin-Dipole Oscillation and Polarizability of a Binary Bose-Einstein Condensate near the Miscible-Immiscible Phase Transition*
T. Bienaimé, E. Fava, G. Colzi, C. Mordini, S. Serafini, C. Qu, S. Stringari, G. Lamporesi and G. Ferrari
Phys. Rev. A **94**, 063652 (2016).

[P8] *Emergence of coherence via transverse condensation in a uniform quasi-two-dimensional Bose gas*
L. Chomaz, L. Corman, **T. Bienaimé**, R. Desbuquois, C. Weitenberg, S. Nascimbène, J. Beugnon and J. Dalibard
Nat. Commun. **6**, 6162 (2015).

[P9] *Quench-induced supercurrents in an annular Bose gas*
L. Corman, L. Chomaz, **T. Bienaimé**, R. Desbuquois, C. Weitenberg, S. Nascimbène, J. Dalibard and J. Beugnon
Phys. Rev. Lett. **113**, 135302 (2014).

Other relevant publications

[P10] *Transit effects for non-linear index measurement in hot atomic vapors*
T. Aladjidi, M. Abuzarli, G. Brochier, **T. Bienaimé**, T. Picot, A. Bramati and Q. Glorieux
arXiv:2202.05764 (2022).

[P11] *Dissipation-enhanced collapse singularity of a nonlocal fluid of light in a hot atomic vapor*
P. Azam, A. Fusaro, Q. Fontaine, J. Garnier, A. Bramati, A. Picozzi, R. Kaiser, Q. Glorieux and **T. Bienaimé**
Phys. Rev. A **104**, 013515 (2021).

[P12] *Spin-orbit-coupled fluids of light in bulk nonlinear media*
G. Martone, **T. Bienaimé** and N. Cherroret
Phys. Rev. A **104**, 013510 (2021).

[P13] *Blast waves in a paraxial fluid of light*
M. Abuzarli, **T. Bienaimé**, E. Giacobino, A. Bramati and Q. Glorieux
EPL **134**, 24001 (2021).

[P14] *Interferences between Bogoliubov excitations and their impact on the evidence of superfluidity in a paraxial fluid of light*
Q. Fontaine, P.-E. Larré, G. Lerario, **T. Bienaimé**, S. Pigeon, D. Faccio, I. Carusotto, E. Giacobino, A. and Q. Glorieux
Phys. Rev. Research **2**, 043297 (2020).

[P15] *Nanofiber based displacement sensor*
C. Ding, M. Joos, C. Bach, **T. Bienaimé**, E. Giacobino, E Wu, A. Bramati and Q. Glorieux
Applied Physics B **126**, 103 (2020).

[P16] *Attenuation-free non-diffracting Bessel beams*
Q. Fontaine, H. Hu, S. Pigeon, **T. Bienaimé**, E. Wu, E. Giacobino, A. Bramati and Q. Glorieux
Optics Express **27**, 30067 (2019).

[P17] *Transmission of near-resonant light through a dense slab of cold atoms*
L. Corman, J. L. Ville, R. Saint-Jalm, M. Aidelsburger, **T. Bienaimé**, S. Nascimbène, J. Dalibard and J. Beugnon
Phys. Rev. A **96**, 053629 (2017). Editors' Suggestion

[P18] *Observation of a spinning top in a Bose-Einstein condensate*
R. N. Bisset, S. Serafini, E. Iseni, M. Barbiero, **T. Bienaimé**, G. Lamporesi, G. Ferrari and F. Dalfovo
Phys. Rev. A **96**, 053605 (2017). Featured in Physics: Synopsis – Editors' Suggestion

[P19] *Loading and compression of a single 2D Bose gas in an optical accordion*
J. L. Ville, **T. Bienaimé**, R. Saint-Jalm, L. Corman, M. Aidelsburger, L. Chomaz, K. Kleinlein, D. Perconte, S. Nascimbène, J. Dalibard and J. Beugnon
Phys. Rev. A **95**, 013632 (2017).

[P20] *Creation and counting of defects in a temperature quenched Bose-Einstein Condensate*
S. Donadello, S. Serafini, **T. Bienaimé**, F. Dalfovo, G. Lamporesi and G. Ferrari
Phys. Rev. A **94**, 023628 (2016).

References

[1] M. Abad and A. Recati. A study of coherently coupled two-component bose-einstein condensates. *The European Physical Journal D*, 67:1–11, 2013.

[2] M. Abad, A. Recati, S. Stringari, and F. Chevy. Counter-flow instability of a quantum mixture of two superfluids. *The European Physical Journal D*, 69:1–5, 2015.

[3] D. A. Abanin, E. Altman, I. Bloch, and M. Serbyn. Colloquium: Many-body localization, thermalization, and entanglement. *Reviews of Modern Physics*, 91(2):021001, 2019.

[4] N. Aghanim, Y. Akrami, F. Arroja, M. Ashdown, J. Aumont, C. Baccigalupi, M. Ballardini, A. J. Banday, R. Barreiro, N. Bartolo, et al. Planck 2018 results-i. overview and the cosmological legacy of planck. *Astronomy & Astrophysics*, 641:A1, 2020.

[5] S. Akhmanov, A. Sukhorukov, and R. Khokhlov. Self-focusing and self-trapping of intense light beams in a nonlinear medium. *Sov. Phys. JETP*, 23(1966):1025–1033, 1966.

[6] A. Albrecht, D. Coulson, P. Ferreira, and J. Magueijo. Causality, randomness, and the microwave background. *Physical Review Letters*, 76(9):1413, 1996.

[7] A. Albrecht, P. J. Steinhardt, M. S. Turner, and F. Wilczek. Reheating an inflationary universe. *Physical Review Letters*, 48(20):1437, 1982.

[8] A. J. Allen, S. Zuccher, M. Caliari, N. P. Proukakis, N. G. Parker, and C. F. Barenghi. Vortex reconnections in atomic condensates at finite temperature. *Phys. Rev. A*, 90:013601, Jul 2014.

[9] J. F. Allen and A. Misener. Flow of liquid helium ii. *Nature*, 141(3558):75–75, 1938.

[10] A. Amo, J. Lefrère, S. Pigeon, C. Adrados, C. Ciuti, I. Carusotto, R. Houdré, E. Giacobino, and A. Bramati. Superfluidity of polaritons in semiconductor microcavities. *Nature Physics*, 5(11):805–810, 2009.

[11] B. P. Anderson, P. C. Haljan, C. E. Wieman, and E. A. Cornell. Vortex precession in bose-einstein condensates: Observations with filled and empty cores. *Phys. Rev. Lett.*, 85:2857–2860, Oct 2000.

[12] M. H. Anderson, J. R. Ensher, M. R. Matthews, C. E. Wieman, and E. A. Cornell. Observation of bose-einstein condensation in a dilute atomic vapor. *science*, 269(5221):198–201, 1995.

[13] A. Andreev and E. Bashkin. Three-velocity hydrodynamics of superfluid solutions. *Soviet Journal of Experimental and Theoretical Physics*, 42:164, 1975.

[14] M. R. Andrews, C. G. Townsend, H.-J. Miesner, D. S. Durfee, D. M. Kurn, and W. Ketterle. Observation of interference between two bose condensates. *Science*, 275(5300):637–641, 1997.

[15] J. R. Anglin and W. H. Zurek. Vortices in the wake of rapid bose-einstein condensation. *Phys. Rev. Lett.*, 83:1707–1710, Aug 1999.

[16] J. Armaitis and R. Duine. Superfluidity and spin superfluidity in spinor bose gases. *Physical Review A*, 95(5):053607, 2017.

[17] J. Armaitis, H. Stoof, and R. Duine. Hydrodynamic modes of partially condensed bose mixtures. *Physical Review A*, 91(4):043641, 2015.

[18] J. Armijo, T. Jacqmin, K. Kheruntsyan, and I. Bouchoule. Mapping out the quasicondensate transition through the dimensional crossover from one to three dimensions. *Phys. Rev. A*, 83:021605, Feb 2011.

[19] A. Aspuru-Guzik and P. Walther. Photonic quantum simulators. *Nature physics*, 8(4):285–291, 2012.

[20] A. W. Baggaley, J. Laurie, and C. F. Barenghi. Vortex-density fluctuations, energy spectra, and vortical regions in superfluid turbulence. *Phys. Rev. Lett.*, 109:205304, Nov 2012.

[21] W. S. Bakr, J. I. Gillen, A. Peng, S. Fölling, and M. Greiner. A quantum gas microscope for detecting single atoms in a hubbard-regime optical lattice. *Nature*, 462(7269):74–77, 2009.

[22] R. Balili, V. Hartwell, D. Snoke, L. Pfeiffer, and K. West. Bose-einstein condensation of microcavity polaritons in a trap. *Science*, 316(5827):1007–1010, 2007.

[23] C. Barcelo, S. Liberati, and M. Visser. Analogue models for frw cosmologies. *International Journal of Modern Physics D*, 12(09):1641–1649, 2003.

[24] C. Barcelo, S. Liberati, and M. Visser. Probing semiclassical analog gravity in bose-einstein condensates with widely tunable interactions. *Physical Review A*, 68(5):053613, 2003.

[25] J. M. Bardeen, P. J. Steinhardt, and M. S. Turner. Spontaneous creation of almost scale-free density perturbations in an inflationary universe. *Physical Review D*, 28(4):679, 1983.

[26] A. Bardon, S. Beattie, C. Luciuk, W. Cairncross, D. Fine, N. Cheng, G. Edge, E. Taylor, S. Zhang, S. Trotzky, et al. Transverse demagnetization dynamics of a unitary fermi gas. *Science*, 344(6185):722–724, 2014.

[27] T. Bardon-brun, S. Pigeon, and N. Cherroret. Classical casimir force from a quasi-condensate of light. *Phys. Rev. Res.*, 2:013297, Mar 2020.

[28] C. F. Barenghi, R. J. Donnelly, and W. Vinen. *Quantized vortex dynamics and superfluid turbulence*, volume 571. Springer Science & Business Media, 2001.

[29] C. F. Barenghi, V. S. L'vov, and P.-E. Roche. Experimental, numerical, and analytical velocity spectra in turbulent quantum fluid. *Proceedings of the National Academy of Sciences*, 111(supplement_1):4683–4690, 2014.

[30] C. Barsi, W. Wan, C. Sun, and J. W. Fleischer. Dispersive shock waves with nonlocal nonlinearity. *Optics letters*, 32(20):2930–2932, 2007.

[31] K. Baudin, A. Fusaro, K. Krupa, J. Garnier, S. Rica, G. Millot, and A. Picozzi. Classical rayleigh-jeans condensation of light waves: Observation and thermodynamic characterization. *Physical Review Letters*, 125(24):244101, 2020.

[32] C. Bäuerle, Y. M. Bunkov, S. Fisher, H. Godfrin, and G. Pickett. Laboratory simulation of cosmic string formation in the early universe using superfluid 3he. *Nature*, 382(6589):332–334, 1996.

[33] S. Beattie, S. Moulder, R. J. Fletcher, and Z. Hadzibabic. Persistent currents in spinor condensates. *Phys. Rev. Lett.*, 110:025301, Jan 2013.

[34] C. Becker, K. Sengstock, P. Schmelcher, P. Kevrekidis, and R. Carretero-González. Inelastic collisions of solitary waves in anisotropic bose–einstein condensates: sling-shot events and expanding collision bubbles. *New Journal of Physics*, 15(11):113028, 2013.

[35] P. J. Bendt. Superfluid helium critical velocities in a rotating annulus. *Phys. Rev.*, 127:1441–1445, Sep 1962.

[36] C. L. Bennett, D. Larson, J. L. Weiland, N. Jarosik, G. Hinshaw, N. Odegard, K. Smith, R. Hill, B. Gold, M. Halpern, et al. Nine-year wilkinson microwave anisotropy probe (wmap) observations: final maps and results. *The Astrophysical Journal Supplement Series*, 208(2):20, 2013.

[37] V. L. Berezinsky. Destruction of Long-range Order in One-dimensional and Two-dimensional Systems Possessing a Continuous Symmetry Group. II. Quantum Systems. *Sov. Phys. JETP*, 34(3):610, 1972.

[38] J. Berges, S. Borsányi, and C. Wetterich. Prethermalization. *Phys. Rev. Lett.*, 93:142002, Sep 2004.

[39] M. Berry and M. Dennis. Reconnections of wave vortex lines. *European journal of physics*, 33(3):723, 2012.

[40] G. P. Bewley, D. P. Lathrop, and K. R. Sreenivasan. Visualization of quantized vortices. *Nature*, 441(7093):588–588, 2006.

[41] G. P. Bewley, M. S. Paoletti, K. R. Sreenivasan, and D. P. Lathrop. Characterization of reconnecting vortices in superfluid helium. *Proceedings of the National Academy of Sciences*, 105(37):13707–13710, 2008.

[42] T. Bienaimé, E. Fava, G. Colzi, C. Mordini, S. Serafini, C. Qu, S. Stringari, G. Lamporesi, and G. Ferrari. Spin-dipole oscillation and polarizability of a binary bose-einstein condensate near the miscible-immiscible phase transition. *Phys. Rev. A*, 94:063652, Dec 2016.

[43] J. Billy, V. Josse, Z. Zuo, A. Bernard, B. Hambrecht, P. Lugan, D. Clément, L. Sanchez-Palencia, P. Bouyer, and A. Aspect. Direct observation of anderson localization of matter waves in a controlled disorder. *Nature*, 453(7197):891–894, 2008.

[44] K. M. Birnbaum, A. Boca, R. Miller, A. D. Boozer, T. E. Northup, and H. J. Kimble. Photon blockade in an optical cavity with one trapped atom. *Nature*, 436(7047):87–90, 2005.

[45] R. N. Bisset, M. J. Davis, T. P. Simula, and P. B. Blakie. Quasicondensation and coherence in the quasi-two-dimensional trapped bose gas. *Phys. Rev. A*, 79:033626, Mar 2009.

[46] R. N. Bisset, R. M. Wilson, and C. Ticknor. Scaling of fluctuations in a trapped binary condensate. *Phys. Rev. A*, 91:053613, May 2015.

[47] R. Blatt and C. F. Roos. Quantum simulations with trapped ions. *Nature Physics*, 8(4):277–284, 2012.

[48] I. Bloch, J. Dalibard, and S. Nascimbene. Quantum simulations with ultracold quantum gases. *Nature Physics*, 8(4):267–276, 2012.

[49] I. Bloch, J. Dalibard, and W. Zwerger. Many-body physics with ultracold gases. *Reviews of modern physics*, 80(3):885, 2008.

[50] A. Blumkin, S. Rinott, R. Schley, A. Berkovitz, I. Shammass, and J. Steinhauer. Observing atom bunching by the fourier slice theorem. *Physical Review Letters*, 110(26):265301, 2013.

[51] N. Bogoliubov. Toward a theory of superfluidity [in russian]. *Izv. AN SSSR. Ser. Phys.*, 11:77–90, 1947.

[52] A. N. Bohr and B. R. Mottelson. *Nuclear Structure (in 2 volumes)*. World Scientific Publishing Company, 1998.

[53] F. Böttcher, J.-N. Schmidt, M. Wenzel, J. Hertkorn, M. Guo, T. Langen, and T. Pfau. Transient supersolid properties in an array of dipolar quantum droplets. *Phys. Rev. X*, 9:011051, Mar 2019.

[54] O. Boughdad, A. Eloy, F. Mortessagne, M. Bellec, and C. Michel. Anisotropic nonlinear refractive index measurement of a photorefractive crystal via spatial self-phase modulation. *Optics express*, 27(21):30360–30370, 2019.

[55] C. C. Bradley, C. A. Sackett, J. J. Tollett, and R. G. Hulet. Evidence of bose-einstein condensation in an atomic gas with attractive interactions. *Phys. Rev. Lett.*, 75:1687–1690, Aug 1995.

[56] J. Brand and W. P. Reinhardt. Solitonic vortices and the fundamental modes of the "snake instability": Possibility of observation in the gaseous bose-einstein condensate. *Phys. Rev. A*, 65:043612, Apr 2002.

[57] R. H. Brandenberger. Lectures on the theory of cosmological perturbations. *LECTURE NOTES IN PHYSICS-NEW YORK THEN BERLIN-*, 646:127–168, 2004.

[58] S. Braun, M. Friesdorf, S. S. Hodgman, M. Schreiber, J. P. Ronzheimer, A. Riera, M. Del Rey, I. Bloch, J. Eisert, and U. Schneider. Emergence of coherence and the dynamics of quantum phase transitions. *Proceedings of the National Academy of Sciences*, 112(12):3641–3646, 2015.

[59] V. Bretin, P. Rosenbusch, F. Chevy, G. V. Shlyapnikov, and J. Dalibard. Quadrupole oscillation of a single-vortex bose-einstein condensate: Evidence for kelvin modes. *Phys. Rev. Lett.*, 90:100403, Mar 2003.

[60] V. Bretin, S. Stock, Y. Seurin, and J. Dalibard. Fast rotation of a bose-einstein condensate. *Phys. Rev. Lett.*, 92:050403, Feb 2004.

[61] A. Browaeys and T. Lahaye. Many-body physics with individually controlled rydberg atoms. *Nature Physics*, 16(2):132–142, 2020.

[62] E. Busley, L. E. Miranda, A. Redmann, C. Kurtscheid, K. K. Umesh, F. Vewinger, M. Weitz, and J. Schmitt. Compressibility and the equation of state of an optical quantum gas in a box. *Science*, 375(6587):1403–1406, 2022.

[63] T. Byrnes, N. Y. Kim, and Y. Yamamoto. Exciton–polariton condensates. *Nature Physics*, 10(11):803–813, 2014.

[64] D. Campo and R. Parentani. Inflationary spectra and partially decohered distributions. *Physical Review D*, 72(4):045015, 2005.

[65] S. H. Cantu, A. V. Venkatramani, W. Xu, L. Zhou, B. Jelenković, M. D. Lukin, and V. Vuletić. Repulsive photons in a quantum nonlinear medium. *Nature Physics*, 16(9):921–925, 2020.

[66] I. Carusotto. Superfluid light in bulk nonlinear media. *Proceedings of the Royal Society A: Mathematical, Physical and Engineering Sciences*, 470(2169):20140320, 2014.

[67] I. Carusotto. Quantum fluids of light, 2022.

[68] I. Carusotto and C. Ciuti. Quantum fluids of light. *Rev. Mod. Phys.*, 85:299–366, Feb 2013.

[69] Y. Castin and R. Dum. Bose-einstein condensates in time dependent traps. *Physical Review Letters*, 77(27):5315, 1996.

[70] Y. Castin, I. Ferrier-Barbut, and C. Salomon. La vitesse critique de landau d'une particule dans un superfluide de fermions. *Comptes Rendus Physique*, 16(2):241–253, 2015.

[71] D. E. Chang, V. Vuletić, and M. D. Lukin. Quantum nonlinear optics—photon by photon. *Nature Photonics*, 8(9):685–694, 2014.

[72] H. Che, J. Drake, and M. Swisdak. A current filamentation mechanism for breaking magnetic field lines during reconnection. *Nature*, 474(7350):184–187, 2011.

[73] C.-A. Chen, S. Khlebnikov, and C.-L. Hung. Observation of quasiparticle pair production and quantum entanglement in atomic quantum gases quenched to an attractive interaction. *Physical Review Letters*, 127(6):060404, 2021.

[74] D. Chen, M. White, C. Borries, and B. DeMarco. Quantum quench of an atomic mott insulator. *Phys. Rev. Lett.*, 106:235304, Jun 2011.

[75] N. Cherroret, T. Scoquart, and D. Delande. Coherent multiple scattering of out-of-equilibrium interacting bose gases. *Annals of Physics*, 435:168543, 2021.

[76] F. Chevy, V. Bretin, P. Rosenbusch, K. W. Madison, and J. Dalibard. Transverse breathing mode of an elongated bose-einstein condensate. *Phys. Rev. Lett.*, 88:250402, Jun 2002.

[77] R. Y. Chiao. Bogoliubov dispersion relation for aphoton fluid': Is this a superfluid? *Optics communications*, 179(1-6):157–166, 2000.

[78] J.-y. Choi, S. Hild, J. Zeiher, P. Schauß, A. Rubio-Abadal, T. Yefsah, V. Khemani, D. A. Huse, I. Bloch, and C. Gross. Exploring the many-body localization transition in two dimensions. *Science*, 352(6293):1547–1552, 2016.

[79] J.-y. Choi, S. W. Seo, and Y.-i. Shin. Observation of thermally activated vortex pairs in a quasi-2d bose gas. *Phys. Rev. Lett.*, 110:175302, Apr 2013.

[80] L. Chomaz, I. Ferrier-Barbut, F. Ferlaino, B. Laburthe-Tolra, B. L. Lev, and T. Pfau. Dipolar physics: A review of experiments with magnetic quantum gases. *Reports on Progress in Physics*, 2022.

[81] L. Chomaz, D. Petter, P. Ilzhöfer, G. Natale, A. Trautmann, C. Politi, G. Durastante, R. M. W. van Bijnen, A. Patscheider, M. Sohmen, M. J. Mark, and F. Ferlaino. Long-lived and transient supersolid behaviors in dipolar quantum gases. *Phys. Rev. X*, 9:021012, Apr 2019.

[82] I. Chuang, R. Durrer, N. Turok, and B. Yurke. Cosmology in the laboratory: Defect dynamics in liquid crystals. *Science*, 251(4999):1336–1342, 1991.

[83] J. W. Cirtain, L. Golub, A. Winebarger, B. De Pontieu, K. Kobayashi, R. Moore, R. W. Walsh, K. Korreck, M. Weber, P. McCauley, et al. Energy release in the solar corona from spatially resolved magnetic braids. *Nature*, 493(7433):501–503, 2013.

[84] P. Cladé, C. Ryu, A. Ramanathan, K. Helmerson, and W. D. Phillips. Observation of a 2d bose gas: From thermal to quasicondensate to superfluid. *Phys. Rev. Lett.*, 102:170401, Apr 2009.

[85] L. W. Clark, N. Schine, C. Baum, N. Jia, and J. Simon. Observation of laughlin states made of light. *Nature*, 582(7810):41–45, 2020.

[86] P. Clark di Leoni, P. D. Mininni, and M. E. Brachet. Helicity, topology, and kelvin waves in reconnecting quantum knots. *Phys. Rev. A*, 94:043605, Oct 2016.

[87] S. P. Cockburn and N. P. Proukakis. Ab initio methods for finite-temperature two-dimensional bose gases. *Phys. Rev. A*, 86:033610, Sep 2012.

[88] W. Colson and A. L. Fetter. Mixtures of bose liquids at finite temperature. *Journal of Low Temperature Physics*, 33:231–242, 1978.

[89] R. Cominotti, A. Berti, A. Farolfi, A. Zenesini, G. Lamporesi, I. Carusotto, A. Recati, and G. Ferrari. Observation of massless and massive collective excitations with faraday patterns in a two-component superfluid. *Phys. Rev. Lett.*, 128:210401, May 2022.

[90] T. Congy, G. El, and M. Hoefer. Interaction of linear modulated waves and unsteady dispersive hydrodynamic states with application to shallow water waves. *Journal of Fluid Mechanics*, 875:1145–1174, 2019.

[91] P. Coullet, L. Gil, and F. Rocca. Optical vortices. *Optics Communications*, 73(5):403–408, 1989.

[92] R. Courant and K. Friedrichs. *Supersonic Flow and Shock Waves*. Applied Mathematical Sciences. Springer New York, 1999.

[93] J.-L. Coutaz and M. Kull. Saturation of the nonlinear index of refraction in semiconductor-doped glass. *JOSA B*, 8(1):95–98, 1991.

[94] G. Couton, H. Maillotte, and M. Chauvet. Self-formation of multiple spatial photovoltaic solitons. *Journal of Optics B: Quantum and Semiclassical Optics*, 6(5):S223, 2004.

[95] M. Cozzini, S. Stringari, V. Bretin, P. Rosenbusch, and J. Dalibard. Scissors mode of a rotating bose-einstein condensate. *Phys. Rev. A*, 67:021602, Feb 2003.

[96] F. Dalfovo, S. Giorgini, L. P. Pitaevskii, and S. Stringari. Theory of bose-einstein condensation in trapped gases. *Rev. Mod. Phys.*, 71:463–512, Apr 1999.

[97] T. Damm, D. Dung, F. Vewinger, M. Weitz, and J. Schmitt. First-order spatial coherence measurements in a thermalized two-dimensional photonic quantum gas. *Nature communications*, 8(1):158, 2017.

[98] A. Das, J. Sabbatini, and W. H. Zurek. Winding up superfluid in a torus via bose einstein condensation. *Scientific reports*, 2(1):1–6, 2012.

[99] S. Datta and U. R. Fischer. Fluid-dynamical analogue of nonlinear gravitational wave memory. *arXiv preprint arXiv:2011.05837*, 2020.

[100] K. B. Davis, M. O. Mewes, M. R. Andrews, N. J. van Druten, D. S. Durfee, D. M. Kurn, and W. Ketterle. Bose-einstein condensation in a gas of sodium atoms. *Phys. Rev. Lett.*, 75:3969–3973, Nov 1995.

[101] V. B. DE ST. Theorie du mouvement non-permanent des eaux avec application aux crues des rivers et a l'introduntion des marees dans leur lit. *Academic de Sci. Comptes Redus*, 73(99):148–154, 1871.

[102] A. T. A. M. de Waele and R. G. K. M. Aarts. Route to vortex reconnection. *Phys. Rev. Lett.*, 72:482–485, Jan 1994.

[103] M. Delehaye, S. Laurent, I. Ferrier-Barbut, S. Jin, F. Chevy, and C. Salomon. Critical velocity and dissipation of an ultracold bose-fermi counterflow. *Phys. Rev. Lett.*, 115:265303, Dec 2015.

[104] B. DeMarco and D. S. Jin. Spin excitations in a fermi gas of atoms. *Phys. Rev. Lett.*, 88:040405, Jan 2002.

[105] M. R. Dennis, R. P. King, B. Jack, K. O'holleran, and M. J. Padgett. Isolated optical vortex knots. *Nature Physics*, 6(2):118–121, 2010.

[106] R. Desbuquois, L. Chomaz, T. Yefsah, J. Léonard, J. Beugnon, C. Weitenberg, and J. Dalibard. Superfluid behaviour of a two-dimensional bose gas. *Nature Physics*, 8(9):645–648, 2012.

[107] V. Dodonov. Fifty years of the dynamical casimir effect. *Physics*, 2(1):67–104, 2020.

[108] S. Donadello, S. Serafini, T. Bienaimé, F. Dalfovo, G. Lamporesi, and G. Ferrari. Creation and counting of defects in a temperature-quenched bose-einstein condensate. *Phys. Rev. A*, 94:023628, Aug 2016.

[109] S. Donadello, S. Serafini, M. Tylutki, L. P. Pitaevskii, F. Dalfovo, G. Lamporesi, and G. Ferrari. Observation of solitonic vortices in bose-einstein condensates. *Phys. Rev. Lett.*, 113:065302, Aug 2014.

[110] R. J. Donnelly. *Quantized vortices in helium II*, volume 2. Cambridge University Press, 1991.

[111] J. Dziarmaga and W. H. Zurek. Quench in the 1d bose-hubbard model: Topological defects and excitations from the kosterlitz-thouless phase transition dynamics. *Scientific reports*, 4(1):1–6, 2014.

[112] S. Eckel, F. Jendrzejewski, A. Kumar, C. J. Lobb, and G. K. Campbell. Interferometric measurement of the current-phase relationship of a superfluid weak link. *Phys. Rev. X*, 4:031052, Sep 2014.

[113] S. Eckel, A. Kumar, T. Jacobson, I. B. Spielman, and G. K. Campbell. A rapidly expanding bose-einstein condensate: an expanding universe in the lab. *Physical Review X*, 8(2):021021, 2018.

[114] M. Egorov, B. Opanchuk, P. Drummond, B. V. Hall, P. Hannaford, and A. I. Sidorov. Measurement of s-wave scattering lengths in a two-component bose-einstein condensate. *Phys. Rev. A*, 87:053614, May 2013.

[115] C. Eigen, J. A. Glidden, R. Lopes, E. A. Cornell, R. P. Smith, and Z. Hadzibabic. Universal prethermal dynamics of bose gases quenched to unitarity. *Nature*, 563(7730):221–224, 2018.

[116] G. A. El. Resolution of a shock in hyperbolic systems modified by weak dispersion. *Chaos: An Interdisciplinary Journal of Nonlinear Science*, 15(3):037103, 2005.

[117] G. A. El, A. Gammal, E. G. Khamis, R. A. Kraenkel, and A. M. Kamchatnov. Theory of optical dispersive shock waves in photorefractive media. *Phys. Rev. A*, 76:053813, Nov 2007.

[118] G. A. El' and V. Khodorovsky. Evolution of a solitonless large-scale perturbation in korteweg-de vries hydrodynamics. *Physics Letters A*, 182(1):49–52, 1993.

[119] G. A. El and A. L. Krylov. General solution of the cauchy problem for the defocusing nls equation in the whitham limit. *Physics Letters A*, 203(2-3):77–82, 1995.

[120] M. Elazar, V. Fleurov, and S. Bar-Ad. All-optical event horizon in an optical analog of a laval nozzle. *Phys. Rev. A*, 86:063821, Dec 2012.

[121] S. Erne, R. Bücker, T. Gasenzer, J. Berges, and J. Schmiedmayer. Universal dynamics in an isolated one-dimensional bose gas far from equilibrium. *Nature*, 563(7730):225–229, 2018.

[122] Y. Eto, M. Takahashi, M. Kunimi, H. Saito, and T. Hirano. Nonequilibrium dynamics induced by miscible–immiscible transition in binary bose–einstein condensates. *New Journal of Physics*, 18(7):073029, 2016.

[123] A. Faraon, P. E. Barclay, C. Santori, K.-M. C. Fu, and R. G. Beausoleil. Resonant enhancement of the zero-phonon emission from a colour centre in a diamond cavity. *Nature Photonics*, 5(5):301–305, 2011.

[124] A. Farolfi, D. Trypogeorgos, C. Mordini, G. Lamporesi, and G. Ferrari. Observation of magnetic solitons in two-component bose-einstein condensates. *Phys. Rev. Lett.*, 125:030401, Jul 2020.

[125] A. Farolfi, A. Zenesini, D. Trypogeorgos, C. Mordini, A. Gallemí, A. C. Roy, A. Recati, G. Lamporesi, and G. Ferrari. Quantum-torque-induced breaking of magnetic interfaces in ultracold gases. *Nature Physics*, 17(12):1359–1363, 2021.

[126] J. Fatome, C. Finot, G. Millot, A. Armaroli, and S. Trillo. Observation of optical undular bores in multiple four-wave mixing. *Physical Review X*, 4(2):021022, 2014.

[127] P. O. Fedichev and U. R. Fischer. "cosmological" quasiparticle production in harmonically trapped superfluid gases. *Physical Review A*, 69(3):033602, 2004.

[128] P. O. Fedichev and G. V. Shlyapnikov. Dissipative dynamics of a vortex state in a trapped bose-condensed gas. *Phys. Rev. A*, 60:R1779–R1782, Sep 1999.

[129] F. Ferlaino, R. J. Brecha, P. Hannaford, F. Riboli, G. Roati, G. Modugno, and M. Inguscio. Dipolar oscillations in a quantum degenerate fermi–bose atomic mixture. *Journal of Optics B: Quantum and Semiclassical Optics*, 5(2):S3, 2003.

[130] I. Ferrier-Barbut, M. Delehaye, S. Laurent, A. T. Grier, M. Pierce, B. S. Rem, F. Chevy, and C. Salomon. A mixture of bose and fermi superfluids. *Science*, 345(6200):1035–1038, 2014.

[131] A. L. Fetter. Rotating trapped bose-einstein condensates. *Rev. Mod. Phys.*, 81:647–691, May 2009.

[132] R. Feynman. Progress in low temperature physics. 1955.

[133] O. Firstenberg, T. Peyronel, Q.-Y. Liang, A. V. Gorshkov, M. D. Lukin, and V. Vuletić. Attractive photons in a quantum nonlinear medium. *Nature*, 502(7469):71–75, 2013.

[134] U. R. Fischer and R. Schützhold. Quantum simulation of cosmic inflation in two-component bose-einstein condensates. *Physical Review A*, 70(6):063615, 2004.

[135] M. Fleischhauer, A. Imamoglu, and J. P. Marangos. Electromagnetically induced transparency: Optics in coherent media. *Reviews of modern physics*, 77(2):633, 2005.

[136] E. Fonda, D. P. Meichle, N. T. Ouellette, S. Hormoz, and D. P. Lathrop. Direct observation of kelvin waves excited by quantized vortex reconnection. *Proceedings of the National Academy of Sciences*, 111(supplement_1):4707–4710, 2014.

[137] M. Forest, C. J. Rosenberg, and O. Wright. On the exact solution for smooth pulses of the defocusing nonlinear schrödinger modulation equations prior to breaking. *Nonlinearity*, 22(9):2287, 2009.

[138] D. V. Freilich, D. M. Bianchi, A. M. Kaufman, T. K. Langin, and D. S. Hall. Real-time dynamics of single vortex lines and vortex dipoles in a bose-einstein condensate. *Science*, 329(5996):1182–1185, 2010.

[139] T. Frisch, Y. Pomeau, and S. Rica. Transition to dissipation in a model of superflow. *Physical review letters*, 69(11):1644, 1992.

[140] S. A. Fulling and P. C. Davies. Radiation from a moving mirror in two dimensional spacetime: conformal anomaly. *Proceedings of the Royal Society of London. A. Mathematical and Physical Sciences*, 348(1654):393–414, 1976.

[141] I. Fushman, D. Englund, A. Faraon, N. Stoltz, P. Petroff, and J. Vuckovic. Controlled phase shifts with a single quantum dot. *science*, 320(5877):769–772, 2008.

[142] A. L. Gaunt, T. F. Schmidutz, I. Gotlibovych, R. P. Smith, and Z. Hadzibabic. Bose-einstein condensation of atoms in a uniform potential. *Phys. Rev. Lett.*, 110:200406, May 2013.

[143] N. Ghofraniha, L. S. Amato, V. Folli, S. Trillo, E. DelRe, and C. Conti. Measurement of scaling laws for shock waves in thermal nonlocal media. *Optics letters*, 37(12):2325–2327, 2012.

[144] N. Ghofraniha, C. Conti, G. Ruocco, and S. Trillo. Shocks in nonlocal media. *Phys. Rev. Lett.*, 99:043903, Jul 2007.

[145] N. Ghofraniha, S. Gentilini, V. Folli, E. DelRe, and C. Conti. Shock waves in disordered media. *Phys. Rev. Lett.*, 109:243902, Dec 2012.

[146] L. Giorgetti, I. Carusotto, and Y. Castin. Semiclassical field method for the equilibrium bose gas and application to thermal vortices in two dimensions. *Phys. Rev. A*, 76:013613, Jul 2007.

[147] J. A. Glidden, C. Eigen, L. H. Dogra, T. A. Hilker, R. P. Smith, and Z. Hadzibabic. Bidirectional dynamic scaling in an isolated bose gas far from equilibrium. *Nature Physics*, 17(4):457–461, 2021.

[148] Q. Glorieux, R. Dubessy, S. Guibal, L. Guidoni, J.-P. Likforman, T. Coudreau, and E. Arimondo. Double-λ microscopic model for entangled light generation by four-wave mixing. *Physical Review A*, 82(3):033819, 2010.

[149] C. Gogolin and J. Eisert. Equilibration, thermalisation, and the emergence of statistical mechanics in closed quantum systems. *Reports on Progress in Physics*, 79(5):056001, 2016.

[150] M. Golubitsky. An introduction to catastrophe theory and its applications. *Siam Review*, 20(2):352–387, 1978.

[151] I. Gotlibovych, T. F. Schmidutz, A. L. Gaunt, N. Navon, R. P. Smith, and Z. Hadzibabic. Observing properties of an interacting homogeneous bose-einstein condensate: Heisenberg-limited momentum spread, interaction energy, and free-expansion dynamics. *Phys. Rev. A*, 89:061604, Jun 2014.

[152] M. Greiner, I. Bloch, O. Mandel, T. W. Hänsch, and T. Esslinger. Exploring phase coherence in a 2d lattice of bose-einstein condensates. *Phys. Rev. Lett.*, 87:160405, Oct 2001.

[153] M. Greiner, O. Mandel, T. Esslinger, T. W. Hänsch, and I. Bloch. Quantum phase transition from a superfluid to a mott insulator in a gas of ultracold atoms. *nature*, 415(6867):39–44, 2002.

[154] M. Greiner, C. A. Regal, and D. S. Jin. Emergence of a molecular bose–einstein condensate from a fermi gas. *Nature*, 426(6966):537–540, 2003.

[155] M. Gring, M. Kuhnert, T. Langen, T. Kitagawa, B. Rauer, M. Schreitl, I. Mazets, D. A. Smith, E. Demler, and J. Schmiedmayer. Relaxation and prethermalization in an isolated quantum system. *Science*, 337(6100):1318–1322, 2012.

[156] L. Grishchuk and Y. V. Sidorov. Squeezed quantum states of relic gravitons and primordial density fluctuations. *Physical Review D*, 42(10):3413, 1990.

[157] S. N. Gurbatov, O. V. Rudenko, and A. I. Saichev. *Waves and structures in nonlinear nondispersive media: general theory and applications to nonlinear acoustics*. Springer Science & Business Media, 2012.

[158] A. Gurevich and A. Krylov. Dissipationless shock waves in media with positive dispersion. *Zh. Eksp. Teor. Fiz*, 92:1684, 1987.

[159] A. Gurevich, A. Krylov, and N. Mazur. Quasi-simple waves in korteweg-de fries hydrodynamics. *Zh. Eksp. Teor. Fiz*, 95:1674, 1989.

[160] A. Gurevich and A. Meshcherkin. Expanding self-similar discontinuities and shock waves in dispersive hydrodynamics. *Zhurnal Eksperimental'noi i Teoreticheskoi Fiziki*, 87:1277–1292, 1984.

[161] A. Gurevich and L. Pitaevskii. Nonstationary structure of a collisionless shock wave. *Zhurnal Eksperimentalnoi i Teoreticheskoi Fiziki*, 65:590–604, 1973.

[162] A. H. Guth. Inflationary universe: A possible solution to the horizon and flatness problems. *Physical Review D*, 23(2):347, 1981.

[163] A. H. Guth and S.-Y. Pi. Fluctuations in the new inflationary universe. *Physical Review Letters*, 49(15):1110, 1982.

[164] L.-C. Ha, C.-L. Hung, X. Zhang, U. Eismann, S.-K. Tung, and C. Chin. Strongly interacting two-dimensional bose gases. *Phys. Rev. Lett.*, 110:145302, Apr 2013.

[165] Z. Hadzibabic and J. Dalibard. Two-dimensional bose fluids: An atomic physics perspective. *La Rivista del Nuovo Cimento*, 34:389–434, 2011.

[166] Z. Hadzibabic, P. Krüger, M. Cheneau, B. Battelier, and J. Dalibard. Berezinskii–kosterlitz–thouless crossover in a trapped atomic gas. *Natre*, 441(7097):1118–1121, 2006.

[167] D. S. Hall, M. R. Matthews, J. R. Ensher, C. E. Wieman, and E. A. Cornell. Dynamics of component separation in a binary mixture of bose-einstein condensates. *Phys. Rev. Lett.*, 81:1539–1542, Aug 1998.

[168] K. Hammerer, A. S. Sørensen, and E. S. Polzik. Quantum interface between light and atomic ensembles. *Reviews of Modern Physics*, 82(2):1041, 2010.

[169] C. Hamner, J. J. Chang, P. Engels, and M. A. Hoefer. Generation of dark-bright soliton trains in superfluid-superfluid counterflow. *Phys. Rev. Lett.*, 106:065302, Feb 2011.

[170] B. J. Hausmann, B. Shields, Q. Quan, P. Maletinsky, M. McCutcheon, J. T. Choy, T. M. Babinec, A. Kubanek, A. Yacoby, M. D. Lukin, et al. Integrated diamond networks for quantum nanophotonics. *Nano letters*, 12(3):1578–1582, 2012.

[171] S. W. Hawking. The development of irregularities in a single bubble inflationary universe. *Physics Letters B*, 115(4):295–297, 1982.

[172] J. Higbie, L. Sadler, S. Inouye, A. Chikkatur, S. Leslie, K. Moore, V. Savalli, and D. Stamper-Kurn. Direct nondestructive imaging of magnetization in a spin-1 bose-einstein gas. *Physical Review Letters*, 95(5):050401, 2005.

[173] T.-L. Ho. Spinor bose condensates in optical traps. *Phys. Rev. Lett.*, 81:742–745, Jul 1998.

[174] M. Hoefer, J. Chang, C. Hamner, and P. Engels. Dark-dark solitons and modulational instability in miscible two-component bose-einstein condensates. *Physical Review A*, 84(4):041605, 2011.

[175] S. Hofferberth, I. Lesanovsky, B. Fischer, T. Schumm, and J. Schmiedmayer. Non-equilibrium coherence dynamics in one-dimensional bose gases. *Nature*, 449(7160):324–327, 2007.

[176] P. C. Hohenberg. Existence of long-range order in one and two dimensions. *Phys. Rev.*, 158:383–386, Jun 1967.

[177] P. C. Hohenberg and B. I. Halperin. Theory of dynamic critical phenomena. *Rev. Mod. Phys.*, 49:435–479, Jul 1977.

[178] A. A. Houck, H. E. Türeci, and J. Koch. On-chip quantum simulation with superconducting circuits. *Nature Physics*, 8(4):292–299, 2012.

[179] W. Hu and S. Dodelson. Cosmic microwave background anisotropies. *Annual Review of Astronomy and Astrophysics*, 40(1):171–216, 2002.

[180] W. Hu, N. Sugiyama, and J. Silk. The physics of microwave background anisotropies. *Nature*, 386(6620):37–43, 1997.

[181] W. Hu and M. White. Acoustic signatures in the cosmic microwave background. *The Astrophysical Journal*, 471(1):30, 1996.

[182] W. Hu and M. White. A new test of inflation. *Physical Review Letters*, 77(9):1687, 1996.

[183] K. Huang. *Statistical Mechanics*. John Wiley & Sons, 2 edition, 1987.

[184] C.-L. Hung, V. Gurarie, and C. Chin. From cosmology to cold atoms: observation of sakharov oscillations in a quenched atomic superfluid. *Science*, 341(6151):1213–1215, 2013.

[185] C.-L. Hung, X. Zhang, N. Gemelke, and C. Chin. Observation of scale invariance and universality in two-dimensional bose gases. *Nature*, 470(7333):236–239, 2011.

[186] M. Isoard, A. Kamchatnov, and N. Pavloff. Dispersionless evolution of inviscid nonlinear pulses. *Europhysics Letters*, 129(6):64003, 2020.

[187] M. Isoard, A. M. Kamchatnov, and N. Pavloff. Long-time evolution of pulses in the korteweg–de vries equation in the absence of solitons reexamined: Whitham method. *Phys. Rev. E*, 99:012210, Jan 2019.

[188] M. Isoard, A. M. Kamchatnov, and N. Pavloff. Wave breaking and formation of dispersive shock waves in a defocusing nonlinear optical material. *Phys. Rev. A*, 99:053819, May 2019.

[189] S. K. Ivanov, J.-E. Suchorski, A. M. Kamchatnov, M. Isoard, and N. Pavloff. Formation of dispersive shock waves in a saturable nonlinear medium. *Phys. Rev. E*, 102:032215, Sep 2020.

[190] T. Jacobson. Introduction to quantum fields in curved spacetime and the hawking effect. *Lectures on quantum gravity*, page 39, 2006.

[191] P. Jain, S. Weinfurtner, M. Visser, and C. Gardiner. Analog model of a friedmann-robertson-walker universe in bose-einstein condensates: Application of the classical field method. *Physical Review A*, 76(3):033616, 2007.

[192] J.-C. Jaskula, G. B. Partridge, M. Bonneau, R. Lopes, J. Ruaudel, D. Boiron, and C. I. Westbrook. Acoustic analog to the dynamical casimir effect in a bose-einstein condensate. *Physical Review Letters*, 109(22):220401, 2012.

[193] A. Jeffrey and T. Taniuti. Non-linear wave propagation with applications to physics and magnetohydrodynamics academic press. *New York and London*, 1964.

[194] A. Jelić and L. F. Cugliandolo. Quench dynamics of the 2d xy model. *Journal of Statistical Mechanics: Theory and Experiment*, 2011(02):P02032, 2011.

[195] D. M. Jezek and P. Capuzzi. Interaction-driven effects on two-component bose-einstein condensates. *Phys. Rev. A*, 66:015602, Jul 2002.

[196] N. Jia, N. Schine, A. Georgakopoulos, A. Ryou, L. W. Clark, A. Sommer, and J. Simon. A strongly interacting polaritonic quantum dot. *Nature Physics*, 14(6):550–554, 2018.

[197] S. Jia, W. Wan, and J. W. Fleischer. Dispersive shock waves in nonlinear arrays. *Phys. Rev. Lett.*, 99:223901, Nov 2007.

[198] D. Jin, J. Ensher, M. Matthews, C. Wieman, and E. A. Cornell. Collective excitations of a bose-einstein condensate in a dilute gas. *Physical review letters*, 77(3):420, 1996.

[199] J. Joseph, E. Elliott, and J. Thomas. Shear viscosity of a unitary fermi gas near the superfluid phase transition. *Physical Review Letters*, 115(2):020401, 2015.

[200] J. Joseph, J. E. Thomas, M. Kulkarni, and A. G. Abanov. Observation of shock waves in a strongly interacting fermi gas. *Physical review letters*, 106(15):150401, 2011.

[201] G. Jotzu, M. Messer, R. Desbuquois, M. Lebrat, T. Uehlinger, D. Greif, and T. Esslinger. Experimental realization of the topological haldane model with ultracold fermions. *Nature*, 515(7526):237–240, 2014.

[202] Y. Kagan, E. Surkov, and G. Shlyapnikov. Evolution of a bose-condensed gas under variations of the confining potential. *Physical Review A*, 54(3):R1753, 1996.

[203] A. M. Kamchatnov. *Nonlinear periodic waves and their modulations: an introductory course*. World Scientific, 2000.

[204] A. M. Kamchatnov. Dispersive shock wave theory for nonintegrable equations. *Phys. Rev. E*, 99:012203, Jan 2019.

[205] P. Kapitza. Viscosity of liquid helium below the λ-point. *Nature*, 141(3558):74–74, 1938.

[206] J. Kasprzak, M. Richard, S. Kundermann, A. Baas, P. Jeambrun, J. M. J. Keeling, F. Marchetti, M. Szymańska, R. André, J. Staehli, et al. Bose–einstein condensation of exciton polaritons. *Nature*, 443(7110):409–414, 2006.

[207] R. M. Kerr. Vortex stretching as a mechanism for quantum kinetic energy decay. *Phys. Rev. Lett.*, 106:224501, Jun 2011.

[208] W. Ketterle and N. V. Druten. Evaporative cooling of trapped atoms. volume 37 of *Advances In Atomic, Molecular, and Optical Physics*, pages 181–236. Academic Press, 1996.

[209] P. G. Kevrekidis, D. J. Frantzeskakis, and R. Carretero-González. *Emergent nonlinear phenomena in Bose-Einstein condensates: theory and experiment*, volume 45. Springer, 2008.

[210] T. W. B. Kibble. Topology of cosmic domains and strings. *Journal of Physics A: Mathematical and General*, 9(8):1387, aug 1976.

[211] S. Kida and M. Takaoka. Vortex reconnection. *Annual Review of Fluid Mechanics*, 26(1):169–177, 1994.

[212] B. Kim, K.-T. Chen, S.-S. Hsiao, S.-Y. Wang, K.-B. Li, J. Ruseckas, G. Juzeliūnas, T. Kirova, M. Auzinsh, Y.-C. Chen, et al. A weakly-interacting many-body system of rydberg polaritons based on electromagnetically induced transparency. *Communications Physics*, 4(1):101, 2021.

[213] J. H. Kim, S. W. Seo, and Y.-i. Shin. Critical spin superflow in a spinor bose-einstein condensate. *Physical Review Letters*, 119(18):185302, 2017.

[214] T. Kinoshita, T. Wenger, and D. S. Weiss. A quantum newton's cradle. *Nature*, 440(7086):900–903, 2006.

[215] D. Kivotides, J. C. Vassilicos, D. C. Samuels, and C. F. Barenghi. Kelvin waves cascade in superfluid turbulence. *Phys. Rev. Lett.*, 86:3080–3083, Apr 2001.

[216] Y. S. Kivshar and G. P. Agrawal. *Optical solitons: from fibers to photonic crystals*. Academic press, 2003.

[217] J. Klaers, J. Schmitt, F. Vewinger, and M. Weitz. Bose–einstein condensation of photons in an optical microcavity. *Nature*, 468(7323):545–548, 2010.

[218] D. Kleckner, L. H. Kauffman, and W. T. Irvine. How superfluid vortex knots untie. *Nature Physics*, 12(7):650–655, 2016.

[219] S. Knoop, T. Schuster, R. Scelle, A. Trautmann, J. Appmeier, M. K. Oberthaler, E. Tiesinga, and E. Tiemann. Feshbach spectroscopy and analysis of the interaction potentials of ultracold sodium. *Phys. Rev. A*, 83:042704, Apr 2011.

[220] M. Koch, C. Sames, M. Balbach, H. Chibani, A. Kubanek, K. Murr, T. Wilk, and G. Rempe. Three-photon correlations in a strongly driven atom-cavity system. *Physical review letters*, 107(2):023601, 2011.

[221] Y. Kodama. The whitham equations for optical communications: Mathematical theory of nrz. *SIAM Journal on Applied Mathematics*, 59(6):2162–2192, 1999.

[222] V. Kohnle, Y. Léger, M. Wouters, M. Richard, M. T. Portella-Oberli, and B. Deveaud-Plédran. From single particle to superfluid excitations in a dissipative polariton gas. *Physical review letters*, 106(25):255302, 2011.

[223] C. Kohstall, S. Riedl, E. R. S. Guajardo, L. A. Sidorenkov, J. H. Denschlag, and R. Grimm. Observation of interference between two molecular bose–einstein condensates. *New Journal of Physics*, 13(6):065027, jun 2011.

[224] M. Kollar, F. A. Wolf, and M. Eckstein. Generalized gibbs ensemble prediction of prethermalization plateaus and their relation to nonthermal steady states in integrable systems. *Phys. Rev. B*, 84:054304, Aug 2011.

[225] S. Koller, A. Groot, P. Bons, R. Duine, H. Stoof, and P. van der Straten. Quantum enhancement of spin drag in a bose gas. *New Journal of Physics*, 17(11):113026, 2015.

[226] S. Komineas and N. Papanicolaou. Solitons, solitonic vortices, and vortex rings in a confined bose-einstein condensate. *Phys. Rev. A*, 68:043617, Oct 2003.

[227] J. Koplik and H. Levine. Vortex reconnection in superfluid helium. *Phys. Rev. Lett.*, 71:1375–1378, Aug 1993.

[228] M. Koschorreck, D. Pertot, E. Vogt, and M. Köhl. Universal spin dynamics in two-dimensional fermi gases. *Nature Physics*, 9(7):405–409, 2013.

[229] J. M. Kosterlitz and D. J. Thouless. Ordering, metastability and phase transitions in two-dimensional systems. *Journal of Physics C: Solid State Physics*, 6(7):1181, apr 1973.

[230] E. Kozik and B. Svistunov. Kelvin-wave cascade and decay of superfluid turbulence. *Phys. Rev. Lett.*, 92:035301, Jan 2004.

[231] E. Kozik and B. Svistunov. Scale-separation scheme for simulating superfluid turbulence: Kelvin-wave cascade. *Phys. Rev. Lett.*, 94:025301, Jan 2005.

[232] K. Krupa, A. Tonello, B. M. Shalaby, M. Fabert, A. Barthélémy, G. Millot, S. Wabnitz, and V. Couderc. Spatial beam self-cleaning in multimode fibres. *Nature Photonics*, 11(4):237–241, 2017.

[233] A. Krylov, V. Khodorovskii, G. El, and D. PARSONS. Evolution of a nonmonotonic perturbation in korteweg-de-vries hydrodynamics. *JETP letters*, 56(6):323–327, 1992.

[234] M. J. H. Ku, W. Ji, B. Mukherjee, E. Guardado-Sanchez, L. W. Cheuk, T. Yefsah, and M. W. Zwierlein. Motion of a solitonic vortex in the bec-bcs crossover. *Phys. Rev. Lett.*, 113:065301, Aug 2014.

[235] M. J. H. Ku, B. Mukherjee, T. Yefsah, and M. W. Zwierlein. Cascade of solitonic excitations in a superfluid fermi gas: From planar solitons to vortex rings and lines. *Phys. Rev. Lett.*, 116:045304, Jan 2016.

[236] A. Kubanek, A. Ourjoumtsev, I. Schuster, M. Koch, P. W. Pinkse, K. Murr, and G. Rempe. Two-photon gateway in one-atom cavity quantum electrodynamics. *Physical Review Letters*, 101(20):203602, 2008.

[237] C. Kurtscheid, D. Dung, E. Busley, F. Vewinger, A. Rosch, and M. Weitz. Thermally condensing photons into a coherently split state of light. *Science*, 366(6467):894–897, 2019.

[238] H. Lacombe. Courants de densité dans le détroit de gibraltar. *La Houille Blanche*, (1):38–44, 1965.

[239] Y. Lai and H. Haus. Quantum theory of solitons in optical fibers. i. time-dependent hartree approximation. *Physical review A*, 40(2):844, 1989.

[240] G. Lamporesi, S. Donadello, S. Serafini, F. Dalfovo, and G. Ferrari. Spontaneous creation of kibble–zurek solitons in a bose–einstein condensate. *Nature Physics*, 9(10):656–660, 2013.

[241] L. Landau and E. Lifshitz. Electrodynamics of continuous media, 2nd edn course of theoretical physics, vol. 8 new york. *NY: Pergamon Press.[Google Scholar]*, 1984.

[242] T. Langen, S. Erne, R. Geiger, B. Rauer, T. Schweigler, M. Kuhnert, W. Rohringer, I. E. Mazets, T. Gasenzer, and J. Schmiedmayer. Experimental observation of a generalized gibbs ensemble. *Science*, 348(6231):207–211, 2015.

[243] T. Langen, R. Geiger, M. Kuhnert, B. Rauer, and J. Schmiedmayer. Local emergence of thermal correlations in an isolated quantum many-body system. *Nature Physics*, 9(10):640–643, 2013.

[244] P.-E. Larre, S. Biasi, F. Ramiro-Manzano, L. Pavesi, and I. Carusotto. Pump-and-probe optical transmission phase shift as a quantitative probe of the bogoliubov dispersion relation in a nonlinear channel waveguide. *The European Physical Journal D*, 71:1–17, 2017.

[245] P.-É. Larré and I. Carusotto. Optomechanical signature of a frictionless flow of superfluid light. *Physical Review A*, 91(5):053809, 2015.

[246] P.-E. Larré, D. Delande, and N. Cherroret. Postquench prethermalization in a disordered quantum fluid of light. *Phys. Rev. A*, 97:043805, Apr 2018.

[247] M. Leadbeater, T. Winiecki, D. C. Samuels, C. F. Barenghi, and C. S. Adams. Sound emission due to superfluid vortex reconnections. *Phys. Rev. Lett.*, 86:1410–1413, Feb 2001.

[248] K. L. Lee, N. B. Jørgensen, I.-K. Liu, L. Wacker, J. J. Arlt, and N. P. Proukakis. Phase separation and dynamics of two-component bose-einstein condensates. *Phys. Rev. A*, 94:013602, Jul 2016.

[249] A. J. Leggett. *Quantum liquids: Bose condensation and Cooper pairing in condensed-matter systems*. Oxford university press, 2006.

[250] G. Lerario, A. Fieramosca, F. Barachati, D. Ballarini, K. S. Daskalakis, L. Dominici, M. De Giorgi, S. A. Maier, G. Gigli, S. Kéna-Cohen, et al. Room-temperature superfluidity in a polariton condensate. *Nature Physics*, 13(9):837–841, 2017.

[251] Q.-Y. Liang, A. V. Venkatramani, S. H. Cantu, T. L. Nicholson, M. J. Gullans, A. V. Gorshkov, J. D. Thompson, C. Chin, M. D. Lukin, and V. Vuletić. Observation of three-photon bound states in a quantum nonlinear medium. *Science*, 359(6377):783–786, 2018.

[252] A. D. Linde. A new inflationary universe scenario: a possible solution of the horizon, flatness, homogeneity, isotropy and primordial monopole problems. *Physics Letters B*, 108(6):389–393, 1982.

[253] I.-K. Liu, S. Donadello, G. Lamporesi, G. Ferrari, S.-C. Gou, F. Dalfovo, and N. Proukakis. Dynamical equilibration across a quenched phase transition in a trapped quantum gas. *Communications Physics*, 1(1):24, 2018.

[254] C. Luciuk, S. Smale, F. Böttcher, H. Sharum, B. Olsen, S. Trotzky, T. Enss, and J. Thywissen. Observation of quantum-limited spin transport in strongly interacting two-dimensional fermi gases. *Physical Review Letters*, 118(13):130405, 2017.

[255] M. D. Lukin, M. Fleischhauer, R. Cote, L. Duan, D. Jaksch, J. I. Cirac, and P. Zoller. Dipole blockade and quantum information processing in mesoscopic atomic ensembles. *Physical review letters*, 87(3):037901, 2001.

[256] E. Lundh and P. Ao. Hydrodynamic approach to vortex lifetimes in trapped bose condensates. *Phys. Rev. A*, 61:063612, May 2000.

[257] R. Ma, B. Saxberg, C. Owens, N. Leung, Y. Lu, J. Simon, and D. I. Schuster. A dissipatively stabilized mott insulator of photons. *Nature*, 566(7742):51–57, 2019.

[258] P. Maddaloni, M. Modugno, C. Fort, F. Minardi, and M. Inguscio. Collective oscillations of two colliding bose-einstein condensates. *Phys. Rev. Lett.*, 85:2413–2417, Sep 2000.

[259] K. W. Madison, F. Chevy, W. Wohlleben, and J. Dalibard. Vortex formation in a stirred bose-einstein condensate. *Phys. Rev. Lett.*, 84:806–809, Jan 2000.

[260] K. Mallayya, M. Rigol, and W. De Roeck. Prethermalization and thermalization in isolated quantum systems. *Phys. Rev. X*, 9:021027, May 2019.

[261] G. I. Martone, P.-E. Larré, A. Fabbri, and N. Pavloff. Momentum distribution and coherence of a weakly interacting bose gas after a quench. *Phys. Rev. A*, 98:063617, Dec 2018.

[262] L. Mathey and A. Polkovnikov. Light cone dynamics and reverse kibble-zurek mechanism in two-dimensional superfluids following a quantum quench. *Phys. Rev. A*, 81:033605, Mar 2010.

[263] M. R. Matthews, B. P. Anderson, P. C. Haljan, D. S. Hall, C. E. Wieman, and E. A. Cornell. Vortices in a bose-einstein condensate. *Phys. Rev. Lett.*, 83:2498–2501, Sep 1999.

[264] J. Maurer and P. Tabeling. Local investigation of superfluid turbulence. *Europhysics Letters*, 43(1):29, jul 1998.

[265] Y. Mei, Y. Li, H. Nguyen, P. Berman, and A. Kuzmich. Trapped alkali-metal rydberg qubit. *Physical Review Letters*, 128(12):123601, 2022.

[266] N. D. Mermin and H. Wagner. Absence of ferromagnetism or antiferromagnetism in one- or two-dimensional isotropic heisenberg models. *Phys. Rev. Lett.*, 17:1133–1136, Nov 1966.

[267] K. M. Mertes, J. W. Merrill, R. Carretero-González, D. J. Frantzeskakis, P. G. Kevrekidis, and D. S. Hall. Nonequilibrium dynamics and superfluid ring excitations in binary bose-einstein condensates. *Phys. Rev. Lett.*, 99:190402, Nov 2007.

[268] M.-O. Mewes, M. Andrews, N. Van Druten, D. Kurn, D. Durfee, C. Townsend, and W. Ketterle. Collective excitations of a bose-einstein condensate in a magnetic trap. *Physical review letters*, 77(6):988, 1996.

[269] C. Michel, O. Boughdad, M. Albert, P.-É. Larré, and M. Bellec. Superfluid motion and drag-force cancellation in a fluid of light. *Nature communications*, 9(1):2108, 2018.

[270] P. Michler, A. Kiraz, C. Becher, W. Schoenfeld, P. Petroff, L. Zhang, E. Hu, and A. Imamoglu. A quantum dot single-photon turnstile device. *science*, 290(5500):2282–2285, 2000.

[271] S. Middelkamp, P. J. Torres, P. G. Kevrekidis, D. J. Frantzeskakis, R. Carretero-González, P. Schmelcher, D. V. Freilich, and D. S. Hall. Guiding-center dynamics of vortex dipoles in bose-einstein condensates. *Phys. Rev. A*, 84:011605, Jul 2011.

[272] G. Modugno, M. Modugno, F. Riboli, G. Roati, and M. Inguscio. Two atomic species superfluid. *Phys. Rev. Lett.*, 89:190404, Oct 2002.

[273] M. Modugno, F. Dalfovo, C. Fort, P. Maddaloni, and F. Minardi. Dynamics of two colliding bose-einstein condensates in an elongated magnetostatic trap. *Phys. Rev. A*, 62:063607, Nov 2000.

[274] M. Modugno, C. Fort, P. Maddaloni, F. Minardi, and M. Inguscio. Damping and frequency shift in the oscillations of two colliding bose-einstein condensates. *The European Physical Journal D-Atomic, Molecular, Optical and Plasma Physics*, 17:345–349, 2001.

[275] D. Møller, L. B. Madsen, and K. Mølmer. Quantum gates and multiparticle entanglement by rydberg excitation blockade and adiabatic passage. *Physical review letters*, 100(17):170504, 2008.

[276] R. Monaco, J. Mygind, R. J. Rivers, and V. P. Koshelets. Spontaneous fluxoid formation in superconducting loops. *Phys. Rev. B*, 80:180501, Nov 2009.

[277] G. T. Moore. Quantum theory of the electromagnetic field in a variable-length one-dimensional cavity. *Journal of Mathematical Physics*, 11(9):2679–2691, 1970.

[278] C. Mora and Y. Castin. Extension of bogoliubov theory to quasicondensates. *Phys. Rev. A*, 67:053615, May 2003.

[279] T. Mori, T. N. Ikeda, E. Kaminishi, and M. Ueda. Thermalization and prethermalization in isolated quantum systems: a theoretical overview. *Journal of Physics B: Atomic, Molecular and Optical Physics*, 51(11):112001, 2018.

[280] S. Moulder, S. Beattie, R. P. Smith, N. Tammuz, and Z. Hadzibabic. Quantized supercurrent decay in an annular bose-einstein condensate. *Phys. Rev. A*, 86:013629, Jul 2012.

[281] V. F. Mukhanov, H. A. Feldman, and R. H. Brandenberger. Theory of cosmological perturbations. *Physics reports*, 215(5-6):203–333, 1992.

[282] J. Mur-Petit, M. Guilleumas, A. Polls, A. Sanpera, M. Lewenstein, K. Bongs, and K. Sengstock. Dynamics of f= 1 rb 87 condensates at finite temperatures. *Physical Review A*, 73(1):013629, 2006.

[283] P. A. Murthy, I. Boettcher, L. Bayha, M. Holzmann, D. Kedar, M. Neidig, M. G. Ries, A. N. Wenz, G. Zürn, and S. Jochim. Observation of the berezinskii-kosterlitz-thouless phase transition in an ultracold fermi gas. *Phys. Rev. Lett.*, 115:010401, Jun 2015.

[284] C. J. Myatt, E. A. Burt, R. W. Ghrist, E. A. Cornell, and C. E. Wieman. Production of two overlapping bose-einstein condensates by sympathetic cooling. *Phys. Rev. Lett.*, 78:586–589, Jan 1997.

[285] S. Nascimbène, N. Navon, K. Jiang, F. Chevy, and C. Salomon. Exploring the thermodynamics of a universal fermi gas. *Nature*, 463(7284):1057–1060, 2010.

[286] S. Nascimbene, N. Navon, K. Jiang, L. Tarruell, M. Teichmann, J. Mckeever, F. Chevy, and C. Salomon. Collective oscillations of an imbalanced fermi gas: axial compression modes and polaron effective mass. *Physical review letters*, 103(17):170402, 2009.

[287] C. M. Nascimento, M. A. Alencar, S. Chávez-Cerda, M. G. da Silva, M. R. Meneghetti, and J. M. Hickmann. Experimental demonstration of novel effects on the far-field diffraction patterns of a gaussian beam in a kerr medium. *Journal of Optics A: Pure and Applied Optics*, 8(11):947, 2006.

[288] R. Navarro, R. Carretero-González, P. J. Torres, P. G. Kevrekidis, D. J. Frantzeskakis, M. W. Ray, E. Altuntaş, and D. S. Hall. Dynamics of a few corotating vortices in bose-einstein condensates. *Phys. Rev. Lett.*, 110:225301, May 2013.

[289] N. Navon, A. L. Gaunt, R. P. Smith, and Z. Hadzibabic. Emergence of a turbulent cascade in a quantum gas. *Nature*, 539(7627):72–75, 2016.

[290] S. Nazarenko and R. West. Analytical solution for nonlinear schrödinger vortex reconnection. *Journal of low temperature physics*, 132:1–10, 2003.

[291] M. Neeley, M. Ansmann, R. C. Bialczak, M. Hofheinz, E. Lucero, A. D. O'Connell, D. Sank, H. Wang, J. Wenner, A. N. Cleland, et al. Emulation of a quantum spin with a superconducting phase qudit. *Science*, 325(5941):722–725, 2009.

[292] T. W. Neely, E. C. Samson, A. S. Bradley, M. J. Davis, and B. P. Anderson. Observation of vortex dipoles in an oblate bose-einstein condensate. *Phys. Rev. Lett.*, 104:160401, Apr 2010.

[293] D. R. Nelson and J. M. Kosterlitz. Universal jump in the superfluid density of two-dimensional superfluids. *Phys. Rev. Lett.*, 39:1201–1205, Nov 1977.

[294] C. Netterfield, P. A. Ade, J. J. Bock, J. Bond, J. Borrill, A. Boscaleri, K. Coble, C. Contaldi, B. Crill, P. De Bernardis, et al. A measurement by boomerang of multiple peaks in the angular power spectrum of the cosmic microwave background. *The Astrophysical Journal*, 571(2):604, 2002.

[295] E. Nicklas, W. Muessel, H. Strobel, P. G. Kevrekidis, and M. K. Oberthaler. Nonlinear dressed states at the miscibility-immiscibility threshold. *Phys. Rev. A*, 92:053614, Nov 2015.

[296] E. Nicklas, H. Strobel, T. Zibold, C. Gross, B. A. Malomed, P. G. Kevrekidis, and M. K. Oberthaler. Rabi flopping induces spatial demixing dynamics. *Phys. Rev. Lett.*, 107:193001, Nov 2011.

[297] C. Nore, M. Abid, and M. E. Brachet. Kolmogorov turbulence in low-temperature superflows. *Phys. Rev. Lett.*, 78:3896–3899, May 1997.

[298] J. Nuño, C. Finot, G. Xu, G. Millot, M. Erkintalo, and J. Fatome. Vectorial dispersive shock waves in optical fibers. *Communications Physics*, 2(1):138, 2019.

[299] T. Ohmi and K. Machida. Bose-einstein condensation with internal degrees of freedom in alkali atom gases. *Journal of the Physical Society of Japan*, 67(6):1822–1825, 1998.

[300] R. Onofrio, C. Raman, J. Vogels, J. Abo-Shaeer, A. Chikkatur, and W. Ketterle. Observation of superfluid flow in a bose-einstein condensed gas. *Physical review letters*, 85(11):2228, 2000.

[301] L. Onsager. Statistical hydrodynamics. *Il Nuovo Cimento (1943-1954)*, 6(Suppl 2):279–287, 1949.

[302] L. Ovsyannikov. Two-layer "shallow water" model. *Journal of Applied Mechanics and Technical Physics*, 20(2):127–135, 1979.

[303] T. Ozawa, H. M. Price, A. Amo, N. Goldman, M. Hafezi, L. Lu, M. C. Rechtsman, D. Schuster, J. Simon, O. Zilberberg, et al. Topological photonics. *Reviews of Modern Physics*, 91(1):015006, 2019.

[304] R. E. Packard and S. Vitale. Principles of superfluid-helium gyroscopes. *Phys. Rev. B*, 46:3540–3549, Aug 1992.

[305] G. Pagano, M. Mancini, G. Cappellini, P. Lombardi, F. Schäfer, H. Hu, X.-J. Liu, J. Catani, C. Sias, M. Inguscio, et al. A one-dimensional liquid of fermions with tunable spin. *Nature Physics*, 10(3):198–201, 2014.

[306] B. Paredes, A. Widera, V. Murg, O. Mandel, S. Fölling, I. Cirac, G. V. Shlyapnikov, T. W. Hänsch, and I. Bloch. Tonks–girardeau gas of ultracold atoms in an optical lattice. *Nature*, 429(6989):277–281, 2004.

[307] L. Parker. Particle creation in expanding universes. *Physical Review Letters*, 21(8):562, 1968.

[308] L. Parker. Particle creation in isotropic cosmologies. *Physical Review Letters*, 28(11):705, 1972.

[309] P. J. Peebles and J. Yu. Primeval adiabatic perturbation in an expanding universe. *The Astrophysical Journal*, 162:815, 1970.

[310] M. Pelton, C. Santori, J. Vucković, B. Zhang, G. S. Solomon, J. Plant, and Y. Yamamoto. Efficient source of single photons: a single quantum dot in a micropost microcavity. *Physical review letters*, 89(23):233602, 2002.

[311] U.-L. Pen, U. Seljak, and N. Turok. Power spectra in global defect theories of cosmic structure formation. *Physical Review Letters*, 79(9):1611, 1997.

[312] C. J. Pethick and H. Smith. *Bose–Einstein Condensation in Dilute Gases*. Cambridge University Press, 2001.

[313] D. S. Petrov, M. Holzmann, and G. V. Shlyapnikov. Bose-einstein condensation in quasi-2d trapped gases. *Phys. Rev. Lett.*, 84:2551–2555, Mar 2000.

[314] T. Peyronel, O. Firstenberg, Q.-Y. Liang, S. Hofferberth, A. V. Gorshkov, T. Pohl, M. D. Lukin, and V. Vuletić. Quantum nonlinear optics with single photons enabled by strongly interacting atoms. *Nature*, 488(7409):57–60, 2012.

[315] C. Piekarski, W. Liu, J. Steinhauer, E. Giacobino, A. Bramati, and Q. Glorieux. Measurement of the static structure factor in a paraxial fluid of light using bragg-like spectroscopy. *Phys. Rev. Lett.*, 127:023401, Jul 2021.

[316] D. Pines and P. Nozières. Normal fermi liquids (the theory of quantum liquids vol i), 1966.

[317] L. Pitaevskii and S. Stringari. *Bose-Einstein Condensation and Superfluidity*. International Series of Monographs on Physics. OUP Oxford, 2016.

[318] A. Polkovnikov, E. Altman, and E. Demler. Interference between independent fluctuating condensates. *Proceedings of the National Academy of Sciences*, 103(16):6125–6129, 2006.

[319] A. Polkovnikov, K. Sengupta, A. Silva, and M. Vengalattore. Colloquium: Nonequilibrium dynamics of closed interacting quantum systems. *Rev. Mod. Phys.*, 83:863–883, Aug 2011.

[320] A. Prain, S. Fagnocchi, and S. Liberati. Analogue cosmological particle creation: Quantum correlations in expanding bose-einstein condensates. *Physical Review D*, 82(10):105018, 2010.

[321] E. Priest and T. Forbes. Magnetic reconnection: Mhd theory and applications, cambridge univ. *Press, Cambridge*, pages 1–45, 2000.

[322] N. Prokof'ev and B. Svistunov. Two-dimensional weakly interacting bose gas in the fluctuation region. *Phys. Rev. A*, 66:043608, Oct 2002.

[323] M. Prüfer, P. Kunkel, H. Strobel, S. Lannig, D. Linnemann, C.-M. Schmied, J. Berges, T. Gasenzer, and M. K. Oberthaler. Observation of universal dynamics in a spinor bose gas far from equilibrium. *Nature*, 563(7730):217–220, 2018.

[324] H. Pu and N. P. Bigelow. Properties of two-species bose condensates. *Phys. Rev. Lett.*, 80:1130–1133, Feb 1998.

[325] K. Pyka, J. Keller, H. Partner, R. Nigmatullin, T. Burgermeister, D. Meier, K. Kuhlmann, A. Retzker, M. B. Plenio, W. Zurek, et al. Topological defect formation and spontaneous symmetry breaking in ion coulomb crystals. *Nature communications*, 4(1):2291, 2013.

[326] C. Qiu, X. Nie, and D. Lu. Quantum simulations with nuclear magnetic resonance system. *Chinese Physics B*, 30(4):048201, 2021.

[327] C. Qu, L. P. Pitaevskii, and S. Stringari. Magnetic solitons in a binary bose-einstein condensate. *Phys. Rev. Lett.*, 116:160402, Apr 2016.

[328] A. Ramanathan, S. R. Muniz, K. C. Wright, R. P. Anderson, W. D. Phillips, K. Helmerson, and G. K. Campbell. Partial-transfer absorption imaging: A versatile technique for optimal imaging of ultracold gases. *Review of Scientific Instruments*, 83(8):083119, 2012.

[329] A. Recati and S. Stringari. Spin fluctuations, susceptibility, and the dipole oscillation of a nearly ferromagnetic fermi gas. *Phys. Rev. Lett.*, 106:080402, Feb 2011.

[330] C. A. Regal, M. Greiner, and D. S. Jin. Observation of resonance condensation of fermionic atom pairs. *Phys. Rev. Lett.*, 92:040403, Jan 2004.

[331] P. Richerme, Z.-X. Gong, A. Lee, C. Senko, J. Smith, M. Foss-Feig, S. Michalakis, A. V. Gorshkov, and C. Monroe. Non-local propagation of correlations in quantum systems with long-range interactions. *Nature*, 511(7508):198–201, 2014.

[332] B. Riemann. Collected papers, english translation by r. baker, ch. christenson and h. orde, 2004.

[333] G. Roati, C. D'Errico, L. Fallani, M. Fattori, C. Fort, M. Zaccanti, G. Modugno, M. Modugno, and M. Inguscio. Anderson localization of a non-interacting bose–einstein condensate. *Nature*, 453(7197):895–898, 2008.

[334] M. Rodríguez, P. Pedri, P. Törmä, and L. Santos. Scissors modes of two-component degenerate gases: Bose-bose and bose-fermi mixtures. *Physical Review A*, 69(2):023617, 2004.

[335] C. Rorai, J. Skipper, R. M. Kerr, and K. R. Sreenivasan. Approach and separation of quantised vortices with balanced cores. *Journal of Fluid Mechanics*, 808:641–667, 2016.

[336] P. Rosenbusch, V. Bretin, and J. Dalibard. Dynamics of a single vortex line in a bose-einstein condensate. *Phys. Rev. Lett.*, 89:200403, Oct 2002.

[337] J. E. Rothenberg and D. Grischkowsky. Observation of the formation of an optical intensity shock and wave breaking in the nonlinear propagation of pulses in optical fibers. *Phys. Rev. Lett.*, 62:531–534, Jan 1989.

[338] G. Roumpos, M. Lohse, W. H. Nitsche, J. Keeling, M. H. Szymańska, P. B. Littlewood, A. Löffler, S. Höfling, L. Worschech, A. Forchel, et al. Power-law decay of the spatial correlation function in exciton-polariton condensates. *Proceedings of the National Academy of Sciences*, 109(17):6467–6472, 2012.

[339] P. Roushan, C. Neill, A. Megrant, Y. Chen, R. Babbush, R. Barends, B. Campbell, Z. Chen, B. Chiaro, A. Dunsworth, et al. Chiral ground-state currents of interacting photons in a synthetic magnetic field. *Nature Physics*, 13(2):146–151, 2017.

[340] R. Roy, A. Green, R. Bowler, and S. Gupta. Two-element mixture of bose and fermi superfluids. *Phys. Rev. Lett.*, 118:055301, Feb 2017.

[341] W. RuGway, A. G. Manning, S. S. Hodgman, R. G. Dall, A. G. Truscott, T. Lamberton, and K. V. Kheruntsyan. Observation of transverse bose-einstein condensation via hanbury brown–twiss correlations. *Phys. Rev. Lett.*, 111:093601, Aug 2013.

[342] V. Ruutu, V. Eltsov, A. Gill, T. Kibble, M. Krusius, Y. G. Makhlin, B. Placais, G. Volovik, and W. Xu. Vortex formation in neutron-irradiated superfluid 3he as an analogue of cosmological defect formation. *Nature*, 382(6589):334–336, 1996.

[343] C. Ryu, M. F. Andersen, P. Cladé, V. Natarajan, K. Helmerson, and W. D. Phillips. Observation of persistent flow of a bose-einstein condensate in a toroidal trap. *Phys. Rev. Lett.*, 99:260401, Dec 2007.

[344] L. Sadler, J. Higbie, S. Leslie, M. Vengalattore, and D. Stamper-Kurn. Spontaneous symmetry breaking in a quenched ferromagnetic spinor bose–einstein condensate. *Nature*, 443(7109):312–315, 2006.

[345] R. Sagdeev and M. Leontovich. Reviews of plasma physics, 1966.

[346] N. Šantić, A. Fusaro, S. Salem, J. Garnier, A. Picozzi, and R. Kaiser. Nonequilibrium precondensation of classical waves in two dimensions propagating through atomic vapors. *Physical review letters*, 120(5):055301, 2018.

[347] A. Sartori, J. Marino, S. Stringari, and A. Recati. Spin-dipole oscillation and relaxation of coherently coupled bose–einstein condensates. *New Journal of Physics*, 17(9):093036, 2015.

[348] A. Sartori and A. Recati. Dynamics of highly unbalanced bose-bose mixtures: miscible vs. immiscible gases. *The European Physical Journal D*, 67:1–7, 2013.

[349] K. Sato. Cosmological baryon-number domain structure and the first order phase transition of a vacuum. *Physics Letters B*, 99(1):66–70, 1981.

[350] B. Saxberg, A. Vrajitoarea, G. Roberts, M. G. Panetta, J. Simon, and D. I. Schuster. Disorder-assisted assembly of strongly correlated fluids of light. *Nature*, 612(7940):435–441, 2022.

[351] M. W. Scheeler, D. Kleckner, D. Proment, G. L. Kindlmann, and W. T. Irvine. Helicity conservation by flow across scales in reconnecting vortex links and knots. *Proceedings of the National Academy of Sciences*, 111(43):15350–15355, 2014.

[352] R. Schley, A. Berkovitz, S. Rinott, I. Shammass, A. Blumkin, and J. Steinhauer. Planck distribution of phonons in a bose-einstein condensate. *Physical review letters*, 111(5):055301, 2013.

[353] H. Schmaljohann, M. Erhard, J. Kronjäger, M. Kottke, S. Van Staa, L. Cacciapuoti, J. Arlt, K. Bongs, and K. Sengstock. Dynamics of f= 2 spinor bose-einstein condensates. *Physical review letters*, 92(4):040402, 2004.

[354] C. Schneider, K. Winkler, M. D. Fraser, M. Kamp, Y. Yamamoto, E. Ostrovskaya, and S. Höfling. Exciton-polariton trapping and potential landscape engineering. *Reports on Progress in Physics*, 80(1):016503, 2016.

[355] E. Schrödinger. The proper vibrations of the expanding universe. *Physica*, 6(7-12):899–912, 1939.

[356] B. Schwartz, S. Foner, and N. A. T. O. S. A. Division. *Superconductor Applications: SQUIDs and Machines*. NATO ASI series: Physics. Springer US, 1977.

[357] K. W. Schwarz. Three-dimensional vortex dynamics in superfluid ^{4}He: Homogeneous superfluid turbulence. *Phys. Rev. B*, 38:2398–2417, Aug 1988.

[358] T. Scoquart, P.-É. Larré, D. Delande, and N. Cherroret. Weakly interacting disordered bose gases out of equilibrium: From multiple scattering to superfluidity (a). *Europhysics Letters*, 132(6):66001, 2021.

[359] S. Serafini, M. Barbiero, M. Debortoli, S. Donadello, F. Larcher, F. Dalfovo, G. Lamporesi, and G. Ferrari. Dynamics and interaction of vortex lines in an elongated bose-einstein condensate. *Phys. Rev. Lett.*, 115:170402, Oct 2015.

[360] D. E. Sheehy and L. Radzihovsky. Vortices in spatially inhomogeneous superfluids. *Phys. Rev. A*, 70:063620, Dec 2004.

[361] J. F. Sherson, C. Weitenberg, M. Endres, M. Cheneau, I. Bloch, and S. Kuhr. Single-atom-resolved fluorescence imaging of an atomic mott insulator. *Nature*, 467(7311):68–72, 2010.

[362] Y.-i. Shin, C. H. Schunck, A. Schirotzek, and W. Ketterle. Phase diagram of a two-component fermi gas with resonant interactions. *Nature*, 451(7179):689–693, 2008.

[363] L. A. Sidorenkov, M. K. Tey, R. Grimm, Y.-H. Hou, L. Pitaevskii, and S. Stringari. Second sound and the superfluid fraction in a fermi gas with resonant interactions. *Nature*, 498(7452):78–81, 2013.

[364] A. H. Silver and J. E. Zimmerman. Quantum states and transitions in weakly connected superconducting rings. *Phys. Rev.*, 157:317–341, May 1967.

[365] A. Sinatra, P. O. Fedichev, Y. Castin, J. Dalibard, and G. V. Shlyapnikov. Dynamics of two interacting bose-einstein condensates. *Phys. Rev. Lett.*, 82:251–254, Jan 1999.

[366] G. Situ and J. W. Fleischer. Dynamics of the berezinskii–kosterlitz–thouless transition in a photon fluid. *Nature Photonics*, 14(8):517–522, 2020.

[367] L. Skrbek and K. Sreenivasan. Developed quantum turbulence and its decay. *Physics of Fluids*, 24(1):011301, 2012.

[368] J. Smith, A. Lee, P. Richerme, B. Neyenhuis, P. W. Hess, P. Hauke, M. Heyl, D. A. Huse, and C. Monroe. Many-body localization in a quantum simulator with programmable random disorder. *Nature Physics*, 12(10):907–911, 2016.

[369] G. F. Smoot, C. L. Bennett, A. Kogut, E. Wright, J. Aymon, N. Boggess, E. Cheng, G. De Amici, S. Gulkis, M. Hauser, et al. Structure in the cobe differential microwave radiometer first-year maps. *Astrophysical Journal, Part 2-Letters (ISSN 0004-637X), vol. 396, no. 1, Sept. 1, 1992, p. L1-L5. Research supported by NASA.*, 396:L1–L5, 1992.

[370] A. Sommer, M. Ku, G. Roati, and M. W. Zwierlein. Universal spin transport in a strongly interacting fermi gas. *Nature*, 472(7342):201–204, 2011.

[371] E. Sonin. Spin currents and spin superfluidity. *Advances in Physics*, 59(3):181–255, 2010.

[372] D. M. Stamper-Kurn and M. Ueda. Spinor bose gases: Symmetries, magnetism, and quantum dynamics. *Rev. Mod. Phys.*, 85:1191–1244, Jul 2013.

[373] A. Starobinskii. Spectrum of relict gravitational radiation and the early state of the universe. *JETP Letters*, 30(11):682–685, 1979.

[374] J. Steinhauer, R. Ozeri, N. Katz, and N. Davidson. Excitation spectrum of a bose-einstein condensate. *Physical review letters*, 88(12):120407, 2002.

[375] J. Stenger, S. Inouye, D. Stamper-Kurn, H.-J. Miesner, A. Chikkatur, and W. Ketterle. Spin domains in ground-state bose–einstein condensates. *Nature*, 396(6709):345–348, 1998.

[376] S. Stringari. Collective excitations of a trapped bose-condensed gas. *Phys. Rev. Lett.*, 77:2360–2363, Sep 1996.

[377] D. W. Sumners. Lifting the curtain: Using topology to probe the hidden action of enzymes. *Notices of the American Mathematical Society*, 42(5):528–537, 1995.

[378] C. Sun, S. Jia, C. Barsi, S. Rica, A. Picozzi, and J. W. Fleischer. Observation of the kinetic condensation of classical waves. *Nature Physics*, 8(6):470–474, 2012.

[379] A. A. Svidzinsky and A. L. Fetter. Stability of a vortex in a trapped bose-einstein condensate. *Phys. Rev. Lett.*, 84:5919–5923, Jun 2000.

[380] Y. Tang, W. Kao, K.-Y. Li, S. Seo, K. Mallayya, M. Rigol, S. Gopalakrishnan, and B. L. Lev. Thermalization near integrability in a dipolar quantum newton's cradle. *Phys. Rev. X*, 8:021030, May 2018.

[381] L. Tanzi, E. Lucioni, F. Famà, J. Catani, A. Fioretti, C. Gabbanini, R. N. Bisset, L. Santos, and G. Modugno. Observation of a dipolar quantum gas with metastable supersolid properties. *Phys. Rev. Lett.*, 122:130405, Apr 2019.

[382] R. Tebbs, A. J. Youd, and C. F. Barenghi. The approach to vortex reconnection. *Journal of Low Temperature Physics*, 162:314–321, 2011.

[383] E. Timmermans. Phase separation of bose-einstein condensates. *Phys. Rev. Lett.*, 81:5718–5721, Dec 1998.

[384] P. Torres, P. Kevrekidis, D. Frantzeskakis, R. Carretero-González, P. Schmelcher, and D. Hall. Dynamics of vortex dipoles in confined bose–einstein condensates. *Physics Letters A*, 375(33):3044–3050, 2011.

[385] A. Trabesinger. Quantum simulation. *Nature Physics*, 8(4):263–263, 2012.

[386] S. Trotzky, Y.-A. Chen, A. Flesch, I. P. McCulloch, U. Schollwöck, J. Eisert, and I. Bloch. Probing the relaxation towards equilibrium in an isolated strongly correlated one-dimensional bose gas. *Nature physics*, 8(4):325–330, 2012.

[387] M. C. Tsatsos, P. E. Tavares, A. Cidrim, A. R. Fritsch, M. A. Caracanhas, F. E. A. dos Santos, C. F. Barenghi, and V. S. Bagnato. Quantum turbulence in trapped atomic bose–einstein condensates. *Physics Reports*, 622:1–52, 2016.

[388] S. Tung, G. Lamporesi, D. Lobser, L. Xia, and E. A. Cornell. Observation of the presuperfluid regime in a two-dimensional bose gas. *Phys. Rev. Lett.*, 105:230408, Dec 2010.

[389] M. Tylutki, S. Donadello, S. Serafini, L. P. Pitaevskii, F. Dalfovo, G. Lamporesi, and G. Ferrari. Solitonic vortices in bose–einstein condensates. *The European Physical Journal Special Topics*, 224:577–583, 2015.

[390] S. Ulm, J. Roßnagel, G. Jacob, C. Degünther, S. Dawkins, U. Poschinger, R. Nigmatullin, A. Retzker, M. Plenio, F. Schmidt-Kaler, et al. Observation of the kibble–zurek scaling law for defect formation in ion crystals. *Nature communications*, 4(1):2290, 2013.

[391] S. Utsunomiya, L. Tian, G. Roumpos, C. Lai, N. Kumada, T. Fujisawa, M. Kuwata-Gonokami, A. Löffler, S. Höfling, A. Forchel, et al. Observation of bogoliubov excitations in exciton-polariton condensates. *Nature Physics*, 4(9):700–705, 2008.

[392] G. Valtolina, F. Scazza, A. Amico, A. Burchianti, A. Recati, T. Enss, M. Inguscio, M. Zaccanti, and G. Roati. Exploring the ferromagnetic behaviour of a repulsive fermi gas through spin dynamics. *Nature Physics*, 13(7):704–709, 2017.

[393] N. J. van Druten and W. Ketterle. Two-step condensation of the ideal bose gas in highly anisotropic traps. *Phys. Rev. Lett.*, 79:549–552, Jul 1997.

[394] M. Vazquez and S. DE WITT. Tangle analysis of gin site-specific recombination. In *Mathematical Proceedings of the Cambridge Philosophical Society*, volume 136, pages 565–582. Cambridge University Press, 2004.

[395] S. Vezzoli, A. Mussot, N. Westerberg, A. Kudlinski, H. Dinparasti Saleh, A. Prain, F. Biancalana, E. Lantz, and D. Faccio. Optical analogue of the dynamical casimir effect in a dispersion-oscillating fibre. *Communications Physics*, 2(1):84, 2019.

[396] L. Vichi and S. Stringari. Collective oscillations of an interacting trapped fermi gas. *Phys. Rev. A*, 60:4734–4737, Dec 1999.

[397] A. Villois, G. Krstulovic, D. Proment, and H. Salman. A vortex filament tracking method for the gross–pitaevskii model of a superfluid. *Journal of Physics A: Mathematical and Theoretical*, 49(41):415502, 2016.

[398] A. Villois, D. Proment, and G. Krstulovic. Universal and nonuniversal aspects of vortex reconnections in superfluids. *Phys. Rev. Fluids*, 2:044701, Apr 2017.

[399] W. F. Vinen. The detection of single quanta of circulation in liquid helium ii. *Proceedings of the Royal Society of London. Series A. Mathematical and Physical Sciences*, 260(1301):218–236, 1961.

[400] D. Vocke, T. Roger, F. Marino, E. M. Wright, I. Carusotto, M. Clerici, and D. Faccio. Experimental characterization of nonlocal photon fluids. *Optica*, 2(5):484–490, 2015.

[401] D. Vocke, K. Wilson, F. Marino, I. Carusotto, E. M. Wright, T. Roger, B. P. Anderson, P. Öhberg, and D. Faccio. Role of geometry in the superfluid flow of nonlocal photon fluids. *Physical Review A*, 94(1):013849, 2016.

[402] G. Volovik, V. Mineev, and I. Khalatnikov. Theory of solutions of a superfluid fermi liquid in a superfluid bose liquid. *Zh. Eksp. Teor. Fiz*, 42(2):342–347, 1975.

[403] A. Wallraff, D. I. Schuster, A. Blais, L. Frunzio, R.-S. Huang, J. Majer, S. Kumar, S. M. Girvin, and R. J. Schoelkopf. Strong coupling of a single photon to a superconducting qubit using circuit quantum electrodynamics. *Nature*, 431(7005):162–167, 2004.

[404] W. Wan, S. Jia, and J. W. Fleischer. Dispersive superfluid-like shock waves in nonlinear optics. *Nature Physics*, 3(1):46–51, 2007.

[405] Y. Wang, S. Shevate, T. M. Wintermantel, M. Morgado, G. Lochead, and S. Whitlock. Preparation of hundreds of microscopic atomic ensembles in optical tweezer arrays. *npj Quantum Information*, 6(1):54, 2020.

[406] C. N. Weiler, T. W. Neely, D. R. Scherer, A. S. Bradley, M. J. Davis, and B. P. Anderson. Spontaneous vortices in the formation of bose–einstein condensates. *Nature*, 455(7215):948–951, 2008.

[407] S. Weinfurtner, E. W. Tedford, M. C. Penrice, W. G. Unruh, and G. A. Lawrence. Classical aspects of hawking radiation verified in analogue gravity experiment. *Analogue gravity phenomenology: Analogue spacetimes and horizons, from theory to experiment*, pages 167–180, 2013.

[408] D. M. Weld, H. Miyake, P. Medley, D. E. Pritchard, and W. Ketterle. Thermometry and refrigeration in a two-component mott insulator of ultracold atoms. *Phys. Rev. A*, 82:051603, Nov 2010.

[409] B. Wetzel, D. Bongiovanni, M. Kues, Y. Hu, Z. Chen, S. Trillo, J. M. Dudley, S. Wabnitz, and R. Morandotti. Experimental generation of riemann waves in optics: A route to shock wave control. *Phys. Rev. Lett.*, 117:073902, Aug 2016.

[410] G. B. Whitham. Non-linear dispersive waves. *Proceedings of the Royal Society of London. Series A. Mathematical and Physical Sciences*, 283(1393):238–261, 1965.

[411] C. M. Wilson, G. Johansson, A. Pourkabirian, M. Simoen, J. R. Johansson, T. Duty, F. Nori, and P. Delsing. Observation of the dynamical casimir effect in a superconducting circuit. *nature*, 479(7373):376–379, 2011.

[412] M. Wittemer, F. Hakelberg, P. Kiefer, J.-P. Schröder, C. Fey, R. Schützhold, U. Warring, and T. Schaetz. Phonon pair creation by inflating quantum fluctuations in an ion trap. *Physical review letters*, 123(18):180502, 2019.

[413] G. Wlazłowski, A. Bulgac, M. M. Forbes, and K. J. Roche. Life cycle of superfluid vortices and quantum turbulence in the unitary fermi gas. *Phys. Rev. A*, 91:031602, Mar 2015.

[414] K. C. Wright, R. B. Blakestad, C. J. Lobb, W. D. Phillips, and G. K. Campbell. Driving phase slips in a superfluid atom circuit with a rotating weak link. *Phys. Rev. Lett.*, 110:025302, Jan 2013.

[415] G. Xu, M. Conforti, A. Kudlinski, A. Mussot, and S. Trillo. Dispersive dam-break flow of a photon fluid. *Phys. Rev. Lett.*, 118:254101, Jun 2017.

[416] G. Xu, A. Mussot, A. Kudlinski, S. Trillo, F. Copie, and M. Conforti. Shock wave generation triggered by a weak background in optical fibers. *Optics letters*, 41(11):2656–2659, 2016.

[417] T. Yefsah, R. Desbuquois, L. Chomaz, K. J. Günter, and J. Dalibard. Exploring the thermodynamics of a two-dimensional bose gas. *Phys. Rev. Lett.*, 107:130401, Sep 2011.

[418] Z.-Q. Yu. Equation of state and phase transition in spin-orbit-coupled bose gases at finite temperature: A perturbation approach. *Physical Review A*, 90(5):053608, 2014.

[419] V. E. Zakharov, V. S. L'vov, and G. Falkovich. *Kolmogorov spectra of turbulence I: Wave turbulence*. Springer Science & Business Media, 2012.

[420] Y. B. Zel'Dovich and Y. P. Raizer. *Physics of shock waves and high-temperature hydrodynamic phenomena*. Courier Corporation, 2002.

[421] A. Zenesini, A. Berti, R. Cominotti, C. Rogora, I. G. Moss, T. P. Billam, I. Carusotto, G. Lamporesi, A. Recati, and G. Ferrari. Observation of false vacuum decay via bubble formation in ferromagnetic superfluids. *arXiv preprint arXiv:2305.05225*, 2023.

[422] C.-H. Zhang and H. A. Fertig. Collective excitations of a two-component bose-einstein condensate at finite temperature. *Physical Review A*, 75(1):013601, 2007.

[423] J.-Y. Zhang, S.-C. Ji, Z. Chen, L. Zhang, Z.-D. Du, B. Yan, G.-S. Pan, B. Zhao, Y.-J. Deng, H. Zhai, S. Chen, and J.-W. Pan. Collective dipole oscillations of a spin-orbit coupled bose-einstein condensate. *Phys. Rev. Lett.*, 109:115301, Sep 2012.

[424] Y. Zhang, X. Cheng, X. Yin, J. Bai, P. Zhao, and Z. Ren. Research of far-field diffraction intensity pattern in hot atomic rb sample. *Optics express*, 23(5):5468–5476, 2015.

[425] T. Zibold, V. Corre, C. Frapolli, A. Invernizzi, J. Dalibard, and F. Gerbier. Spin-nematic order in antiferromagnetic spinor condensates. *Phys. Rev. A*, 93:023614, Feb 2016.

[426] S. Zuccher, M. Caliari, A. W. Baggaley, and C. F. Barenghi. Quantum vortex reconnections. *Physics of fluids*, 24(12):125108, 2012.

[427] W. H. Zurek. Cosmological experiments in superfluid helium? *Nature*, 317(6037):505–508, 1985.

[428] W. H. Zurek. Cosmological experiments in condensed matter systems. *Physics Reports*, 276(4):177–221, 1996.

[429] M. W. Zwierlein, C. A. Stan, C. H. Schunck, S. M. F. Raupach, S. Gupta, Z. Hadzibabic, and W. Ketterle. Observation of bose-einstein condensation of molecules. *Phys. Rev. Lett.*, 91:250401, Dec 2003.